SYNTHESIS AND CHARACTERIZATION OF ROTATIONALLY DISORDERED INTERGROWTHS CONTAINING PbX AND TiX_2 (X = Se AND Te)

by

DANIEL B. MOORE

A DISSERTATION

Presented to the Department of Chemistry and Biochemistry
and the Graduate School of the University of Oregon
in partial fulfillment of the requirements
for the degree of
Doctor of Philosophy

December 2014

DISSERTATION APPROVAL PAGE

Student: Daniel B. Moore

Title: Synthesis and Characterization of Rotationally Disordered Intergrowths Containing PbX and TiX_2 (X = Se and Te)

This dissertation has been accepted and approved in partial fulfillment of the requirements for the Doctor of Philosophy degree in the Department of Chemistry and Biochemistry by:

Dr. Shannon W. Boettcher	Chairperson
Dr. David C. Johnson	Advisor
Dr. Darren W. Johnson	Core Member
Dr. Ben McMorran	Institutional Representative

and

J. Andrew Berglund	Dean of the Graduate School

Original approval signatures are on file with the University of Oregon Graduate School.

Degree awarded December 2014

DISSERTATION ABSTRACT

Daniel B. Moore

Doctor of Philosophy

Department of Chemistry and Biochemistry

December 2014

Title: Synthesis and Characterization of Rotationally Disordered Intergrowths Containing PbX and TiX_2 (X = Se and Te)

The method of modulated elemental reactants (MER) is used to prepare the layered compound $Ti_{1+x}Se_2$. Using a thin-film precursor prepared by sequentially depositing elemental titanium and selenium by physical vapor deposition, the binary compound is readily formed by short-duration annealing at 350°C. The structural and electrical properties of this compound are investigated and suggest that the film is markedly different from the bulk crystalline material. The synthesis is then expanded to produce the first $TiSe_2$ turbostratically disordered misfit layer compound, $(PbSe)_{1.16}TiSe_2$. With the synthesis technique established, the second compound in this family, $(PbSe)_{1.18}(TiSe_2)_2$, was synthesized and compared to the misfit layer compound synthesized by bulk methods. The rotationally disordered compound demonstrated an increased Seebeck coefficient and reduced resistivity at room temperature, sparking interest in this family of compounds as potential thermoelectric materials.

Designed synthesis of several targeted compounds is reported with interest in evaluating thermoelectric potential of these rotationally disordered compounds. The first nine members of this family were synthesized with m and n values 1 – 3 and evaluated for

their thermoelectric properties. Results from this study indicated compounds with larger n values could be of further interest and many more of these compounds are synthesized and reported.

Designed synthesis using the MER synthesis method is then pushed further to synthesize the first telluride misfit layer compounds. Four new compounds of the $[(PbTe)_{1.17}]_m(TiTe_2)_n$ family are reported, and their structures were examined by a variety of X-ray diffraction techniques. The robustness of the MER method is revealed by the synthesis of these layered intergrowths which would not be possible using other synthesis methods available.

This work consists, in part, of previously published and coauthored material.

CURRICULUM VITAE

NAME OF AUTHOR: Daniel B. Moore

GRADUATE AND UNDERGRADUATE SCHOOLS ATTENDED:

University of Oregon, Eugene
University of Iowa, Iowa City

DEGREES AWARDED:

Doctor of Philosophy, Chemistry, 2014, University of Oregon
Master of Science, Chemistry, 2009, University of Oregon
Bachelor of Science, Chemistry, 2007, University of Iowa

PROFESSIONAL EXPERIENCE:

Graduate Technical Intern, Intel Corporation, 1 year

GRANTS, AWARDS, AND HONORS:

IGERT Fellowship, University of Oregon, 2011

PUBLICATIONS:

Merrill, D. R.; Moore, D. B.; Ditto, J.; Sutherland, D. R.; Falmbigl, M.; Winkler, M.; Hans-Fridtjof, P.; Johnson, D. C. *Eur. J. Inorg. Chem.* **2014**, (in press).

Merrill, D. R.; Moore, D. B.; Coffey, M. N.; Jansons, A. W.; Falmbigl, M.; Johnson, D. C. *Semicond. Sci. Technol.* **2014**, *29*, 064004.

Moore, D. B.; Beekman, M.; Disch, S.; Johnson, D. C. *Angew. Chem. Int. Ed. Engl.* **2014**, *53*, 5672-5675.

Atkins, R.; Moore, D. B.; Johnson, D. *Chem. Mater.* **2013**, *25*, 1744–1750.

Moore, D. B.; Beekman, M.; Disch, S.; Zschack, P.; Hausler, I.; Neumann, W.; Johnson, D. C. *Chem. Mater.* **2013**, *25*, 2404–2409.

Moore, D. B.; Stolt, M.; Atkins, R.; Sitts, L.; Jones, Z.; Disch, S.; Beekman, M.; Johnson, D. *Emerg. Mater. Res.* **2012**, *1*, 292–298.

Moore, D. B.; Sitts, L.; Stolt, M. J.; Beekman, M.; Johnson, D. C. *J. Electron. Mater.* **2012**, *42*, 1647–1651.

ACKNOWLEDGMENTS

Many people have contributed to the success of the work. I would like to thank my lab mates, past and present, for the help that they have all provided. This includes Sage Bauers, Devin Merrill, Richard Westover, Marco Esters, Suzzie Wood, Matti Alemayehu, Noel Gunning, Ryan Reynolds, Dr. Matthias Falmbigl, and Dr. Ryan Atkins. I would also like to thank my advisor, Professor David Johnson, for his patience and guidance throughout this process and for providing me with a pathway into the Ph.D. program. I would like to thank Markus Kuhn and Marc French at Intel Corporation for giving me such a great internship experience. No research would have been possible without Kris Johnson and David Senkovich, thank you for everything. Thank you to Jeff Ditto for always being there to help with a smile. I would like to thank the many undergraduates who contributed to this work. This includes Luke Sitts, Matt Stolt, Duncan Sutherland, Chrissa Turley, Chun Lee, Daniel Berg, Kat Hansen, and Jessica Foelker, and Zack Jones. I would also like to thank the rotation students who worked with me on a variety of projects, including Don Clayton, Adam Jansons, and Ann Greenaway.

I am especially grateful to three post-doctoral researchers who helped me so much along the way; Dr. Matt Beekman, Dr. Sabrina Disch, and Dr. Ngoc Nguyen, thank you for everything you taught me.

A special thanks to my parents, Ken and Connie, for their support, and to my wife Natalee for everything.

I would like to acknowledge funding from the National Science Foundation under

Grant DMR 0907049, ONR Grant No. N00014-07-1-0358, Grant DMR-1266217, Grant MRI 0923577, and CCI Grant CHE-1102637. Support from the Oregon's National Science Foundation IGERT Fellowship Program under Grant No. DGE-0549503. Use of the Advanced Photon Source was supported by the U.S. Department of Energy, Office of Science, Office of Basic Energy Sciences, under Contract No. DE-AC02-06CH11357.

To Natalee

TABLE OF CONTENTS

LIST OF FIGURES

Figure Page

Figure Page

Figure Page

Figure Page

LIST OF TABLES

CHAPTER I

INTRODUCTION

The development of new solid materials has had dramatic impacts on our modern way of life. From microprocessors to lasers to superconductors, new materials have always been hand in hand with technological breakthroughs. Solid state synthesis has offered unique challenges to chemists compared to solution based techniques. DiSalvo outlined in 1990[1] how the principles of synthetic molecular chemistry have been difficult to apply towards synthesis of new solid materials. There is very little ability to predict composition, structure, and reaction mechanism. This limited ability to control the reaction mechanism and predict the synthesis outcome has prevented the preparation of large numbers of higher order compounds, such as quaternary systems. In order to move forward in materials synthesis, researchers must gain control over these predictive powers. Stein et al. in 1993[2] point out that these limitations largely stem from the use of high temperature solid-solid reactions. High temperature is used to enhance diffusion rates in systems where the diffusion lengths are on the order of microns to form thermodynamically stable products. For a synthesis to be successful, the higher order product must be more stable than a mixture of the elements and lower order (binary, ternary) products. Stein suggests that a method for gaining predictive power is to retain elements of the precursor in the final product. A synthesis that uses precursors similar to the desired product can proceed at much lower temperatures, presenting the possibility of trapping kinetically stable products.

The modulated elemental reactant (MER) synthesis method has been developed to realize kinetic products by reducing diffusion lengths required for reaction through creating precursors that are very close to the desired compound in composition, and in an atom's location within the solid material. This method involves sequentially layering calibrated amounts of elemental material in approximately the correct composition and thickness to produce a thin film precursor. When precursor conditions are right, it will self-assemble into the desired product with low-temperature annealing rather than mixing over long distances to form thermodynamic products. Using the MER synthesis method, it has been shown that precursors can be designed to self-assemble into a targeted metastable product. To investigate the capabilities and limitations of the MER technique, layered intergrowths based on typically thermodynamically stable building blocks were examined. These layered intergrowths are known as misfit layer compounds.

Misfit layer compounds have proven to be an excellent field for examining the MER synthesis method. These unique laminates, typically represented as $[(MX)_{1+\delta}]_m(TX_2)_n$, consist of a layered intergrowth of a rock salt-like (MX) and transition metal dichalcogenide (TX_2). M is Sn, Pb, Bi, or a rare earth metal, T is a group IV, V, or VI transition metal, and X is a chalcogen. The misfit (1+δ) represents the difference in packing density of the two constituents. The number of rocksalt bilayers and TX_2 trilayers are represented by m and n respectively. These bizarre compounds have long been of interest for developing materials with unique and desirable properties.[3] The vast majority of reports of misfit layer compounds are on sulfides, although there are a

few examples of selenides[3]. These compounds are synthesized using traditional methods, and the products obtained exist in thermodynamic equilibrium. Interestingly, the two constituent structures are commonly found to distort toward one another resulting in common b (in-plane) and c (cross-plane) lattice parameters, arranging in a three dimensional crystal. In the literature, thermodynamically stable misfit layer compounds generally consist of m, $n \leq 3$.[3] While the obvious limitations of traditional synthesis techniques would be expected to result in a limited suite of the most thermodynamically stable products, there is no apparent reason why other layering schemes should not be kinetically stable, if they could be realized synthetically. In 2008 Lin et al. reported the first MER synthesized misfit layer compounds, setting the stage for the synthesis of many new misfit layer compounds.[4] Since then, it has been shown that entire families of metastable layered intergrowths can be synthesized from designed precursors over a large range of m and n.[5]

Misfit layer compounds that have been synthesized using the MER method have turbostratic disorder.[6] This disorder refers to the sheets of MX and TX_2 within the layered compounds being arbitrarily rotated about the c axis. The compounds do, however, exhibit very high order in the c (cross-plane) direction, as the nearly two-dimensional constituents lay very parallel to the substrate on which they are deposited. This disorder prevents prediction of the exact location of neighboring atoms in adjacent layers. Because these turbostratically disordered misfit layer compounds do not fit the traditional definition of a crystal, the term “ferecrystal” has been used to describe them (fere from Latin, meaning “almost”). In this body of work, “ferecrystals” and

"turbostratically disordered misfit layer compounds" are synonymous. The disorder present in ferecrystals is thought to effectively scatter phonons, and therefore cause the extremely low thermal conductivity reported for this class of compounds.[7,8]

The observed low thermal conductivity suggests ferecrystals may be a useful thermoelectric material if a material system with desirable electronic properties is identified. Thermoelectric performance is judged by a parameter known as the figure of merit, zT, shown in Equation 1, and requires the optimization of parameters that have very different structural and electronic requirements and are interrelated.

$$zT = \frac{\sigma S^2}{\kappa} T$$

A higher figure of merit indicates a better thermoelectric material. Current standard materials used in thermoelectric products, such as alloys of Bi_2Te_3 and Sb_2Te_3,[9] have a figure of merit around 1. In order for a new material to be of interest in real-world thermoelectric applications, the figure of merit needs to approach or surpass zT = 1.[10] The figure of merit can be increased by reducing the thermal conductivity (κ), and this has been one key focus for electrically conductive solids in the thermoelectrics community. However, the total thermal conductivity of a material is governed by two contributions, the electronic and the lattice thermal conductivity, respectively. Whereas the electronic portion is directly influenced by the electrical conductivity via the Wiedemann-Franz relation, the lattice contribution to the total thermal conductivity can be modified independent from all other factors contributing to zT. All turbostratically disordered misfit layer compounds measured to date have shown very low lattice contribution to the thermal conductivity due to the extensive rotational disorder,

providing an ideal nanostructure for scattering phonons and allowing the search for an effective ferecrystal system to be discussed with regard to the thermoelectric power factor (σS^2) where σ is the electrical conductivity and S is the Seebeck coefficient. Both σ and S depend on the number of free carriers in the material, unfortunately the dependencies are at odds with one another. A high carrier concentration yields high conductivity, but generally at the expense of the Seebeck coefficient, while a low carrier concentration increases the Seebeck coefficient while lowering conductivity. Optimizing these two parameters has been a major challenge in the thermoelectrics community due in part to limitations in solid state synthesis. One approach has been the synthesis of composite materials to optimize individual properties in different phases, rather than trying to optimize them together in a single phase, which has proven exceedingly difficult.[11] The use of modulated elemental reactants to synthesize designed nano- and subnanoscale composites may provide the synthetic control required to realize metastable materials with competitive zT values for low temperature applications.

Previous investigations into the electrical transport properties of turbostratically disordered misfit layer compounds have been reported. Semiconducting compounds within the $[(MSe)_{1+\delta}]_m(MoSe_2)_n$ family[4] have shown that electrical properties can vary dramatically even within a single compound made multiple times, as transport properties of compounds in this semiconducting regime are heavily dominated by defects present in the material, which in turn are strongly dependent on small changes in precursor composition. On the other hand, investigations into metallic compounds such as those based on $NbSe_2$, VSe_2, and $TaSe_2$ [5,12–14] have shown that there is relatively

little deviation of electrical characteristics within the same compound made repeatedly, and a systematic change in properties with the nanoarchitecture. While compounds in the above-mentioned systems clearly demonstrated the usefulness of the MER technique for realizing a large variety of compounds with varying amounts of either constituent, none have provided ideal constituent properties for designing compounds with tunable thermoelectric properties within a family of compounds.

TiX_2 and derivative compounds have been shown to exhibit interesting electrical properties, including charge density behavior. $TiTe_2$ is known to be semimetallic[15] and TiS_2 is semiconducting,[16] but the properties of $TiSe_2$ have resulted in some debate in the literature regarding the nature of the band structure. Nominally it would be expected to be semiconducting with Ti^{4+} and $2Se^{2-}$, assuming there is no overlap between the valence Se 4p and conduction Ti 3d bands. Initially thought to be semimetallic,[17,18] recent photoemission studies suggest that the pure material is actually a small band gap semiconductor.[19] The material has been shown to be incredibly sensitive to synthesis conditions, with higher temperatures resulting in a loss of Se atoms, which has been rationalized by the incorporation of excess Ti into the van der Waals gap between layers. The confusion regarding the band structure is no surprise considering the sensitivity to synthesis conditions reported for the compound, and the expected changes in the Fermi level with slight deviations from ideal stoichiometries.[17] TiS_2 and $TiSe_2$ have shown anomalously high Seebeck coefficients for high levels of carrier concentration (10^{20}-10^{21} cm^{-3}), attributed to a large phonon drag effect, and therefore have garnered interest in the thermoelectrics community.[20]

More recently, it has been shown that the electrical properties can be systematically affected by incorporating atoms or other structures into the van der Waals gap between the TiX_2 layers. Cu has been found to systematically affect the charge density wave and thermoelectric properties of TiS_2[21–23]. The m = n = 1 misfit layer compounds have been reported in the sulfide system with both PbS and SnS.[24] Further work on the sulfide system showed that the compounds could also be realized with n = 2, with Pb, Sn, and Bi as the rocksalt cation.[25] In all cases, the properties of the TiS_2 layer seemed to be more or less intact, with an increase in carrier concentration. Not surprisingly, the incorporation of structures and atoms in the van der Waals gap lowers the thermal conductivity in the material considerably[25], and may provide a method controlling electrical properties while minimizing thermal conduction to optimize the thermoelectric performance of the material. Such reports lead us to investigate the $[(MSe)_{1+\delta}]_m(TiSe_2)_n$ compounds in an attempt to design material properties by trapping kinetic products with varied m and n, via the MER approach.

The first step into investigating $TiSe_2$ ferecrystals was the synthesis of the binary $TiSe_2$ using the modulated elemental reactant method. This work is presented in Chapter III, Characterization of nonstoichiometric $Ti_{1+x}Se_2$ prepared by the method of modulated elemental reactants, and was published in volume 41, issue 12, of the Journal of Electronic Materials in 2012 with co-authors Luke Sitts, Matthew J. Stolt, Matt Beekman, and David C. Johnson. Luke Sitts and Matthew J. Stolt assisted in sample preparation along with both electrical and X-ray data collection, Matt Beekman assisted in analysis of the electrical data, David C. Johnson is my advisor and research group

leader, and I am the primary author. The compound produced acted electronically as a heavily doped semiconductor, which is different than what is seen in bulk $TiSe_2$ not prepared by the MER method. This behavior is thought to be due to the MER compound containing excess Ti atoms, which are incorporated into the van der Waal's gap and donate electrons to the conduction band of the material. Interestingly, the Seebeck coefficient was found to be relatively large for the carrier concentration observed.

Using the synthesis information for $TiSe_2$, the first $TiSe_2$ turbostratically disordered misfit layer compound was attempted by layering Pb and Se between the $TiSe_2$ units. After careful calibration of the deposition system, the $[(PbSe)_{1.16}]_1(TiSe_2)_1$ compound was successfully synthesized and these results are presented in Chapter IV, Structural and electrical properties of $(PbSe)_{1.16}TiSe_2$. This work was published in volume 1, issue 6, of Emerging Materials Research in 2012 with co-authors Matthew J. Stolt, Ryan Atkins, Luke Sitts, Zachary Jones, Sabrina Disch, Matt Beekman, and David C. Johnson. Matthew J. Stolt and Luke Sitts assisted in sample preparation along with both electrical and X-ray data collection, Ryan Atkins assisted in microprobe data collection, Zachary Jones and Sabrina Disch provided the Rietveld and le Bail analysis, Matt Beekman assisted in analysis of the electrical data, David C. Johnson is my advisor and research group leader, and I am the primary author. This article presents the synthesis and structural characterization of this new compound and examines basic electrical transport properties.

Chapter V, Phase Width of Kinetically Stable $([PbSe]_{1+y})_1(TiSe_2)_1$ Ferecrystals and the Effect of Precursor Structure on Electrical Properties, investigates the reproducibility in structure and electrical transport properties of this compound made several times. From this chapter we observe that variation within a compound synthesized several times can be great, but variation of samples synthesized in the same deposition cycle is much less. This indicates that in order to evaluate trends in electrical properties within a family of compounds, compounds will need to be made in the same deposition cycle. Sage Bauers assisted in this work in the sample synthesis, electrical measurements, and editing of the chapter.

In 2010, Giang et al.[26] published an article reporting the synthesis of the $(PbSe)_{1.18}(TiSe_2)_2$ misfit layer compound. In this article, the authors attempted to synthesize $(PbSe)_{1.16}TiSe_2$ by combining stoichiometric amounts of elemental precursor and using traditional high temperature synthesis techniques. This resulted instead in the formation of the more stable $(PbSe)_{1.18}(TiSe_2)_2$ compound. This article presented an opportunity to compare a ferecrystal with the misfit layer compound analogue. Using the synthesis technique developed in Chapter IV, precursors were designed to assemble into the $(PbSe)_{1.18}(TiSe_2)_2$ compound. These results are presented in Chapter VI, Synthesis, structure, and properties of turbostratically disordered $(PbSe)_{1.18}(TiSe_2)_2$. This work was published in volume 25 of Chemistry of Materials in 2013 with co-authors Matt Beekman, Sabrina Disch, Paul Zschack, Ines Hausler, Wolfgang Neumann, and David C. Johnson. Matt Beekman assisted in analysis of electrical data, Sabrina Disch provided the Rietveld and le Bail analysis, Paul Zschack assisted in X-ray diffraction

analysis at the Advanced Photon Source Ines Hausler and Wolfgang Neumann provided analysis of electron diffraction, David C. Johnson is my advisor and research group leader, and I am the primary author. When compared, the ferecrystal has electrical properties that are significantly different than the misfit layer compound, including lower resistivity at room temperature and a two times higher Seebeck coefficient.

Designed synthesis was tested in more detail in Chapter VII, Investigating the electrical properties within the $[(PbSe)_{1+\delta}]_m(TiSe_2)_n$ family of ferecrystals (m,n = 1-3). The first nine compounds of this family with m and n values 1-3 were synthesized and the electrical properties explored. This work indicates a strong correlation between increasing $TiSe_2$ layers and increasing magnitude of the Seebeck coefficient, while the resistivity remains relatively constant for all samples examined. This work also corroborates what is seen in Chapter V; that trending within a deposition cycle is evident but variation between cycles can be large. Several people contributed to work presented in this chapter. Matt Stolt made several of the samples as an undergraduate in the lab. Kat Hansen (Undergraduate), Ann Greenaway (Rotation student) and Daniel Berg (Undergraduate) were responsible for many electrical measurements.

The changes in electrical properties as n, or the number of $TiSe_2$ units, increases is further investigated in Chapter VIII, Investigating electrical properties of the $([PbSe]_{1+\delta})_1(TiSe_2)_n$ family of ferecrystals (n = 1-18). This chapter indicates that increasing n generally leads to a decrease in the number of electrons per unit volume as the ratio of donors to acceptors is decreased. Plotting the Seebeck coefficient versus carrier concentration further confirms the need to realize a consistent manner of

decreasing the number of carriers in the material to make them viable thermoelectric materials.

The MER synthesis method is more rigorously tested in Chapter IX, Telluride misfit layer compounds: $[(PbTe)_{1.17}]_m(TiTe_2)_n$. This work was published in volume 53 of Angewandte Chemie International Edition in 2014 with co-authors Matt Beekman, Sabrina Disch, and David C. Johnson. Matt Beekman provided assistance with electrical data analysis, Sabrina Disch provided the Rietveld and le Bail analysis, David C. Johnson is my advisor and research group leader, and I am the primary author. This chapter reports the synthesis of metastable telluride compounds that are the first telluride misfit layer compounds. The robustness of the MER method is revealed by the synthesis of these layered intergrowths which would not be possible using other synthesis methods available.

CHAPTER II

SYNTHETIC METHODS

II.1. Synthesis Description

Designed precursors were produced using a custom built physical vapor deposition system. A front view of this system is shown in Figure II.1. Four positions (Position A) are available for elemental sources. Electron beam guns or effusion cells can be used in any of the positions. Selenium and tellurium were deposited using effusion cells while titanium and lead were deposited using electron beam guns. Substrates are placed on a rotatable holder at position B. Quartz crystal microbalances (QCMs) are positioned between the source and the substrate holder (Position C) for each source position. A mask is in place above the elemental sources (Position D). This mask has a 2 cut outs for each source. One cutout allows for a QCM to be constantly exposed to the plume of the evaporated material. The other cutout is directed towards the substrate holder, and has a pneumatically controlled shutter positioned directly above it to control when the plume hits the substrate. The shutter prevents deposition of material onto the substrate and can be opened manually or controlled with a computer to open sequentially.

The vacuum of the deposition system is maintained between 5×10^{-7} and 5×10^{-8} torr throughout depositions. This is accomplished using a 3-stage pumping system. On initial evacuation, valve #1 is opened and the mechanical pump backing the turbo pump (Position E) is used to obtain a vacuum of ~200 mtorr. At this point, the turbo pump is energized and evacuates the system below 1×10^{-4} torr. Once vacuum has reached this

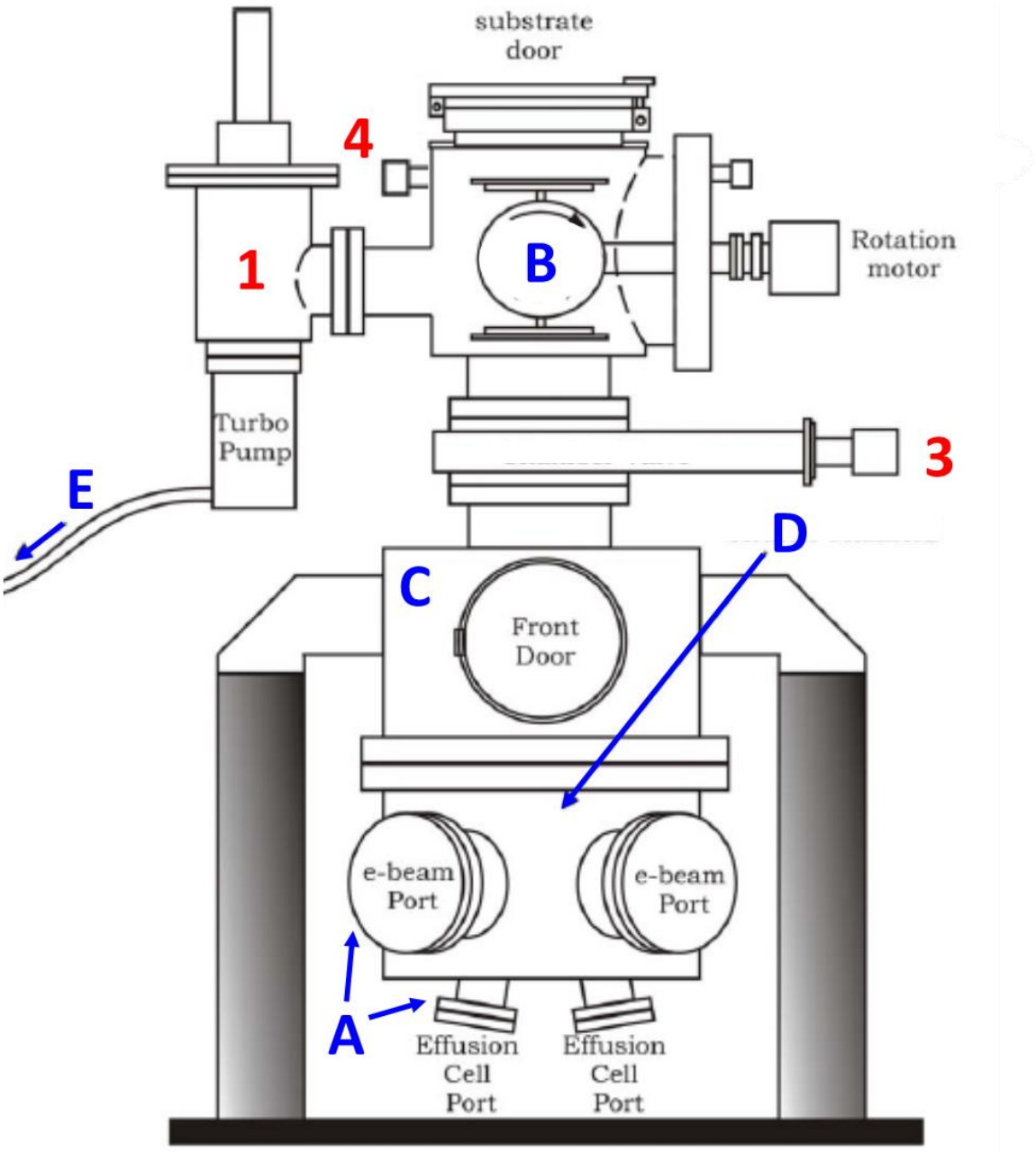

Figure II.1. Schematic representation of the deposition system used to synthesize all samples discussed. Modified from Reference 1[1].

level, valve #2 is opened and the chamber is exposed to the cryogenic pump (Not pictured, located opposite front door). Valve #1 is then closed and the cryogenic pump obtains the base vacuum of 5×10^{-7} to 5×10^{-8} torr. After deposition of precursors, sample exchange is accomplished by first closing valve #3. This isolates all the system components that are sensitive to atmospheric venting (e-beam guns, effusion cells, QCMS). Valve #4 is then opened to flow nitrogen into the top portion of the chamber. Once atmospheric pressure is reached, samples are exchanged and the system is returned to vacuum. This is done by again using the mechanical pump and turbo pump sequence. Once a suitable vacuum has been reached in the top section as to not damage lower components ($< 1 \times 10^{-5}$ torr), valve #3 is opened and the entire system is returned to cryogenic pumping.

A tedious procedure to calibrate the deposition system is first needed in order to synthesize designed precursors that meet the requirements to form the targeted compound. As a starting point, 3 samples were initially produced for each element used (Pb, Ti, and Se). A LabView controlled PC was used to deposit films of 3 different thicknesses, as reported by the QCM. The thicknesses of these films were measured using X-ray reflectivity (XRR). The measured thicknesses were then compared with the thickness measured by the QCM. It was found for all 3 elements that roughly 1/3 of the material that reaches the QCM reaches the substrate, with some slight variation that can be attributed to small changes in geometry (variation in geometry changes the ration of atoms hitting the QCM to the number of atoms hitting the substrate, commonly referred to as the tooling factor) and differences in sticking coefficients

between elements (fraction of atoms that stick at the substrate/QCM out of number that hit the substrate/QCM). Because the value displayed by the QCM is not accurate, but used frequently during the experiment, popular lab jargon to refer to this has become “Fåkestrom (Få)”. The next point in calibration, based on the above experiment, assumes 1 Få is equal to 0.3 actual Angstroms deposited onto the substrate surface. Literature values for the unit cells of the two binary compounds are then used to determine an initial starting point for deposition parameters. Initial parameters are very rough and are used only to get close enough that X-ray diffraction and electron probe microanalysis can be used to calibrate thicknesses used for designed precursors. The starting parameters for the Pb|Se sequence, for instance, were developed as follows; Literature value for the unit cell of PbSe is 6.128 Å.[1] If you assume half of this layer thickness will come from Pb atoms, and half from Se atoms, then about 3 Å of each material is desired. Since 1 Å = ~3 Få, 9 Få is a valid starting point for the deposited thicknesses of both Pb and Se for the Pb|Se layer.

The next step in a typical calibration is then to make 6 samples using the course deposition parameters obtained by the description above. Schematics of these 6 samples are shown in figure II.2. This set can be divided into 2 subsets, with one set increasing the number of Ti|Se units repeated and other set increasing the Pb|Se units. The 1:1 ratio sample is deposited twice to monitor experimental consistency. Shutters are opened sequentially to layer the precursor as shown in the schematic at the thicknesses determined from the previous step. This unit is then repeated to build a precursor film with a total thickness of around 500 Å for ease of characterization. These

6 samples are the first of many in an iterative process to obtain the correct deposition parameters that will make the precursor which self-assembles into the desired product upon low-temperature annealing. Two key factors need to be realized for the experiment to work, the layer thickness and the elemental composition. The quickest turnaround experiment to get the process moving is to measure and adjust the layer thicknesses using X-ray reflectivity (XRR) and X-ray Diffraction (XRD)

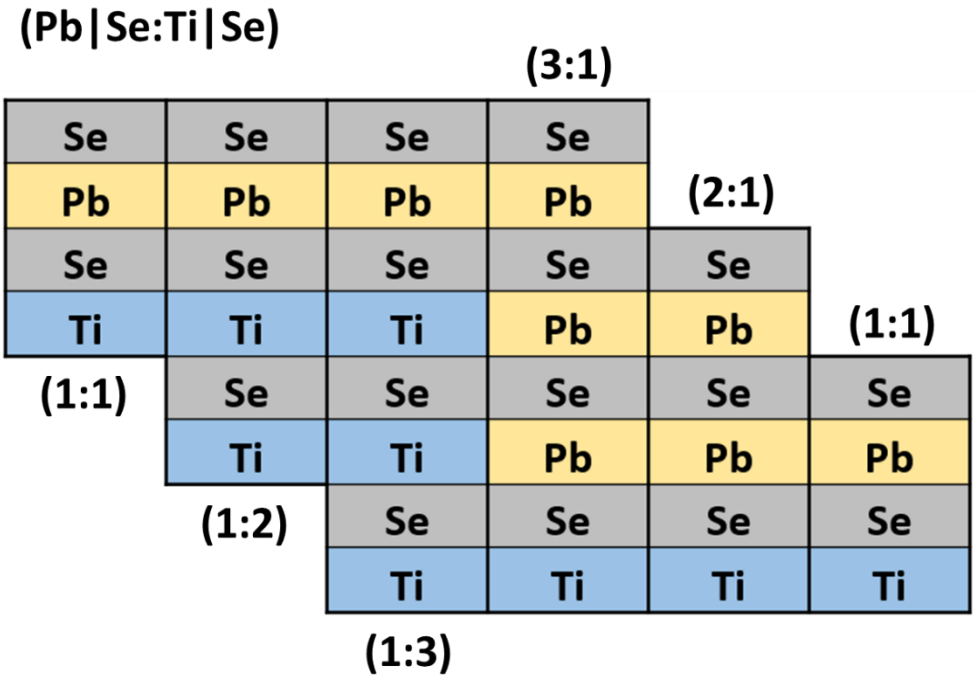

Figure II.2. Schematic representations of a typical calibration set of films.

A Bruker D8 Discover X-ray diffractometer equipped with parallel beam optics was used for the calibration process. XRR scans were taken to obtain total film thickness while XRD was used to examine the thickness of the deposited repeating unit. While the precursor is amorphous, it has abrupt enough changes in the electron density to produce diffraction maxima. The thickness determined for each sample from XRD is then used to determine the thickness of the individual deposited Pb|Se and Ti|Se layers.

An example plot of repeating unit thickness for the 6 samples deposited as a function of the number of times the Pb|Se or Ti|Se layer was deposited in a unit cell is given in Figure II.3. The slope of this line gives the thickness if the layer that was changed while the intercept corresponds to the thickness of the layer held constant in the series. The intercept is much more susceptible to error and is usually discarded while the slopes are used to determine the layer thickness. The thickness value obtained for each layer, for instance 6.21 Å for Pb|Se thickness in the example, is then compared with literature for the binary compound. The deposited values for each element, or Få, can then be scaled to give thicknesses closer to the desired literature value. The composition of the films is unknown at this point, so the Få metal|Se ratios are maintained constant as the thicknesses are scaled.

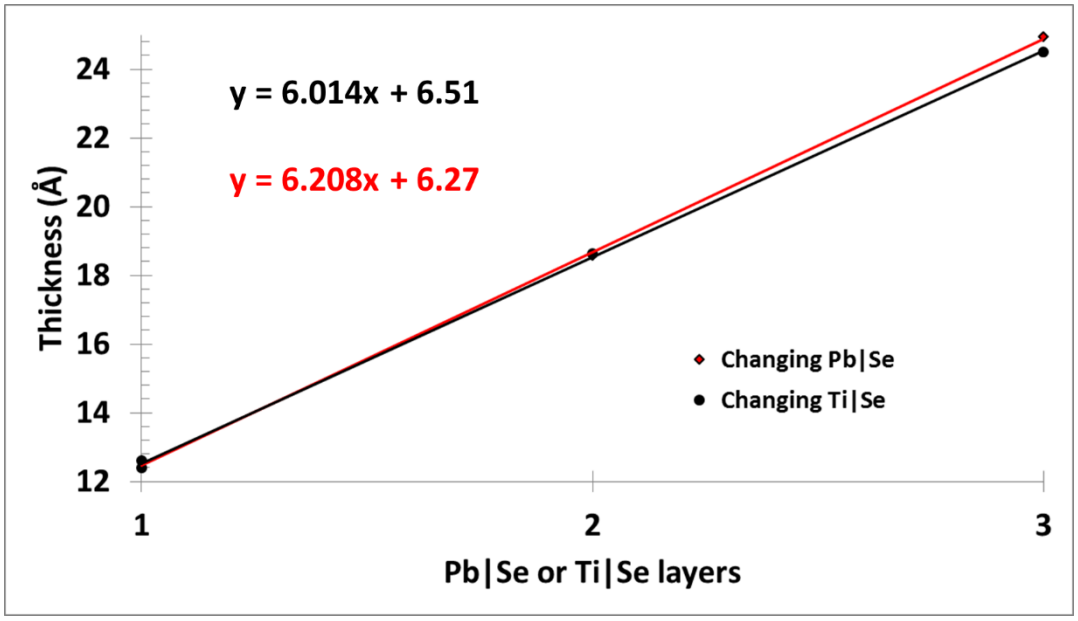

Figure II.3. Example of a thickness calibration plot from XRD thickness data.

The six samples in Figure II.2. are then deposited again, with the new values obtained from the thickness investigation. These six samples are then analyzed using electron probe microanalaysis (EPMA) (Cameca SX-50/SX-100) to determine the composition of the films, using methods described elsewhere.[2] Atomic percent of the elements is obtained and evaluated against the ideal composition. The misfit parameter is unknown at this point, but is estimated to be 1.16 from the $(PbSe)_{1.16}(TiSe_2)_2$ misfit layer compound reported.[3] The XRD patterns for the films are collected and the thickness evaluated as described in the previous step. The deposited thickness values (Få) are then adjusted to obtain a precursor closer to the desired composition and thickness. The thickness obtained from XRD is used to help determine the correct adjustments. For instance, if EPMA data shows that precursors are Ti deficient, however the thickness of the Ti|Se layer is at the targeted value, the adjustment would be an increase in the Ti Få value while decreasing the Se value to maintain the targeted thickness.

This process is iterated several times until both the composition and thickness are at the targeted values, which include a 3-5% excess of Se to account for loss during the annealing process. Because targeted values are estimated from bulk parameters and do not take into account any structural distortions that could occur in the ferecrystalline compound, annealing studies are carried out with each iteration of samples close to the targeted values. Annealing studies are explained in detail in Chapters III, IV, VIII, and IX. XRD patterns are evaluated of the annealed samples to determine if the targeted crystalline compounds form. Once deposition parameters are

determined that can reliably produce precursors that anneal into targeted precursors, any desired layering scheme can be designed to produce any $[(PbSe)_{1+\delta}]_m(TiSe_2)_n$ compound.

CHAPTER III

CHARACTERIZATION OF NONSTOICHIOMETRIC $Ti_{1+x}Se_2$ PREPARED BY METHOD OF MODULATED ELEMENTAL REACTANTS

This work was published in volume 41, issue 12, of the Journal of Electronic Materials in 2012 with co-authors Luke Sitts, Matthew J. Stolt, Matt Beekman, and David C. Johnson. Luke Sitts and Matthew J. Stolt assisted in sample preparation along with both electrical and X-ray data collection, Matt Beekman assisted in analysis of the electrical data, David C. Johnson is my advisor and research group leader, and I am the primary author.

III.1. Introduction

Layered transition metal dichalcogenides (MX_2, where M is an early transition metal and X = S, Se, or Te) are a compositionally diverse class of compounds that exhibit an equally diverse range of physical and chemical properties [1]. The structures of these materials are characterized by quasi-two dimensional X-M-X layers with covalent intra-layer bonding and weaker van der Waals bonding between layers. Metallic, semi-metallic, semiconducting, superconducting, and charge density wave electrical transport has been observed depending on the choice of transition metal. In some systems, various polytypes corresponding to distinct layer stacking order can be obtained [1], presumably due to relatively small energy differences between the different possible structures.

Recently, the modulated elemental reactants (MER) synthetic approach [2] has been used to prepare a number of layered nanostructured intergrowths derived from MX_2 constituents, with a variety of compositions and structures [3-5]. A general characteristic of layered materials prepared from MER thin film precursors is significant rotational or turbostratic disorder between the constituent layers, which, in spite of well-defined intra-layer order and precise stacking of the layers, substantially reduces long range order in these materials [3-5].

To date, the only binary transition metal dichalcogenide prepared by the MER approach that has been extensively studied is WSe_2 [6, 7]. Exceptionally low cross-plane thermal conductivity (~ 0.05 $Wm^{-1}K^{-1}$) was discovered in WSe_2 prepared from MER, attributed to the substantial turbostratic disorder between precisely layered WSe_2 sheets that is achieved by the MER synthetic approach [6, 7]. Here we report on the characterization of the binary diselenide $Ti_{1+x}Se_2$ prepared by the MER approach. $TiSe_2$ has been the subject of significant interest due to persistent questions regarding the nature of its electronic structure [8, 9] and charge density wave behavior [10], and has also been considered for potential thermoelectric applications [11,12]. To the best of our knowledge, the only prior polytype known to exist for this compound is 1-T $TiSe_2$, which adopts the CdI_2 crystal structure (Figure III.1) consisting of one $TiSe_2$ layer per unit cell [13]. In the perfect $TiSe_2$ structure, each Ti is octahedrally coordinated by six Se atoms. We find the electrical transport properties of the MER-prepared phase reported on here to be significantly different from the bulk form of this material.

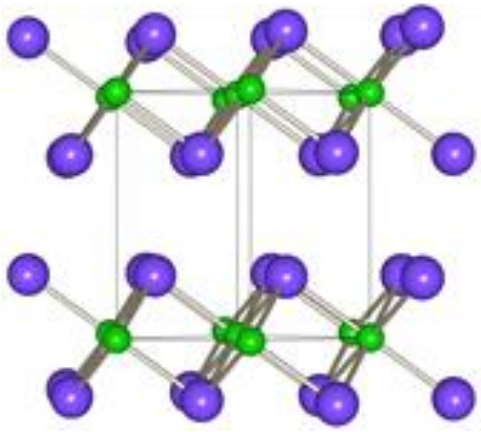

Figure III.1. Crystal structure of 1-T $TiSe_2$, with the unit cell outlined.

III.2. Experimental Details

Precursor films were synthesized using a custom-built vacuum deposition system. Titanium was deposited using an electron beam gun and an effusion cell was used to deposit selenium. The background pressure in the chamber was maintained between 5×10^{-8} and 5×10^{-7} torr during deposition. Quartz crystal microbalances monitored deposition rates which were between 0.2 and 0.3 Å/sec at the substrate; substrate exposure was controlled by pneumatic shutters. <100> Si wafers or masked fused silica slides were placed above the elemental sources and rotated about the substrate normal to increase uniformity of deposited material. 84 deposition cycles were used to deposit a film with total thickness of approximately 500 Å, as determined from X-ray reflectivity. One cycle comprises sequential opening of the Ti shutter and then the Se shutter for calibrated amounts of time to deposit sufficient material to form one $Ti_{1+x}Se_2$ layer. Calibration was accomplished using X-ray reflectivity for total film thickness and electron probe microanalysis for composition. The precursor films were

annealed on a custom-built hot plate under nitrogen atmosphere with O_2 and H_2O contents at less than 0.5 ppm levels.

X-ray reflectivity (XRR) and X-ray diffraction (XRD) data were collected using a Bruker D8 Discover (Cu Kα radiation) equipped with parallel beam optics. Film thickness was determined from analysis of the XRR data. Chemical composition was determined by electron probe microanalysis (EPMA) using a Cameca^{TM} SX-50 electron microprobe and specialized procedures developed for thin film analysis. In-plane (perpendicular to the *c*-axis) electrical resistivity (ρ) and Hall coefficient (R_H) were measured from 20 K to 300 K by the van der Pauw method on films patterned in a cross geometry in a custom closed-cycle He cryostat. In-plane Seebeck coefficient (*S*) was determined at room temperature using a dynamic differential method. Patterned films for these in-plane electrical transport measurements were deposited on insulating fused silica substrates to minimize the influence of the substrate on the measurement.

III.3. Results and Discussion

Several binary phases have been reported to exist in the Ti-Se system, and the CdI_2-type phase ($Ti_{1+x}Se_2$) has been observed to exhibit a relatively wide phase width [14, 15]. In the present study, the substrate exposure times for each element were iteratively adjusted in order to obtain precursor films with the Ti:Se composition of 1:2, and a composition modulation on the thickness length scale of one Se-Ti-Se layer (Figure III.1), i.e. approximately 6 Å [13]. An X-ray diffraction pattern of an as-deposited precursor is shown in Figure III.2.a. Very weak diffraction peaks corresponding to the

target product phase were already visible in the pattern collected from the precursor, indicating that some ordering and nucleation of the $Ti_{1+x}Se_2$ phase occurs under ambient conditions during film deposition. Since the optimum annealing conditions required to produce a well-formed product are not known *a priori*, the effects of annealing temperature and time on product formation were studied by X-ray diffraction. As an example, Figure III.2.a illustrates the evolution of the precursor as it is annealed for 30 min at successively increasing temperatures. Little change is observed at temperatures below 300°C, above which the diffraction peaks become significantly more intense. As shown in Figure III.2.b, the film thickness first decreases with increasing annealing temperature, attributed to the reduction in volume as the mostly amorphous precursor self-assembles into the $TiSe_2$ phase. The full width at half maximum of the (004) reflection (Figure III.2.c) also decreases with increasing annealing temperature, attributed to increased *c*-axis ordering as the film self-assembles into the $TiSe_2$ product. The film thickness plateaus in the 300 to 350°C temperature range, but then dramatically decreases from 400°C on, indicating degradation of the film. This is consistent with the XRD pattern for the film annealed at 500°C (Figure III.2.a), which again shows only weak peaks corresponding to the $Ti_{1+x}Se_2$ phase.

Figure III.3 shows an X-ray diffraction pattern collected in the specular geometry from a $Ti_{1+x}Se_2$ film annealed at 350°C for 30 min, along with a calculated pattern based on the bulk crystal structure [13]. The pattern contains only four well-defined peaks that can be indexed as (00*l*) reflections to a single *c*-axis parameter determined to be 6.036(2) Å from least-squares refinement. This value is somewhat larger than the *c*

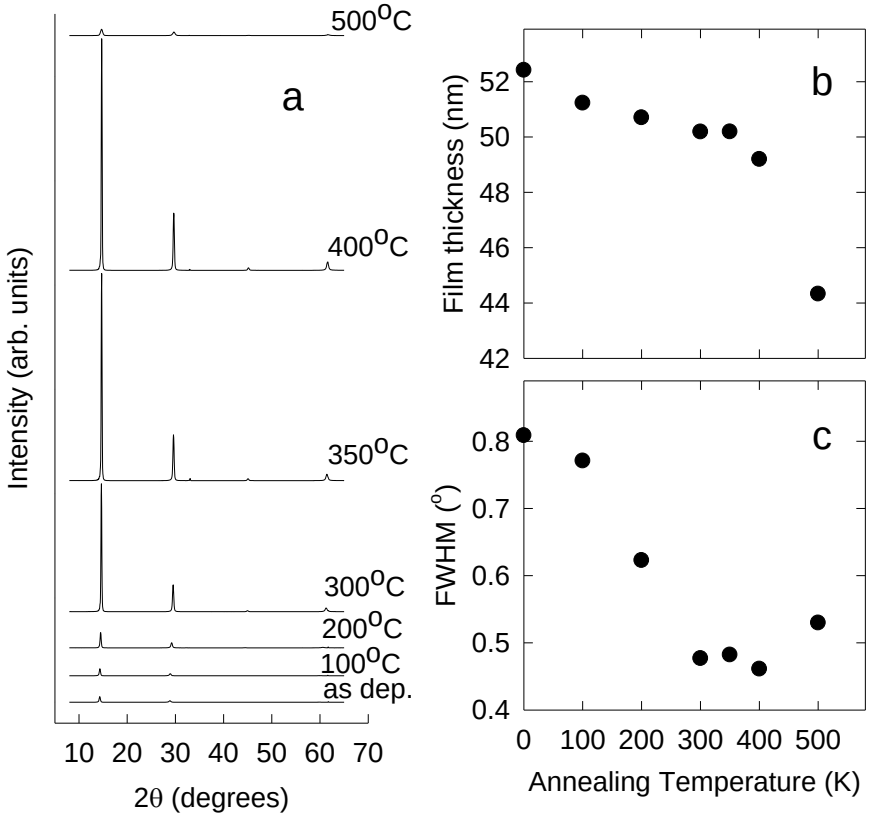

Figure III.2. (a) Selected specular X-ray diffraction patterns collected from the same precursor annealed at increasing temperatures, illustrating the evolution of the precursor to product during annealing. (b) Film thickness as a function of annealing temperature, indicating a significant decrease in thickness as the film is annealed at temperatures higher than 350°C. (c) Full width at half maximum (FWHM) of the (004) reflection as a function of annealing temperature.

parameter for stoichiometric $TiSe_2$, c = 6.008(3) Å [13]. The composition of the annealed film determined from EPMA (Table III.1) is $Ti_{1.1}Se_2$, indicating an excess of Ti. This excess is consistent with the observed increased lattice parameter relative to $TiSe_2$, assuming the additional Ti resides between the $TiSe_2$ layers, i.e. within octahedral voids in the $TiSe_2$ van der Waals gap (Figure III.1.a). The observation of only (00*l*) reflections indicates the $Ti_{1+x}Se_2$ layers are highly oriented parallel to substrate, a conclusion that is

also corroborated by rocking curve scans collected from the film (not shown). Similar observations have been observed in other layered materials prepared by MER [3-7].

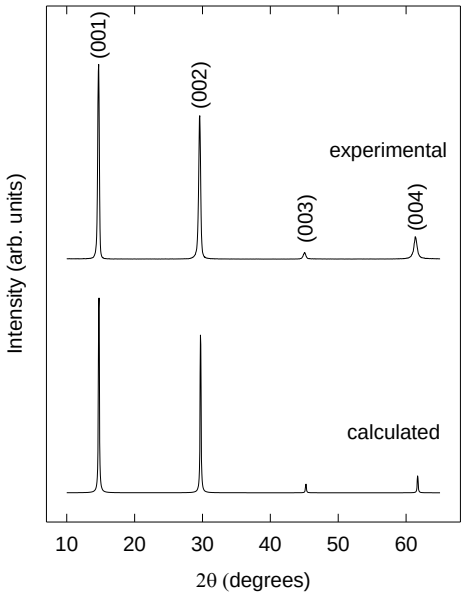

Figure III.3. Experimental (top) and simulated (bottom) X-ray diffraction patterns for $Ti_{1.1}Se_2$ prepared by MER and $TiSe_2$ [12], respectively. Only (00*l*) reflections are observed.

Table III.1. Room temperature in-plane electrical transport properties for $Ti_{1+x}Se_2$ (x = 0.1), as well as *c*-axis parameter and Ti:Se ratios for the precursor and annealed film determined from electron microprobe analysis.

Ti:Se (precursor)	Ti:Se (annealed)	*c*(Å)	ρ(mΩ-cm)	*S*(μV/K)	n(cm^{-3})	μ_H ($cm^2V^{-1}s^{-1}$)
1.0:2.0	1.1:2.0	6.036(2)	3.58	-134	3.7×10^{21}	0.47

The physical properties of 1-T $TiSe_2$ have been a topic of perpetual interest, in large part due to the challenge of unequivocally determining the nature of its electronic structure [8, 9]. The basic question of whether stoichiometric $TiSe_2$ is semiconducting or semi-metallic has motivated numerous investigations over the years, and recent studies continue to disagree on whether the conduction band maximum and valence band

minimum overlap [16] or a small energy gap exists [9]. In-plane electrical transport properties measured at room temperature on a $Ti_{1+x}Se_2$ film annealed at 350°C for 30 minutes are reported in Table III.1. Since the layers of the film are oriented parallel to the substrate, these data are indicative of the transport properties in the direction perpendicular to the *c*-axis. The moderately large, negative Seebeck coefficient observed for the specimen is uncharacteristic of a semi-metal and is in contrast to the relatively small, positive *S* observed for single crystals of $TiSe_2$ [9]. The sign of *S* suggests electrons are the majority carriers in the film. This is consistent with the composition of the film determined by EPMA, reported in Table III.1. The Ti:Se ratio indicates the annealed film is Ti-rich, with $x = 0.1$ in $Ti_{1+x}Se_2$. Assuming the excess Ti is incorporated into the structure *via* the van der Waals gap (Figure III.1) and contributes a total of four electrons per excess Ti to the intralayer Ti 3*d* conduction band (and assuming there is no valence-conduction band overlap), a carrier concentration near 7×10^{21} cm^{-3} would be expected. From the Hall coefficient measured at room temperature and the single-band relation $R_H = 1/ne$, we estimate $n = 3.7 \times 10^{21}$ cm^{-3} for the film at room temperature, in qualitative agreement with the value calculated based on the above simple crystal chemistry considerations.

From the measured electrical resistivity and Hall coefficient, the Hall mobility $\mu_H = R_H/\rho$ is calculated to be 0.47 $cm^2V^{-1}s^{-1}$. This is a relatively low value, which we attribute to small in-plane domain sizes [3-7] and relatively high concentration of defects [17] that may be present in the sample; controlled post-annealing under a controlled vapor

of the constituents may improve the carrier mobility [17] and will be the objective of future studies.

The electrical resistivity $\rho(T)$ for the MER $Ti_{1+x}Se_2$ film annealed at 350°C for 30 minutes is shown in Figure III.4.a. In contrast to the behavior observed for bulk crystalline $TiSe_2$ [10], $\rho(T)$ in Figure III.4.a has a relatively weak temperature dependence and decreases monotonically with increasing temperature. Stoichiometric single-crystals of $TiSe_2$ show a pronounced peak in $\rho(T)$ near 165 K which is attributed to the transition to a charge density wave state below 200 K [10]. Only a subtle feature resembling such a peak is observed in the data of Figure III.4.a, and the specimen does not display metallic behavior at the lowest temperatures, a feature that is also different from bulk crystalline $TiSe_2$. The temperature dependence of the Hall coefficient (Figure III.4.b) suggests the weak monotonic decrease in resistivity with increasing temperature originates from an increase in carrier concentration with temperature. The corresponding Hall mobility decreases with increasing temperature, as expected from an increase in carrier scattering by phonons as the temperature is increased.

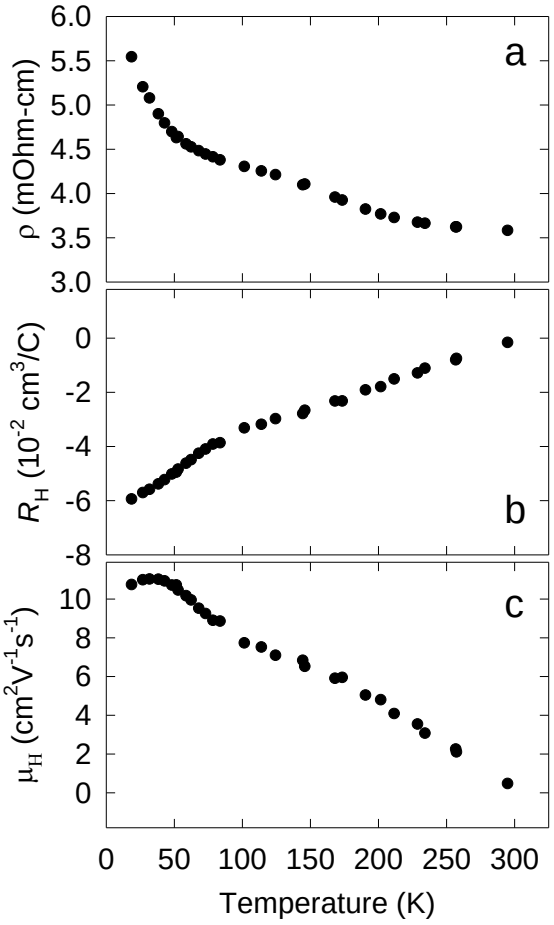

Figure III.4. (a) Electrical resistivity, (b) Hall coefficient, and (c) Hall mobility as a function for temperature for a $Ti_{1.1}Se_2$ film prepared by MER.

The electrical transport properties of MER prepared $Ti_{1+x}Se_2$ are observed to be significantly different from the bulk form of the stoichiometric compound. The observed behavior is more characteristic of a heavily doped semiconductor than a semimetal. The effect of turbostratic disorder on the electrical transport in such materials is not yet understood and may play a role in the observed difference in properties. The thermoelectric power factor S^2/ρ for the $Ti_{1.1}Se_2$ film is calculated to be 5.5 μW cm^{-1} K^{-1}. However, the relatively high carrier concentration (~ 10^{21} cm^{-3}) suggests that this may

not be the optimum composition for optimum thermoelectric performance. The effect of composition, i.e. Ti excess, on the thermoelectric properties of these materials is a topic of interest for future study.

III.4. Conclusion

We have prepared the layered dichalcogenide $Ti_{1+x}Se_2$ by the method of modulated elemental reactants. Thin film precursors with Ti:Se composition of 1:2, corresponding to the stoichiometric composition $TiSe_2$, produce a Ti-rich phase with composition $Ti_{1.1}Se_2$, presumably due to Se loss by evaporation during annealing. Electrical transport properties for the MER-prepared phase are inconsistent with semi-metallic behavior, but do agree with the notion that excess Ti contributes to heavily doped semiconductor behavior. The magnitude of the Seebeck coefficient is relatively large for the observed carrier concentration. The observations are somewhat unexpected since the bulk crystalline compound appears to show transport characteristics of a semi-metallic or very small gap semiconductor.

III.5. Bridge

The synthesis information for $TiSe_2$ can now be directly applied to design the first $TiSe_2$ turbostratically disordered misfit layer compound by attempting to layer Pb and Se between the $TiSe_2$ units. The information about the electrical transport properties of the MER synthesized $TiSe_2$ is a useful tool to compare the electrical properties of the $([PbSe]_{1+\delta})_1(TiSe_2)_n$ family of compounds and can be considered the $n = \infty$ member of this family.

CHAPTER IV

STRUCTURAL AND ELECTRICAL PROPERTIES OF $(PbSe)_{1.16}TiSe_2$

This work was published in volume 1, issue 6, of Emerging Materials Research in 2012 with co-authors Matthew J. Stolt, Ryan Atkins, Luke Sitts, Zachary Jones, Sabrina Disch, Matt Beekman, and David C. Johnson. Matthew J. Stolt and Luke Sitts assisted in sample preparation along with both electrical and X-ray data collection, Ryan Atkins assisted in microprobe data collection, Zachary Jones and Sabrina Disch provided the Rietveld and le Bail analysis, Matt Beekman assisted in analysis of the electrical data, David C. Johnson is my advisor and research group leader, and I am the primary author.

IV.1. Introduction

The search for novel materials for thermoelectric energy conversion has intensified in recent years, resulting in a number of discoveries of promising bulk and nanostructured material systems.[1] Binary and ternary chalcogenide compounds remain some of the highest performing materials in the low- to high- temperature range.[1] In recent times, a class of chalcogenide materials collectively referred to as misfit-layered compounds has received attention as potential thermoelectric materials.[2] The structures of these materials are formed by the regular stacking of two structural components derived from binary compounds, MX and TX2, resulting in the chemical formula $(MX)_{1+\delta}(TX_2)_n$, where M = Pb, Sn, Bi, Sb or a rare earth element, T = an early transition metal, X = S or Se and n represents the number of TX_2 layers in the structure, with $n < 3.3$ The term “misfit” refers to the difference in area per metal cation in the a–b plane of the constituents. Thermoelectric figure of merit ZT as high as 0.4 has already

been reported at elevated temperature,[2] even though only a small percentage of the known or conceivable[3] misfit-layered compositions have been evaluated.

Recognizing that there are no formal charge balance requirements between the formally uncharged constituents and that a stable interface exists between them, the existence of kinetically stable $(MX)_{1+\delta}(TX_2)_n$ compositions was postulated and subsequently demonstrated[4 5] in thin-film form using the modulated elemental reactants (MER) approach.[6] Similar to their crystalline misfit-layered counterparts, these materials consist of precisely stacked MX and TX_2 layers.[4 5] Unlike their crystalline misfit-layered counterparts, these materials possess a rotational disorder between the layers that strongly reduces long-range order, resulting in unusual properties that include exceptionally low thermal conductivities near 0.1 W/m-K in the cross-plane direction and 0.4 W/m-K in the in-plane direction.[4 5 7]

In this article, the authors report the synthesis and characterization of a new layered selenide, $(PbSe)_{1.16}TiSe_2$, formed as an intergrowth of PbSe and $TiSe_2$ layers, two binary compounds that have been previously acknowledged for their thermoelectric properties. Prior attempts to prepare this compound via traditional high-temperature synthesis resulted in the formation of a mixture of $(PbSe)_{1.16}(TiSe_2)_2$ and PbSe.[8] Annealing the compound past 350°C results in decomposition, suggesting that $(PbSe)_{1.16}TiSe_2$ is metastable. Diffraction and electrical transport properties measurements for the specimens studied indicate that the compound exists in a relatively small composition range, behaves similarly to a heavily doped semiconductor

or poor metal and exhibits a higher thermoelectric power factor than other MER $(MX)_{1+\delta}(TX_2)_n$ compositions prepared to date.

IV.2. Experimental Details

Thin-film samples were synthesized using a custom-built physical vapor deposition system.[6] The elements Pb and Ti were deposited using electron beam guns, and Se was deposited using an effusion cell. The background pressure in the deposition system was maintained between 5×10^{-8} and 5×10^{-7} torr during deposition of all samples to minimize oxidation during deposition. Quartz crystal microbalances were used to monitor deposition rates, which were held between 0.02 and 0.03 nm/s at the substrate. Silicon <100> substrates or masked fused silica substrates were placed above the elemental sources and rotated about the substrate normal to improve the uniformity of deposited material. Computer-controlled pneumatic shutters were opened sequentially for calibrated amounts of time to deposit the desired thicknesses of each element. In this way, thin-film samples were constructed of 42 repeating layers of Ti, Se, Pb and Se for a target fi lm thickness of 50 nm. Compositional calibration was performed using electron-probe microanalysis (Cameca SX-50, Gennevilliers, France). The ratio of the product of the time that shutters remain open during deposition and the deposition rates determine the mole ratio of the elements in the film and is iteratively adjusted to achieve the targeted composition. The shutter times were then scaled to obtain the required thickness of the modulation in the precursor. Thickness calibration was accomplished by using x-ray diffraction (XRD) and X-ray reflectivity to determine thicknesses of as-deposited precursors (Bruker D8 Discover laboratory

diffractometer with Cu Kα radiation, setup with parallel beam optics). As-deposited precursors were then annealed on a hotplate in a glovebox with a nitrogen atmosphere (O_2 and H_2O content less than 0.5 ppm during annealing).

High-resolution XRD was measured at the 33-BM-C beamline of the advanced photon source (APS) using x-ray energies of 12.503 and 13.199 keV and a point detector, with orientation of the scattering vector Q either perpendicular (00*l* reflection series) or parallel (*hk*0 reflection series) to the substrate. Refinements according to the Le Bail[9], and Rietveld[10] approaches have been carried out using the GSAS program package.[11 12]

In-plane (parallel to the substrate) electrical resistivity (ρ) was measured from 20 to 300 K by the van der Pauw method on films patterned in a cross-geometry on insulating fused silica substrates in a custom closed-cycle He cryostat electrical measurement system. Temperature-dependent resistivity was collected while cooling to 20 K and then again while heating to 300 K, showing the measurement was reproducible. The Hall coefficient (RH) was measured on the same specimens by linear fits to the Hall voltage measured as a function of magnetic field, using a maximum magnetic field of 1.8 T. The in-plane Seebeck coefficient (S) was determined at room temperature using a dynamic differential method. Patterned films for these in-plane electrical transport measurements were deposited on insulating fused silica substrates to minimize the influence of the substrate on the measurement.

IV.3. Results and Discussion

The MERs synthesis approach entails depositing a repeating sequence of elemental layers, controlling the relative composition of the precursor by the relative

thickness of the elemental layers.[6] The authors used the misfit parameter determined previously for $(PbSe)1.16(TiSe_2)_2$ as the initial value for our attempts at preparing $(PbSe)_{1+\delta}TiSe_2$. On the basis of the prior synthesis of similar compounds, the thickness of the repeating unit of the precursor was initially targeted to be close to that of the expected c-axis unit-cell size (1.2–1.3 nm), and the relative thicknesses were adjusted to obtain precursors with composition close to that expected for the target compound.[8] Table IV.1 summarizes the samples prepared as part of this study. Electron microprobe data of sample "a" yielded percentage compositions Pb:Ti:Se of 21:18:61, which is

Table IV.1. Sample designation, deposition parameters,[†] modulation period (*c*) of precursors, and the *c*-axis lattice parameters (*c*) of annealed samples for 7 of the $(PbSe)_{1.16}TiSe_2$ samples prepared in this study.

Sample	*Relative Pb Thickness*	*Relative Se Thickness*	*Relative Ti Thickness*	*Relative Se Thickness*	Precursor *c (nm)*	Annealed *c (nm)*
a	0.77(1)	1.16(1)	0.54(1)	1.76(1)	1.237(1)	1.2183(5)
b	0.77(1)	1.20(1)	0.54(1)	1.74(1)	1.230(1)	1.2183(3)
c	0.77(1)	1.20(1)	0.59(1)	1.75(1)	1.225(1)	1.218(1)
d	0.77(1)	1.20(1)	0.56(1)	1.72(1)	1.207(1)	1.217(1)
e	0.77(1)	1.20(1)	0.56(1)	1.72(1)	1.208(1)	1.217(2)
f	0.77(1)	1.20(1)	0.56(1)	1.72(1)	1.240(1)	1.2174(3)
g	0.77(1)	1.20(1)	0.56(1)	1.72(1)	1.261(1)	1.2175(3)

[†] Reported relative thicknesses do not represent actual physical thicknesses, but are instead proportional to the actual amount of deposited material. Therefore, percent differences in deposition parameters for a particular element reflect actual percent differences in the amount of deposited material.

within experimental error of the targeted percent compositions of 22:19:59 calculated using the assumed misfit parameter.

Figure IV.1 contains diffraction patterns collected as a function of annealing temperature for precursor “a.” The as-deposited precursor has a relatively strong 00*l* Bragg diffraction peak and weak higher-order 00*l* Bragg maxima reflecting the initial elemental layering with diffuse interfaces. Annealing at 300°C results in significant growth of the expected higher-order diffraction maxima, as the atoms begin to self-assemble into the targeted structure and the interfaces between layers become more abrupt. The higher-order diffraction peaks have their highest intensities after annealing at 350°C, decreasing with increased annealing temperature. Annealing at temperatures above 400°C resulted in the disappearance of diffraction maxima associated with the modulated structure, reflecting the prior literature report that the m, n = 1 structure does not form on annealing the stoichiometric composition at high temperatures.[8] On the basis of these observations, the annealing conditions of 350°C for 30 min were used to prepare samples for the experiments described below.

Precursors were prepared over a range of initial compositions and modulation repeat thicknesses in order to sample the range of compositions in which the target compound forms. Table IV.1 contains a summary of deposition parameters, initial thicknesses for the repeating elemental sequence, and the c-lattice parameter of the $(PbSe)_{1+\delta}TiSe_2$ compound that self assembles during annealing. Within the range of precursors explored, the c-lattice parameters of the products clustered around the value of 1.2176(5) nm, ranging from 1.2170 to 1.2183 nm. This suggests that the metastable

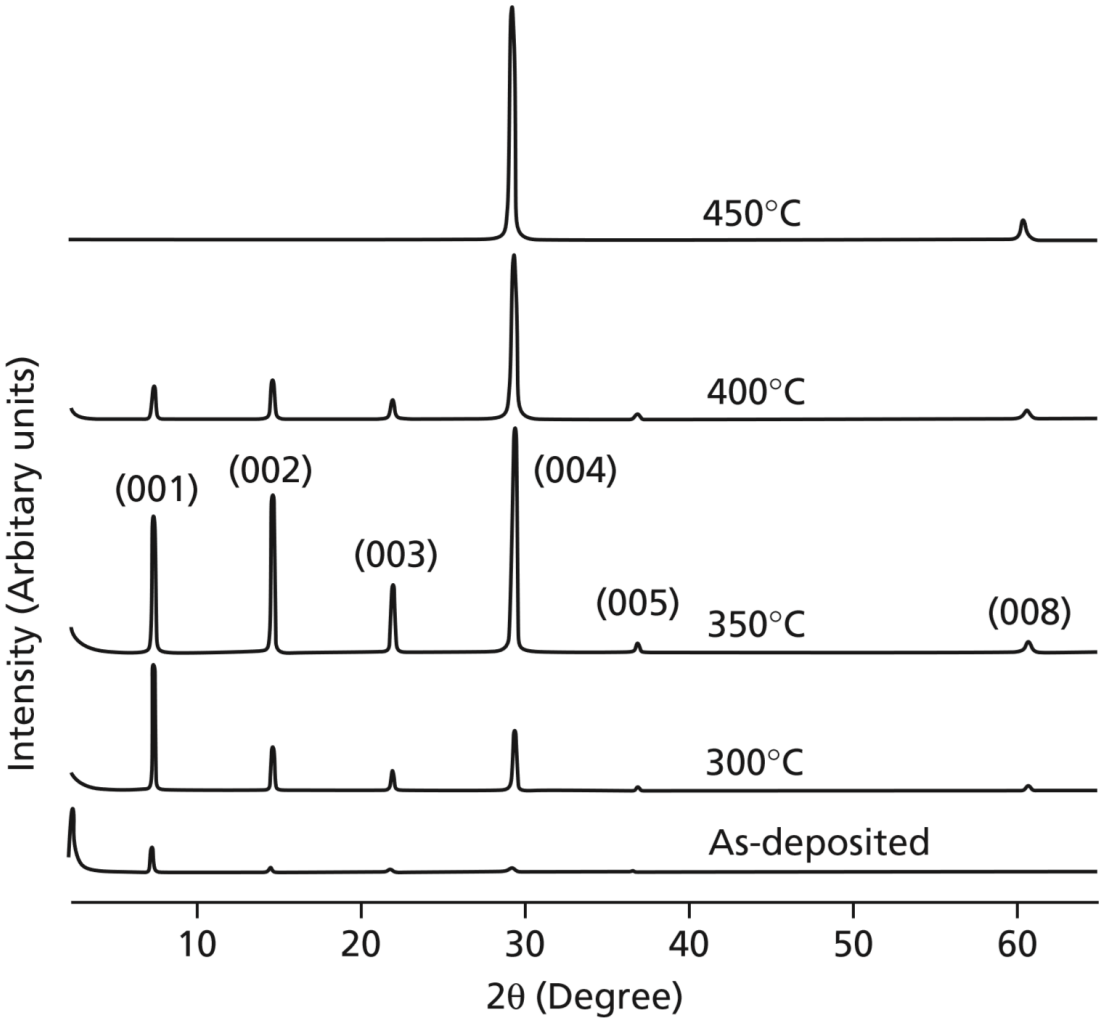

Figure IV.1. The evolution of the diffraction pattern collected using Cu Kα X-ray radiation as a function of annealing temperature. The sample was annealed for 30 minutes at the temperatures indicated above each scan before the diffraction pattern was collected. The 00*l* indices are given for each of the Bragg diffraction maxima.

$(PbSe)_{1+\delta}TiSe_2$ forms with a relatively small composition width. The consistency of the relative intensities of the Bragg diffraction maxima suggests that a specific orientation of the constituents form on annealing.

To gain knowledge of the structure of $(PbSe)_{1+\delta}TiSe_2$, several diffraction experiments were performed, including high resolution X-ray diffraction conducted at the Advanced Photon Source, Argonne National Lab. The in-plane lattice parameters of the binary

constituents were determined from the le Bail refinement of *hk*0 diffraction patterns (Figure IV.2). The observed tetragonal in-plane lattice constant of PbSe, 0.6133(3) nm and the hexagonal in-plane lattice constant of $TiSe_2$, 0.3552(7) nm agree well with bulk values of 0.6121 nm and 0.3553 nm, for PbSe[14] and $TiSe_2$,[15] respectively, suggesting minimal in-plane structural distortion occurs in the intergrowth. The refined in-plane lattice parameters result in a calculated "misfit parameter" of $\delta = 0.161(3)$, in agreement with 0.16 reported for $(PbSe)_{1.16}(TiSe_2)_2$. This misfit value is in the middle range of previously reported misfit parameters, which range between -0.01 and 0.29.[3-6] Using the Scherrer equation, the widths of the in-plane diffraction peaks were used to estimate an in-plane grain size of approximately 10 nm.

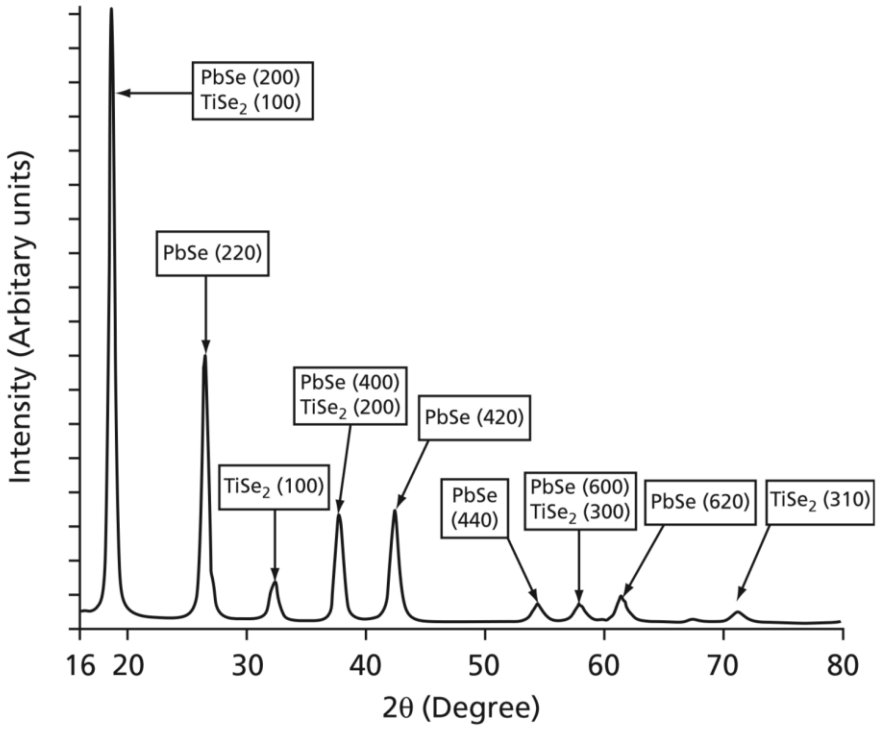

Figure IV.2. In-plane diffraction data collected at the APS using 12.503 keV radiation. The *hk*0 indices for both the $TiSe_2$ and PbSe constituents are indicated.

Le Bail refinement of 00/ reflections (diffraction data in the specular condition) yielded a unit cell parameter along the c-axis of 1.2174(2) nm, which is consistent with the expected size of a repeating unit containing one PbSe layer and one $TiSe_2$ layer. Rietveld refinement analysis (depicted in Figure IV.3) was utilized to extract the atomic plane positions (i.e. the projection of the electron density along the *c*-axis) from the intensities of the 00/ reflections. Results from Rietveld refinement are reported in Table IV.2. The refinement reveals a puckering of Pb, within the PbSe bilayer, with the Pb plane displaced towards the neighboring $TiSe_2$ Se plane of atoms as a result of the modulation between the two interwoven structures. The displacement of Pb towards the Se plane, 0.015(3) nm is slightly less than previously observed misfit layer puckering values, which range from 0.020 nm to 0.060 nm in the relatively few atomic level structures that have been previously determined.[16-23] The average Pb to Se distance of 0.302(2) nm within the rock-salt structure is close to the 0.306 nm observed in PbSe.[14] A value of 0.313(2) nm was obtained for the distance between the closest atomic planes of the two binary constituents. This M-X inter-planar distance between the rock-salt and dichalcogenide structural units is consistent with prior studies of crystal structures of lead- and tin-containing sulfide misfit layer compounds, as summarized by Wiegers.[3] The 0.145(3) nm distance between the Ti plane and the adjacent Se planes within the $TiSe_2$ constituent is shorter than the 0.153 nm inter-planar distance found in bulk $TiSe_2$.[15]

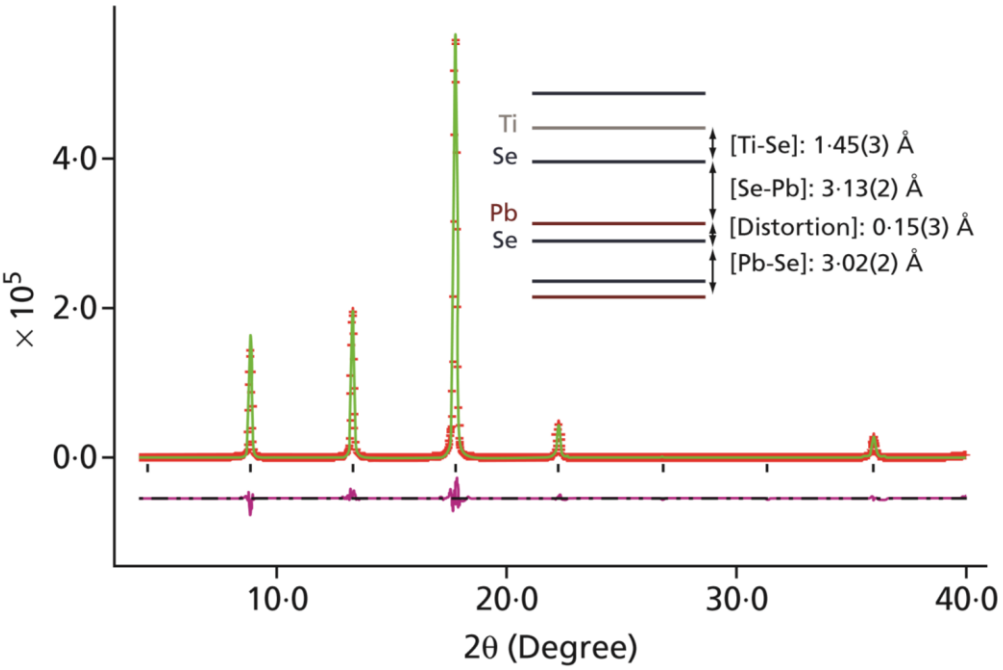

Figure IV.3. The observed, modeled, and difference curves from a Rietveld refinement using specular XRD data (13.199 keV) are shown in red, green and purple, respectively. Inset: Line diagram of the interatomic distances of the refined planes along the c-axis resulting from the 00*l* Rietveld refinement of $(PbSe)_{1.16}TiSe_2$ where Ti, Se and Pb are grey, blue and red, respectively.

Diffraction data were also collected throughout reciprocal space to examine the structure in crystallographic directions other than those accessed using the specular (00*l*) and in-plane (*hk*0) geometries. Diffraction scans along mixed index directions *hkl* (*h*, $k \neq 0$; $l \neq 0$) are very broad, yielding coherence lengths less than 2 repeating structural units. No superlattice reflections are observed in any direction other than 00*l*, i.e. the individual constituents diffract independently. In addition, the intensity is independent of rotation of the sample about the surface normal, characteristic of a two-dimensional polycrystalline material. These observations are consistent with the presence of rotational disorder between the PbSe and $TiSe_2$ constituents. In clay minerals this type of disorder is referred to as turbostratic disorder, i.e., each layer has

Table IV.2. Results from Rietveld and le Bail refinements of the $(PbSe)_{1.16}TiSe_2$ composition based on synchrotron X-ray diffraction data, including lattice parameters (intergrowth *c*, constituent *a*) *z* positions for each atom (*z*), site occupancies (occ.), important inter-planer distances (*d*), and refinement residuals.

Quantity		Refined Value
c lattice parameter (00l) [Å]		12.174(2)
Ti	*z*	0
	occ.	1
Se	*z*	0.121(2)
	occ.	1
Pb	*z*	0.376(1)
	occ.	0.5805
Se	*z*	0.388(1)
	occ.	0.5805
Uiso	[$Å^2$]	0.111(1)
d(Pb-Se, distortion) [Å]		0.15(3)
d(Pb-Se, avg.) [Å]		3.02(2)
d(Pb-Se, interplanar) [Å]		3.13(2)
d(Ti-Se, dichalcogenide) [Å]		1.45(3)
a lattice parameter ($TiSe_2$) [Å]		3.552(7)
a lattice parameter (PbSe) [Å]		6.133(3)
δ(hk0)		0.161(3)
δ(00l)		0.161
Rp (12.503 KeV)		0.1275
Rp (13.199 KeV)		0.0762
Total Rp		0.1041

an arbitrary translation or rotational orientation with respect to the adjacent layers. This structural disorder – layered structures with in-plane crystallinity, chemically and structurally abrupt interfaces, layer-to-layer misregistration, and turbostratic disorder appears to be a consequence of the modulated elemental reactant synthesis approach; we have coined the term *ferecrystal* (from Latin *fere,* meaning *almost*) to describe this new type of structural polymorph.

Room temperature electrical transport properties (electrical resistivity, Seebeck coefficient, and carrier concentration) for four samples are reported in Table IV.3. Sample a and b were synthesized separately from two different depositions. Samples b-1, b-2, and b-3 were deposited at the same time. All values are characteristic of a poor metal or heavily doped semiconductor; the negative sign of the Seebeck coefficient *S* indicates *n*-type conduction, i.e. electrons are the majority carriers. The Seebeck coefficients measured were -69 and -66 μV/K for samples a and b, respectively. Interestingly, the Seebeck coefficient of $(PbSe)_{1.16}TiSe_2$ is approximately 30% larger in magnitude than for $(PbSe)_{1.16}(TiSe_2)_2$,[9] while at the same time the resistivity of the former is almost a factor of ten lower. Similar electrical resistivities $\rho(T)$ were obtained for all four specimens in the range 20 K to 300 K and are shown in Fig. IV.4. The resistivity has an interesting dependence on temperature, first decreasing from 20 K to 100 K then slowly increasing up to 300 K. This change in resistivity may indicate a change in scattering mechanism, possibly due to the static disorder in the sample. The room temperature values are 2.7 mOhm-cm for sample a and the b series of samples ranged from 2.8 to 3.0 mOhm-cm. Unfortunately we could not extend our

measurements to temperatures below 20 K to check for the existence of a superconducting phase, as recently reported for $(PbSe)_{1.16}(TiSe_2)_2$.[9] However, the data of Figure IV.4 are significantly different from resistivity data reported for $(PbSe)_{1.16}(TiSe_2)_2$, which, although also found to be n-type, was reported to have a larger magnitude and stronger metallic temperature dependence.[9] This suggests that the electronic structure and/or doping level for turbostratically disordered $(PbSe)_{1.16}TiSe_2$ are different from crystalline $(PbSe)_{1.16}(TiSe_2)_2$. Although no carrier concentration data was reported in Ref. 9, the model proposed by Giang et al. to describe the electronic structure of $(PbSe)_{1.16}(TiSe_2)_2$ proposes that charge is transferred from PbSe to fill the Ti 3*d* conduction band states associated with the $TiSe_2$ layers. Based on this model one might expect an increased level of Ti 3*d* band filling for the $(PbSe)_{1.16}TiSe_2$ composition relative to $(PbSe)_{1.16}(TiSe_2)_2$.[9] This is consistent with the observed decreased resistivity in $(PbSe)_{1.16}TiSe_2$, however in a rigid band model the Seebeck coefficient would also be expected to be reduced in magnitude, which is in contrast to what we observe. From these observations, we infer that the electrical properties for our composition do not adhere to a simple rigid band picture, and that the electronic structure in the disordered $(PbSe)_{1.16}TiSe_2$ composition is correspondingly different. First principles calculations will be of interest to yield further insight into the electronic properties and the extent of charge transfer.

Table IV.3. Sample designation, room temperature electrical resistivity (ρ), Seebeck coefficient (*S*), carrier concentration (*n*), and Hall mobility (μ_H) for the four $(PbSe)_{1.16}TiSe_2$ samples characterized in this work.

Sample	ρ (mOhm-cm)	*S* (μV/K)	*n* (cm^{-3})	μ_H (cm^2/V-s)
a	2.7	– 69	-	-
b-1	3.0	– 66	2.1×10^{21}	0.8
b-2	2.8	– 66	-	-
b-3	2.9	– 66	-	-

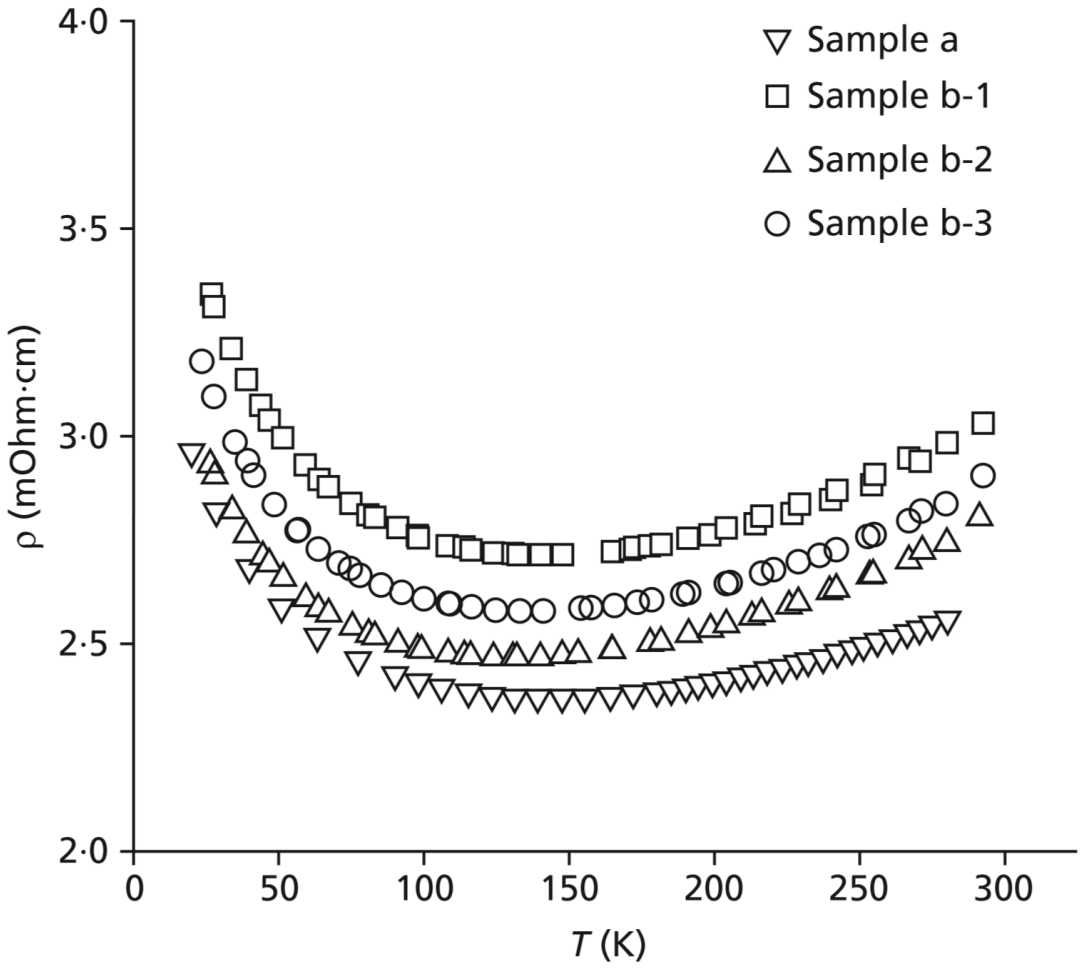

Figure IV.4. Electrical resistivity in the range 20 K to 300 K for four $(PbSe)_{1.16}TiSe_2$ specimens characterized in this work.

Assuming a single carrier type contributes to the electrical transport in $(PbSe)_{1.16}TiSe_2$, we estimated the room temperature carrier concentration *n* from the measured Hall coefficient and the relation $R_H = 1/(ne)$ where *e* is the fundamental charge. The room temperature carrier concentration for specimen b-1 is 2.1×10^{21} cm^{-3}, which is typical of a heavily doped semiconductor or poor metal, and is on the same order of magnitude as the carrier concentrations reported for $(MS)_{1+\delta}(TiS_2)_2$ sulfide compounds with M = Bi, Pb, and Sn.[2] From $\rho = 1/(ne\mu_H)$, we estimate the Hall mobility to be ~1 $cm^2V^{-1}s^{-1}$. This low value may reflect the relatively small in-plane domain sizes associated with turbostratic disorder in $(MSe)_{1+\delta}TSe_2$ intergrowths prepared by MER.[4-6] The relatively high Seebeck coefficient for the measured electron concentration suggests that relatively good electrical transport properties might be achieved in this material system if carrier concentrations can be reduced and carrier mobility improved by, for example, annealing under a controlled atmosphere of the constituents.[24]

IV.4. Conclusions

The new compound $(PbSe)_{1.16}TiSe_2$ is prepared by kinetically trapping the structure from an elementally modulated precursor designed with a repeating period and composition close to that of the targeted structure. The compound consists of interwoven layers of PbSe and $TiSe_2$ that are turbostratically disordered with respect to one another. The positions of atomic layers along the c-axis are similar to those found in conventional crystalline misfit layered compounds. $(PbSe)_{1.16}TiSe_2$ has a room temperature electrical resistivity near 3 mOhm-cm, a Seebeck coefficient in the range -65 to -70 μV/K, and a carrier concentration on the order of 2 x 10^{21}.

IV.5. Bridge

Successful synthesis of the $(PbSe)_{1.16}TiSe_2$ compound lays the foundation for the remaining chapters in this work. The developed synthesis method can be used to attempt to design any member of the $([PbSe]_{1+y})_m(TiSe_2)_n$ family of compounds. However, before compounds with varying m and n values can be compared, it is first important to understand the variation within a single sample synthesized multiple times. The next chapter investigates the reproducibility in structure and electrical transport properties of this compound made several times.

CHAPTER V

PHASE WIDTH OF KINETICALLY STABLE $([PbSe]_{1+y})_1(TiSe_2)_1$ FERECRYSTALS AND THE EFFECT OF PRECURSOR STRUCTURE ON ELECTRICAL PROPERTIES

V.1. Introduction

The high temperatures and long times used in most solid state reactions lead to equilibrium products and an equilibrium distribution of defects and impurity atoms.[1] This leads to the common practice of reporting the properties of a new compounds based on the measurement of a single sample, ideally a single crystal that has been structurally characterized. For metallic compounds with a narrow phase width, subsequent reports usually agree with the initial report, as metallic properties are usually not significantly affected by small changes in the concentration of defects or impurities except at low temperatures.[2] For semiconducting compounds properties often vary significantly between preparations, especially preparations from different groups and even when using near equilibrium synthesis conditions, as small differences in impurity levels and/or defects can significantly vary carrier concentration.[2] An especially large variation in properties is typical when there is a range of compositions within which compounds are stable.[2] As the number of elements within a compound is increased or the structure becomes more complicated, obtaining agreement on properties becomes difficult due to varying distributions of the elements within the ideal composition, impurity atoms, and defects on different crystallographic sites.

The challenges in determining the base properties of ternary intergrowth compounds is especially difficult. An example of this is ternary misfit layer compounds

of the form $(MX)_{1+\delta}(TX_2)_n$, which consist of an intergrowth of a rock salt structure, MX, where M = Sn, Pb, Bi, or RE, and a transition metal dichalcogenide, TX_2 where T = Ti, V, Cr, Nb, and Ta. X is either S or Se and δ represents the difference in the area per cation of the two different structures. Electrical properties for nominally the same compound vary considerably from group to group, even for metallic samples. For example, the resistivity of single crystals of $(PbS)_{1.18}TiS_2$ reported by different groups[3] differs by a factor of 5 and the resistivity of $(SmS)_{1.18}TaS_2$ reported by different groups[3] varies by a factor of 7. The differences in properties of these misfit layer compound crystals is thought to be a consequence of different growth conditions used during vapor transport leading to different amounts of incorporated iodine, other impurities and/or defects. Recently a new synthesis approach was shown capable of preparing intergrowth compounds $((MX)_{1+\delta})_m(TX_2)_n$, where m and n can be systematically controlled by design of a precursor. The structures are different from MLC in that there is rotational disorder between constituents and hence no systematic cooperative structural distortion of the constituent layers. The synthesis route to these compounds is kinetically controlled and the kinetics of the formation reaction will determine the concentration and distribution of defects and impurity atoms.

It is important to understand the reproducibility of the kinetically controlled synthesis of these turbostratically disordered misfit layer compounds, or ferecrystals, before considering the difference between compounds with different m and n values, because small deviations in the product could potentially cause the properties to vary more within different preparations of the same compound relative to compounds with

different m and n values. Here we investigate two sets of $([PbSe]_{1.16})_1(TiSe_2)_1$ samples prepared from a range of different starting precursors and deposited over several months. Although a large variation of precursors was used, we find that they crystallize to nominally the same product, with a small range of c-axis lattice parameters (defined to be along the stacking direction of the intergrowth). It is difficult to determine the precise composition of the majority compound as different trace amounts of secondary phases may form. We find that electrical behavior in the form of resistivity values, Seebeck coefficients, and carrier densities vary from sample to sample and cluster into discreet regions within deposition cycles. The changes in electrical properties correlate with changes in composition. It will be best to look for trends in properties as m and n are varied by taking advantage of the higher level of repeatability within samples prepared in the same deposition cycle.

V.2. Experimental Details

Thin films of the amorphous precursor were deposited on silicon and quartz substrates using a custom built physical vapor deposition system.[4] Selenium was deposited using an effusion cell, whereas lead and titanium were deposited using electron beam guns. The thickness of each elemental layer was monitored using quartz crystal microbalances. Background pressure inside the chamber during film deposition was maintained between 5×10^{-8} and 5×10^{-7} torr for all reported samples. A typical deposition produced a thin film that was approximately 50 nm thick, which consisted of repetitions of the layer sequence Ti – Se – Pb - Se. A second set of samples, prepared much later than the first set, was made with a total thickness of 35 nm. The precursor

was calibrated to contain an excess of 2% Se, as this has previously been shown to produce samples with more intense diffraction patterns.[5] The thickness of each layer in the repeating sequence was calibrated via a method described previously such that each layer self assembles into a $(PbSe)_{1.18}(TiSe_2)_1$ unit cell upon annealing.[6] Samples were annealed on a hot plate at 350°C in a nitrogen atmosphere. Electron-probe microanalysis (EPMA) was used to determine the composition of the thin film samples.[7] Specular X-ray diffraction data were collected using a Bruker D8 Discover diffractometer with Cu Kα radiation.

Thin film specimens for electrical transport properties were deposited on insulating fused silica substrates in order to minimize the influence of the substrate on the measurements. The films were patterned in a standard cross geometry using a shadow mask. Four-probe electrical resistivity (ρ) was measured from 20 K to 300 K in a custom closed-cycle He cryo-system using the van der Pauw technique.[8] Electrical leads were attached using silver epoxy. Seebeck coefficient (*S*) was measured using a differential technique, by determining the slope of applied temperature difference vs. measured voltage difference, corrected for the Seebeck coefficients (*S*) of the copper-constantan thermocouple leads. All reported electrical transport data correspond to the in-plane direction.

V.3. Results and Discussion

Sample precursors were prepared in two deposition cycles to synthesize a precursor which yields a sample after annealing that is crystallographically and compositionally in agreement with the previously reported turbostratically disordered $([PbSe]_{1.16})(TiSe_2)$.[6]

Once a parameter-space close to optimal was found,[96] the depositions were fine-tuned by varying the elemental layer thicknesses of the precursor, which changes the compositions of the precursors. The full width at half maximum of the (002) Bragg reflection was used between depositions as a fast indicator of 1:1 sample quality. Data collected on the samples prepared for this study that formed the 1:1 compound are summarized in Table V.1.

Low angle diffraction patterns are shown in Figure V.1 and indicate little variation is present within deposition cycles. The small variation of critical angle from 0.62 to 0.67 degrees in 2-theta shows little change in density and no correlation was able to be drawn between small shifts in critical angle and composition. Fitting of the high-frequency Keissig oscillations to the Bragg equation modified for refractive contributions results in film thicknesses within 2.5 nm of the targeted values of 50 nm for set 1 and 35 nm for set 2. The angle at which the Kiessig fringes can no longer be resolved is an indicator of the roughness of the films. The increased smoothness seen in the second set of samples is due to diffraction data being collected from samples on a Si substrate as opposed to fused quartz. The changes in rate of decay of the Kiessig fringes between samples is most-likely due to a variance in different substrate's native oxide thicknesses. The first Bragg Peak is seen in all low-angle scans. The peak centers of gravity vary little from 7.27 degrees, corresponding to a d-spacing of 12.15 angstroms and the 001 reflection of the 1:1 ferecrystal.

Table V.1. Summary of all samples as well as data from the previously reported 1:1 compound. Samples from the first deposition cycle, set a, were deposited in order from a1 to a9. Samples from the second deposition, set b, were deposited in order from b1 to b4.

Sample	c-lattice parameter (Å)	Carrier Density (cm^{-3})	Composition		
			Pb/Ti	Pb/Se	Ti/Se
a1	12.181	2.12E+21	0.95	0.36	0.38
a2	12.173	1.76E+21	1.05	0.39	0.37
a3	12.181	2.04E+21	0.88	0.33	0.38
a4	12.167	1.72E+21	1.10	0.38	0.35
a5	12.169	1.71E+21	0.99	0.37	0.37
a6	12.181	1.72E+21	1.07	0.38	0.36
a7	12.170	1.82E+21	0.96	0.36	0.37
a8	12.176	1.86E+21	0.95	0.37	0.38
a9	12.173	2.10E+21	0.98	0.36	0.36
b1	12.188	1.44E+21	0.92	0.40	0.44
b2	12.193	1.07E+21	1.16	0.46	0.40
b3	12.199	1.16E+21	1.08	0.43	0.40
b4	12.194	1.29E+21	0.91	0.40	0.43
Moore 2012[6]	12.174	2.10E+21	1.16	0.37	0.32

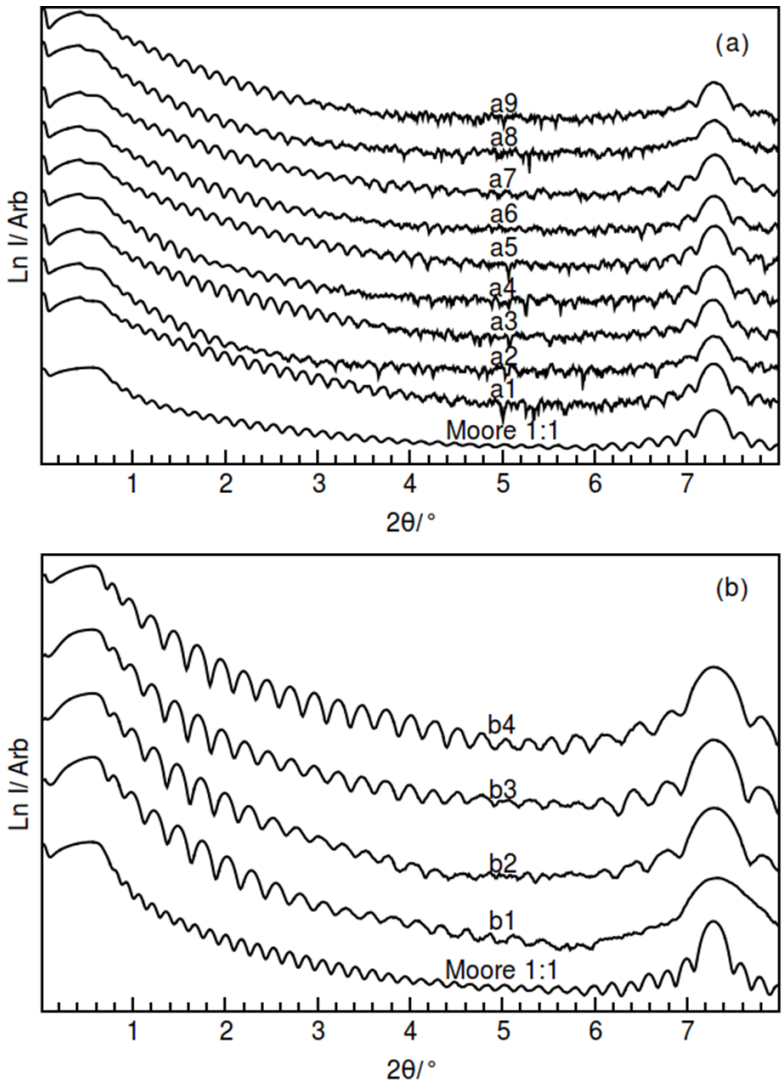

Figure V.1. Low-angle diffraction patterns collected from samples. Data from the Moore 1:1 compound are shown as the bottom curve in each. (a) Set A. The first loss of intensity near the critical angle is a substrate artifact. The critical angle is taken from the second loss. (b) Set B. The apparent amplitude difference is due to the stacking. The range of normalized data is comparable for all samples.

The high angle diffraction patterns (Figure V.2) from both sets of sample also show little variation between samples or deposition cycles. The *c*-lattice parameters of all the samples are within 0.01 Angstroms of the average value and within 0.25% of the previously reported value for the $([PbSe]_{1.16})(TiSe_2)$ ferecrystal. This small change in *c*-lattice parameter correlates weakly with composition changes, trending with the

measured metal (Pb, Ti) to Se ratio. The increased FWHM of the samples from the second deposition cycle is due to fewer layers in the (00*l*) direction in which the crystallite size is limited by the thickness of the film. The lack of any (*hkl*) reflections with $h, k \neq 0$ in an out-of-plane geometry is characteristic of ferecrystal samples due to the crystallographic alignment of the samples with the substrate. The similarity of the diffraction patterns suggests a similar average structure for all of the samples. There is some variation in the relative intensities of peaks throughout both sets of samples, with the largest variations within 50% of the average relative intensity for each peak. These changes in relative intensity suggest a variation in the occupancy of specific locations reflecting the different compositions of the precursors.

Electrical measurements are more sensitive to impurity phases or local crystalline defects than x-ray measurements. Prior literature suggests charge transport occurs mainly in the conduction band of the transition metal dichalcogenide constituent. We expect changes in impurity and defect concentration would alter the carrier density of the semimetallic $TiSe_2$. Table V.1 contains the room temperature resistivity of the samples. The composition and resistivity data from both sets of samples cluster in nearby but discrete regions of parameter space, distinct also from the previously published compound. The variation of the extrema from the average value is ±40% within sample set A and ±30% within sample set B. There is a factor of 2 difference between the averages of the resistivity values of the two data sets, with the extrema from the entire experiment spanning a 400% change. The resistivity values were found to trend with the Pb/Se ratio, as shown in Figure V.3. The variation in room temperature

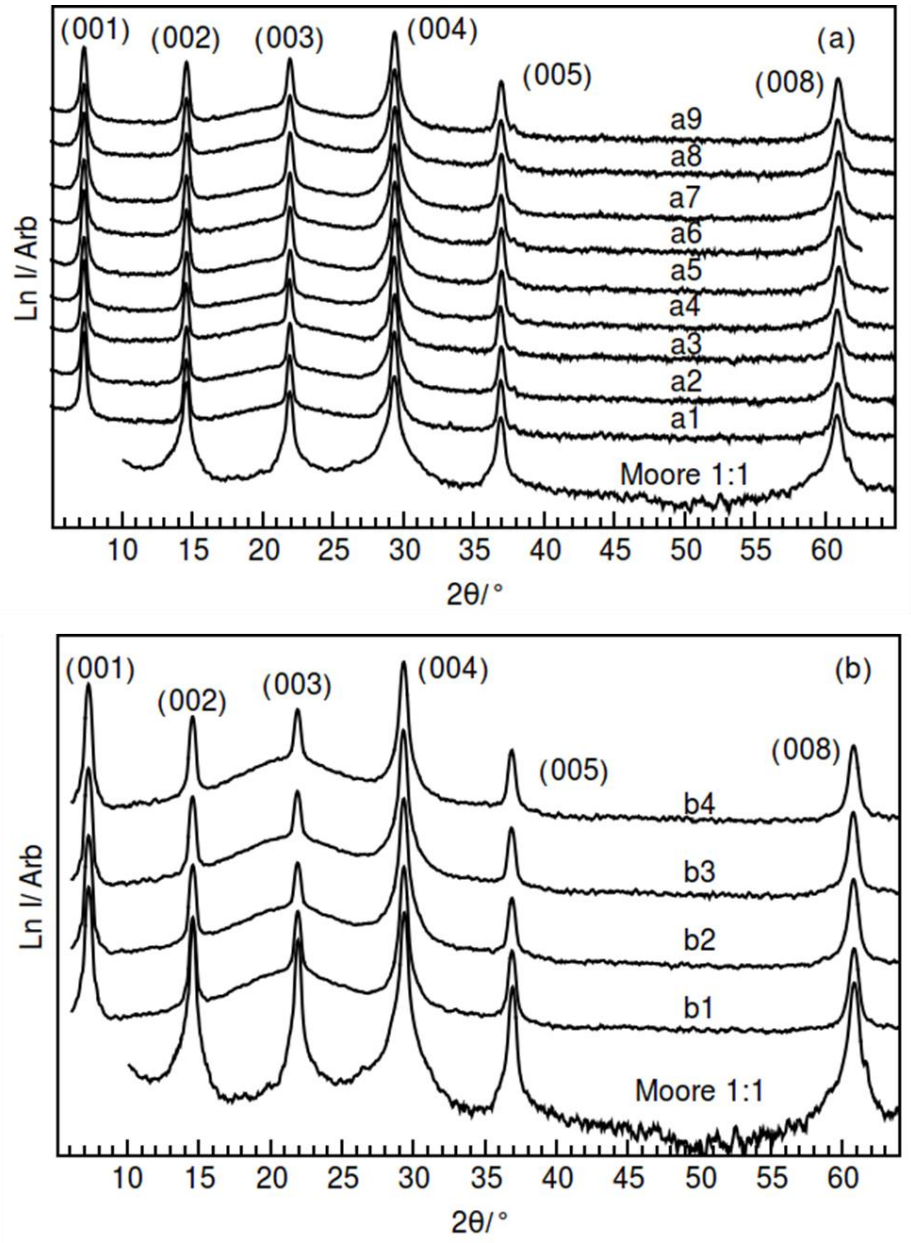

Figure V.2. High angle specular diffraction patterns collected from samples in (a) set A and (b) set B. Data from the Moore 1:1 compound are shown for comparison as the bottom curve in each pane. The apparent difference in scales is due to a reduced range in the pane with fewer curves.

resistivity (400%), however, is smaller than that reported for different single crystals of misfit layer compounds (500-700%). This is somewhat surprising, as the MLC crystals were grown under nearly equilibrium conditions while the self-assembly of our precursors is a kinetic process. This suggests that in the self-assembly, some of the

excess elements are clustered in inclusions rather than being dispersed as local defects throughout the film. The larger variation between depositions also suggests that it would be better to make samples with different m and n in the same set to correlate nanoarchitecture with properties.

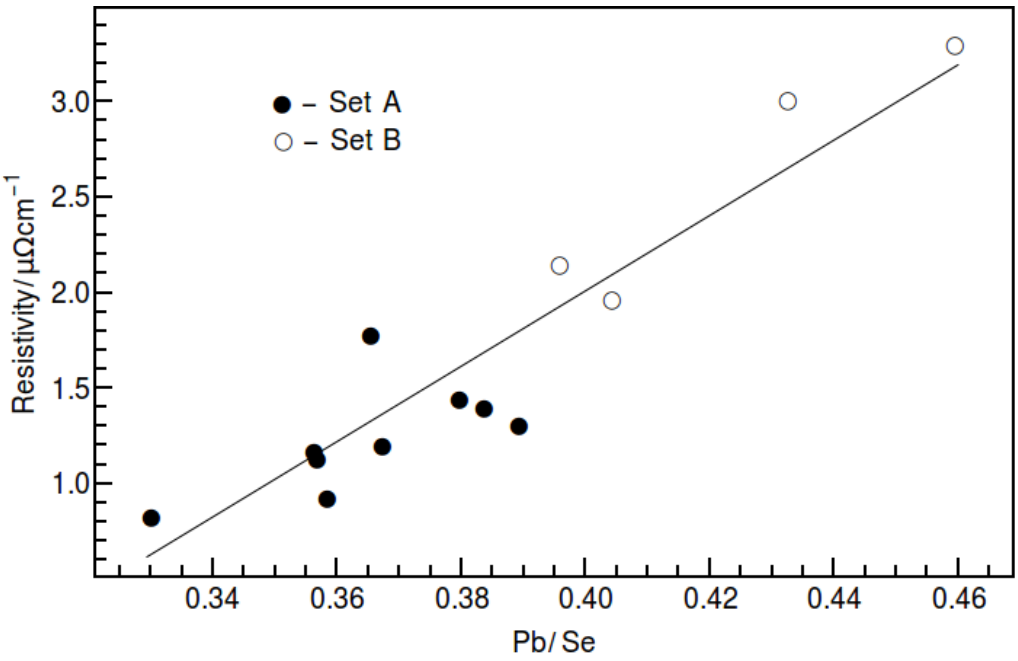

Figure V.3. Sample resistivity values cluster in two regions for the two sample sets and trend with Pb/Se ratio. The line is provided as a guide to the eye.

Temperature dependent resistivity data, collected for most of the compounds studied, are shown in Figure V.4. The temperature dependence is very similar for all samples and indicates metallic behavior. The temperature dependence of the electrical resistivity can be modeled using the Bloch-Grüneisen equation as expected for a metal,

$$\rho(T) = \rho_0 + \Re\left(\frac{T}{\theta_D}\right)^5 \int_0^{\frac{\theta_D}{T}} \frac{z^5}{(e^z - 1)(1 - e^z)} dz$$

where ρ_0 is the residual resistivity, $\Re$ is the electron-phonon interaction constant, and θ_D is the debye temperature. The very weak temperature dependence indicates a small

electron phonon interaction constant, reflecting the lack of long range order found for compounds prepared by self-assembling designed precursors. This disorder, and the resultant lack of phonons, results in the low lattice thermal conductivity of ferecrystals. The variation of the residual resistivity with both sample set and composition is similar to that of the room temperature values, discussed above. There is evidence for a slight upturn in the resistivity at the lowest temperatures measured, but this upturn is smaller than previously reported.

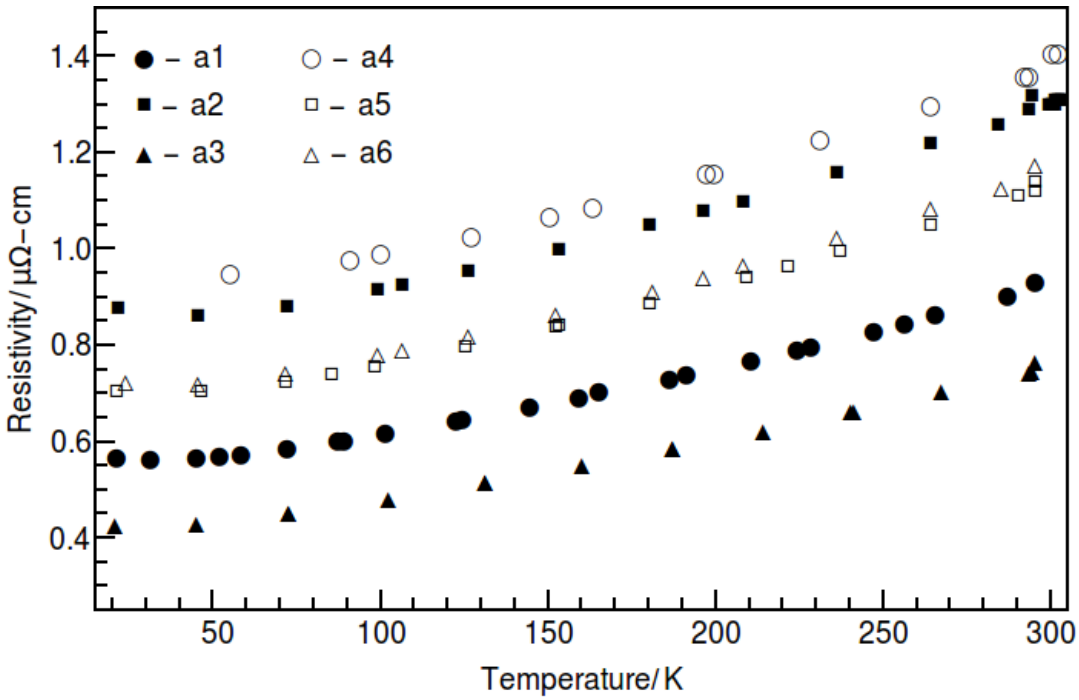

Figure V.4. Variable temperature resistivity data for select ferecrystal samples from set A. Curvature is very similar in all cases, with the value differences in magnitude roughly scaling with carrier concentration.

To gain further information on the electrical properties, Hall coefficients were measured at room temperature for all samples. All samples exhibit a negative Hall coefficient indicating conduction via electrons, which is consistent with prior suggestions of charge donation to $TiSe_2$ from PbSe.[6] Following prior literature reports,

the Hall coefficients were converted to carrier concentration assuming a single band model.[3] Carrier concentrations are reported for all samples in Table V.1 and are shown as a function of temperature on a subset of samples (Figure V.5). Room temperature carrier concentration for each deposition varies by 15% from the average value and there is a factor of 1.5 between sets. Carrier concentration has a linear downward trend with cation impurity, suggesting reduced donation of charge into the dichalcogenide layer. The variation of the carrier concentration with temperature may be a consequence of assuming a single band model to calculate carrier concentrations. A change in charge transfer with temperature would be expected and lead to the observed weak temperature dependence.

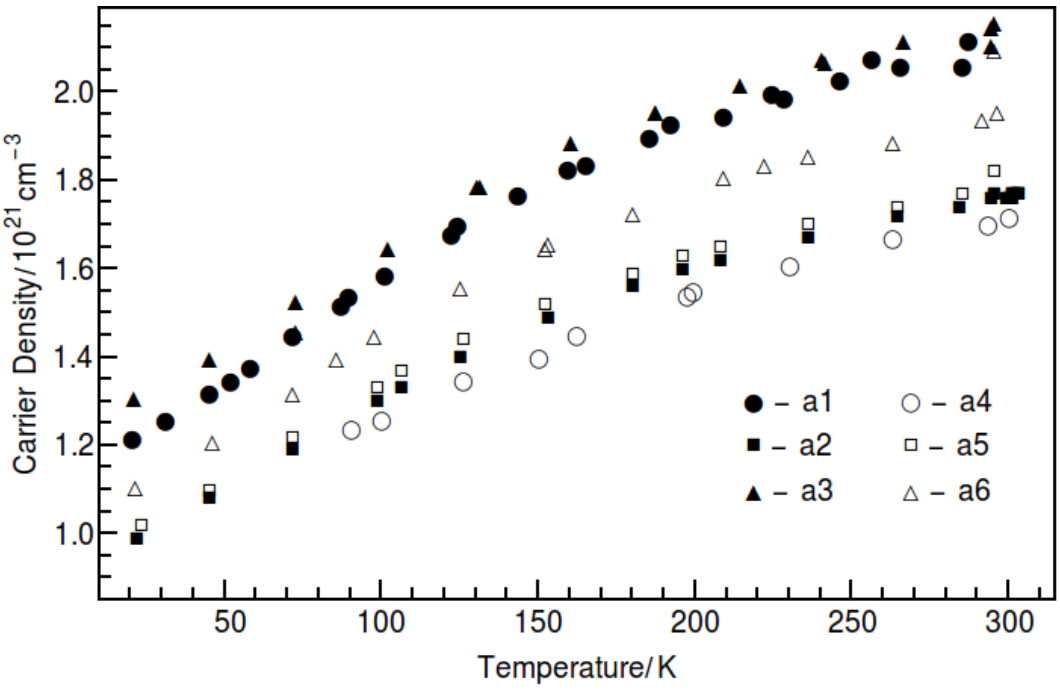

Figure V.5. Carrier concentration as a function of temperature for a subset of samples. The gentle change is typical of a metallic band structure.

Hall mobilities calculated from carrier concentration and resistivity measurements vary between 1.8 and 3.8 $cm^2V^{-1}s^{-1}$. The mobility increases with carrier

concentration, which is unusual for doping because dopant atoms usually cause scattering. However, this is consistent with charge donation from PbSe to $TiSe_2$, where conduction occurs in a location spatially separated from the dopant. The mobility decreases as the Pb/Se ratio increases.

Seebeck coefficients were all negative, consistent with Hall coefficient in indicating that electrons are the majority carrier. The magnitude of the Seebeck coefficients vary by about 2.5 μV/K within a set of samples with the values of each set clustered around averages 5 μV/K apart. As expected, the magnitude of the Seebeck coefficient increases as carrier density is reduced. Assuming a parabolic band with acoustic scattering, the effective mass can be determined from the Pisarenko relationship,[10]

$$\alpha = \frac{8\pi^2 k_B^2}{3eh^2} m^* T \left(\frac{\pi}{3n}\right)^{\frac{3}{2}}$$

Where α is the Seebeck voltage, k_B is the Boltzmann constant, e is the elementary charge, h is Planck's constant, m^* is the effective mass, T is the absolute temperature, and n is the carrier concentration. The average carrier mass was found to be $4.4m_e$ and $3.6m_e$ for sets A and B respectively, both lower than calculated from data on the previously reported 1:1 compound ($5.5m_e$). Figure V.6 graphs the correlation between the Seebeck coefficient and the carrier concentration at 295K. The Seebeck coefficient is relatively insensitive to the Hall determined carrier concentration. The solid curves show the values expected from the Pisarenko relationship for the minimum, maximum, and average effective masses. The lowest effective masses correspond to samples with a high cation (Pb, Ti)/Se ratio. The changes in m^* reflect the shortfall of assuming a single

band model to obtain carrier concentration or that the band becomes more disperse with increased impurity concentration. Additional investigations will be required, both to understand modulation doping and how to use it in band structure engineering of ferecrystal compounds.

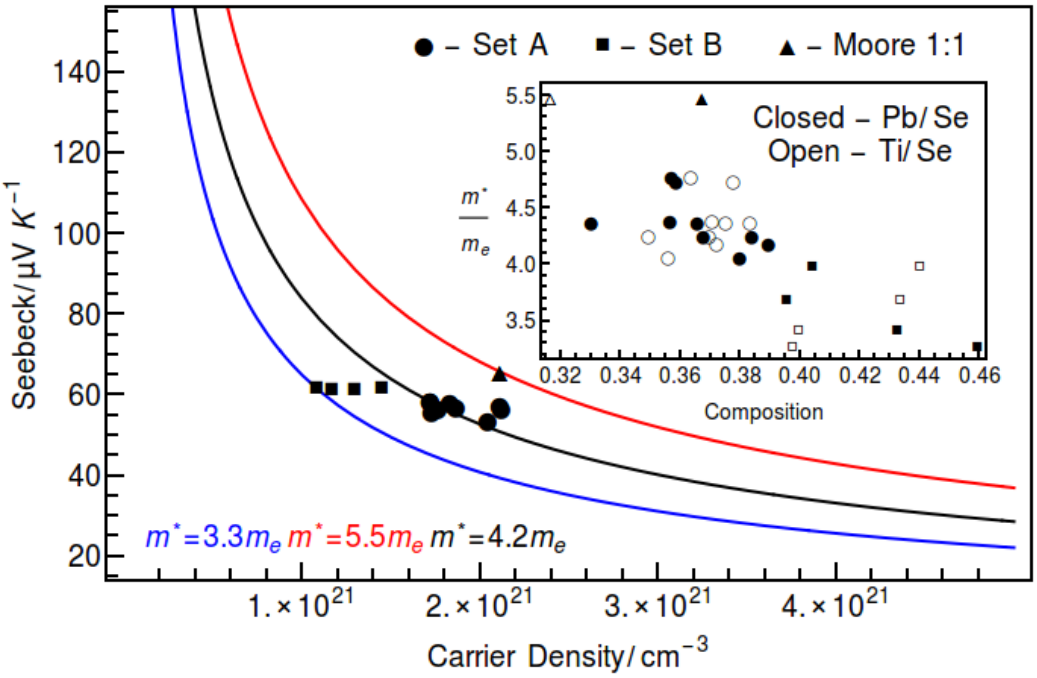

Figure V.6. Room temperature carrier density plotted against Seebeck coefficients for all samples. The solid curves indicate the expected relationship for different effective masses assuming a single rigid parabolic band.

V.4. Conclusion

$([PbSe]_{1.16})_1(TiSe_2)_1$ forms over a range of initial precursor parameters resulting in a very narrow range of *c*-axis lattice parameters, suggesting a narrow phase width for this compound. The resistivity was found to vary by a factor of two, with the change correlating with the Pb/Se ratio. The Seebeck coefficient was consistent within a set of samples prepared in the same deposition cycle. The unusual temperature dependence of the carrier concentration and unusual variation in the effective mass calculated from

the Seebeck coefficients and the carrier concentration suggest that using a single band approximation to convert Hall coefficients to carrier concentration may be a poor assumption. The small change in electrical properties between ferecrystal samples relative to the large difference between reports of single crystals of misfit layered compounds, especially within a set of samples in the same deposition cycle, is encouraging for future experiments that explore how properties vary as compounds with different values of n and m are prepared.

CHAPTER VI

SYNTHESIS, STRUCTURE, AND PROPERTIES OF TURBOSTRATICALLY DISORDERED $(PbSe)_{1.18}(TiSe_2)_2$

This work was published in volume 25 of Chemistry of Materials in 2013 with co-authors Matt Beekman, Sabrina Disch, Paul Zschack, Ines Hausler, Wolfgang Neumann, and David C. Johnson. Matt Beekman assisted in analysis of electrical data, Sabrina Disch provided the Rietveld and le Bail analysis, Paul Zschack assisted in X-ray diffraction analysis at the Advanced Photon Source Ines Haeusler and Wolfgang Neumann provided analysis of the electron diffraction, David C. Johnson is my advisor and research group leader, and I am the primary author.

VI.1. Introduction

Misfit layered compounds are layered intergrowths between two constituents, typically a rock salt structured material and a transition metal dichalcogenide. The chemical formula that describes these compounds is generally written as $[(MX)_{1+\delta}]_m(TX_2)_n$ where X is a chalcogen, M is Sn, Pb, Bi or a rare earth metal, T is a group IV, V, or VI transition metal, and δ reflects the difference in the in-plane packing density of the two constituents. Misfit layered compounds have traditionally been synthesized by grinding stoichiometric amounts of powders together and heating at high temperatures for long periods of time, suggesting that they are thermodynamically stable compounds. Traditionally synthesized misfit layered compounds typically have one or two in-plane axes where the constituents have different lattice parameters,

necessitating higher dimensional crystallography to describe their structures.[1] Giang et al.[2] recently reported the synthesis of a new misfit layered compound $(PbSe)_{1.16}(TiSe_2)_2$ using the above mentioned conventional high temperature bulk synthesis route, followed by distillation to remove the PbSe secondary phase that formed with the desired product. $(PbSe)_{1.16}(TiSe_2)_2$ has a metallic resistivity that decreases as temperature is lowered, becoming superconducting at 2.3K.[2]

Recently it has been shown that new metastable layered intergrowth compounds can be synthesized using the modulated elemental reactant (MER) method.[3] These new compounds differ from misfit layered compounds by having turbostratic disorder,[4] meaning each layer has an arbitrary rotational orientation with respect to adjoining layers. To differentiate these two classes of compounds, the term ferecrystal (from Latin fere, meaning 'almost') has been proposed to describe this new layered structure type, poised between an amorphous and crystalline solid. The turbostratic disorder results in unusual and/or unique properties, such as extremely low thermal conductivity,[5] that are not found in conventional misfit layered materials.

Elucidating their chemical and physical similarities and dissimilarities with respect to conventional misfit layered compounds is a key step toward advancing the understanding of the chemistry and physics of ferecrystal compounds. Reported here is the synthesis of the $(PbSe)_{1.18}(TiSe_2)_2$ ferecrystal and the direct comparison of its structure and electrical properties with the analogous crystalline misfit layered compound, $(PbSe)_{1.16}(TiSe_2)_2$.[2] Diffraction data of this MER created compound along the *hk*0, 00*l*, and *hkl* (h, $k \neq 0$; $l \neq 0$) directions and TEM data are consistent with a precisely

layered structure, with in-plane crystallinity and order, abrupt interfaces between the PbSe and $TiSe_2$ constituents, layer-to-layer misregistration, and turbostratic disorder. The electrical properties of the ferecrystal are found to be significantly different than those of the misfit layered compound, attributed to the turbostratic disorder between the constituent layers.

VI.2. Experimental Details

Thin films of the amorphous precursor were deposited on silicon substrates using a custom built physical vapor deposition system.[6] Deposition of selenium was accomplished using an effusion cell, whereas lead and titanium were deposited using electron beam guns. The thickness of each elemental layer was monitored using quartz crystal microbalances. Background pressure inside the chamber during film deposition was maintained between 5×10^{-8} and 5×10^{-7} torr for all reported samples. A typical deposition produced a thin film that was approximately 50nm thick, which consisted of 28 repetitions of the layer sequence Ti – Se – Ti – Se – Pb – Se. The precursor was calibrated to contain an excess of 2% Se, as this has previously been shown to produce samples with more intense diffraction patterns.[4] The thickness of each layer in the repeating sequence was calibrated via a method described previously such that each layer self assembles into a $(PbSe)_{1.18}(TiSe_2)_2$ unit cell upon annealing.[7] Samples were annealed on a hot plate at 350°C in a nitrogen atmosphere. Electron-probe microanalysis (EPMA) was used to analyze the composition of the thin film samples.[8] The mole fraction Pb:Ti:Se determined by EPMA analysis was 14:20:65, in agreement

with the ideal composition of 14:24:62 for $(PbSe)_{1.18}(TiSe_2)_2$, within experimental uncertainty.

Thin film specimens for electrical transport properties were deposited on insulating fused silica substrates in order to minimize the influence of the substrate on the measurements. The films were patterned in a standard cross geometry using a shadow mask. Four-probe electrical resistivity (ρ) was measured from 20 K to 300 K in a custom closed-cycle He cryo-system using the van der Pauw technique.[9] Electrical leads were attached using silver epoxy. Seebeck coefficient (*S*) was measured using a differential technique, by determining the slope of applied temperature difference vs. measured voltage difference, corrected for the Seebeck coefficients (*S*) of the copper-constantan thermocouple leads. All reported electrical transport data correspond to the in-plane direction.

Specular X-ray diffraction data were collected using a Bruker D8 Discover diffractometer with Cu Kα radiation. Area X-ray diffraction data were collected at the 6-ID-D beamline of the Advanced Photon Source (APS) using high energy X-rays (86.76 keV). Approximate correlation lengths ξ were determined from the Gaussian peak widths in [00*l*] direction and corrected for instrumental resolution according to $\frac{1}{\xi} = \sqrt{HWHM_{sample}^2 + HWHM_{instrument}^2}$ As a reference for the instrumental resolution, a NIST 640c Si standard was measured (FWHM = 0.0145(1) $Å^{-1}$). High resolution X-ray diffraction was measured at the 33-BM-C beamline of the APS using an X-ray energy of 12.9 keV and a point detector, with orientation of the scattering vector *Q* either

perpendicular (00*l* reflection series) or parallel (*hk*0 reflection series) to the substrate. Refinements according to the Le Bail[10] and Rietveld[11] approaches have been carried out using the GSAS program package.[12,13]

Cross-section specimens for the high-resolution transmission electron microscopical (HRTEM) investigations were prepared by focused ion beam milling using an FEI Helios Nanolab D600. The *in situ* lift-out was accomplished using an Omniprobe 200. All specimens were cut out and thinned down to 300nm at 30kV. The subsequent thinning process was done at 5kV, followed by cleaning the specimens at 2kV, with a final cleaning at 1kV. HRTEM and electron diffraction studies were carried out on an FEI aberration-corrected Titan 80-300 equipped with an objective lens C_s corrector.
The transmission electron diffraction (TED) patterns were analysed by means of the software of the ASTAR/DigiSTAR system from NanoMEGAS. The determination of the various orientations of the individual PbSe and $TiSe_2$ crystallites in the layers was performed by comparing each experimental diffraction pattern with a large number of computer simulated diffraction patterns (templates) comprising all possible orientations. The number of templates depends on the symmetry of the unit cell and the desired angle resolution for the orientation determination. Here, the templates were generated with an angle step size of approximately 1°. For the highly symmetric PbSe (space group $Fm\bar{3}m$), the number of generated templates was 1326. Due to the lower crystallographic symmetry (space group $P\bar{3}m1$) the number of generated templates of $TiSe_2$ was 10404.

VI.3. Results and Discussion

An annealing study was carried out to determine the optimal annealing conditions to form the targeted $(PbSe)_{1.18}(TiSe_2)_2$ ferecrystal via self-assembly of the designed thin film precursor. In this study, one sample was deposited on silicon and then cleaved into several pieces. Each piece was annealed under nitrogen at a specific temperature for 30 minutes and out-of-plane diffraction data was collected ex-situ at room temperature. Figure VI.1 contains the diffraction patterns collected after annealing at the indicated temperatures. The low angle diffraction pattern of the as deposited sample contains the expected (001) Bragg diffraction maxima originating from the elementally layered precursor. Higher order low-intensity reflections are already present in the as-deposited sample as well, suggesting that the precursor is very precisely layered and that the product has to some extent begun to form under the ambient conditions of precursor deposition. Reflection intensity increases with annealing temperature up to 350 °C and the reflections shift to higher angle as the *c*-axis lattice parameter decreases. This suggests that the repeating layers becoming slightly thinner as they self-assemble to form the ferecrystal due to more efficient atomic packing and the loss of excess selenium. Above 350 °C, the ferecrystal reflections are reduced in intensity and after annealing at 450 °C only reflections from the binary PbSe compound remain. These data indicate that the turbostratically disordered ferecrystal is not a thermodynamically stable product. Subsequent samples were annealed at 350°C, which was considered the optimum temperature for self-assembly of the ferecrystal based on diffraction intensities.

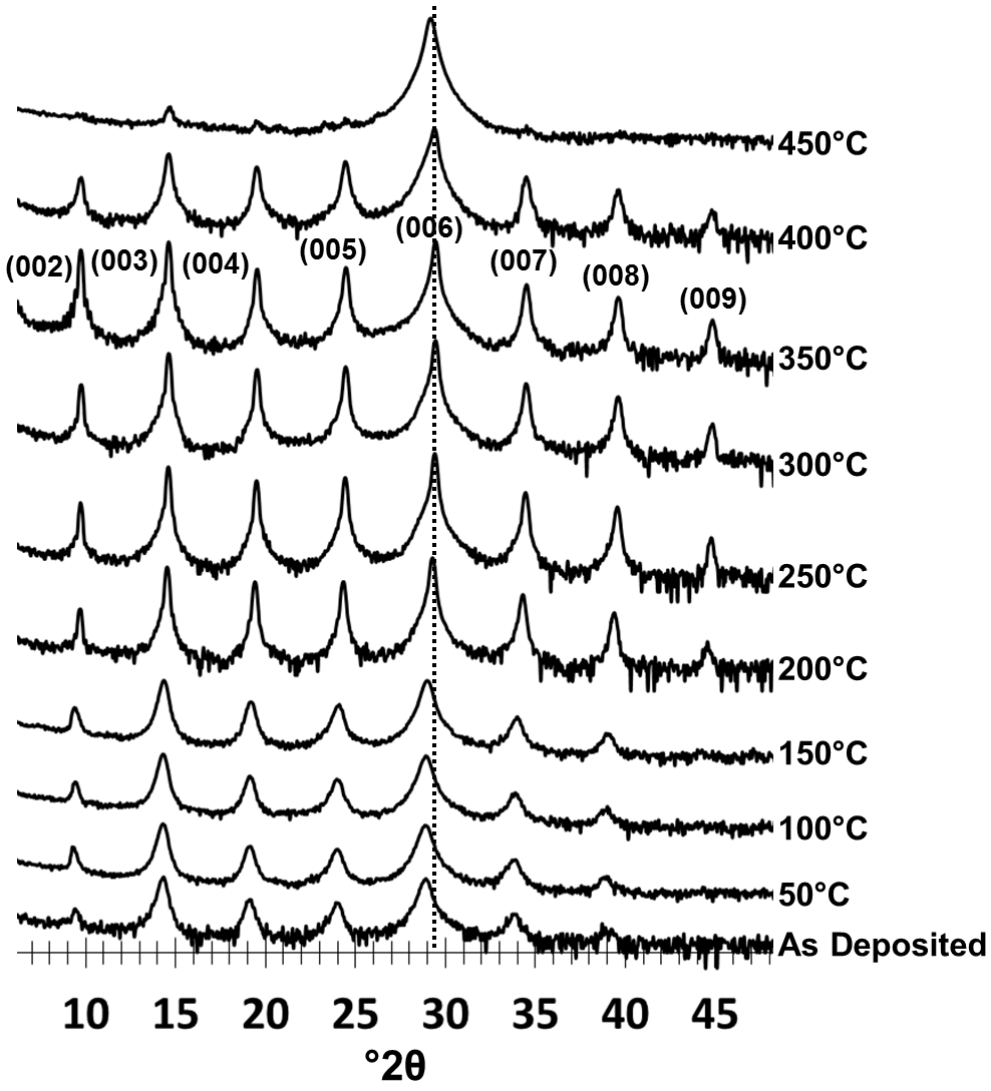

Figure VI.1. Specular diffraction scans collected after annealing a precursor at the indicated annealing temperatures for 30 minutes. Data are plotted in a log scale. The dashed vertical line is included to highlight the shift of reflections to higher angle with higher annealing temperature.

Reciprocal space mapping of a 350 °C annealed $(PbSe)_{1.18}(TiSe_2)_2$ sample using high energy X-rays confirms the strong preferred orientation of the ferecrystal with respect to the substrate, the interleaved structure of the components, and the turbostratic disorder of the individual PbSe and $TiSe_2$ layers (Figure VI.2). High energy X-rays were used in order to minimize absorption effects of Pb. At the same time, this allows access

to a significant amount of diffraction information in a wide range of reciprocal space. The 00*l* reflection series is observed exclusively for orientation of the scattering vector *Q* perpendicular to the substrate ($Q_{x,y}$ = 0), whereas the *hk*0 reflection series of the individual binary constituents are observed at orientation of the scattering wave vector parallel to the substrate (Q_z = 0). All *hkl* reflections of the binary compounds appear simultaneously without rotation of the sample during data acquisition, revealing a random in-plane orientation of domains of the individual ferecrystal layers, whereas no off-axis reflections originating from the overall intergrowth structure have been observed. The extremely low degree of azimuthal smearing of the sharp (00*l*) reflection series, however, indicates a high degree of crystalline order in a preferred orientation perpendicular to the substrate as in a two dimensional powder with near-perfect azimuthal alignment.

The different correlation lengths perpendicular to the substrate give evidence for turbostratic disorder of the ferecrystal layers. The (*hkl)* reflections of the binary compounds exhibit a diffuse intensity distribution along Q_z with a much broader peak width than observed for the (00*l)* reflections, indicating a shorter correlation length of the individual layers perpendicular to the stacking direction as compared to the ferecrystal intergrowth superstructure. Analysis of the peak width of the (00*l)* reflection series (FWHM = 0.0206(2) $Å^{-1}$) leads to a structural correlation length of 13.6(5) nm, in the order of magnitude of the entire sample thickness and close to the instrumental resolution limit. The much broader peak width of the (*hkl)* reflections in [00*l*] direction (FWHM = 0.22(1) $Å^{-1}$) relates to a structural correlation length of only 0.90(8) nm,

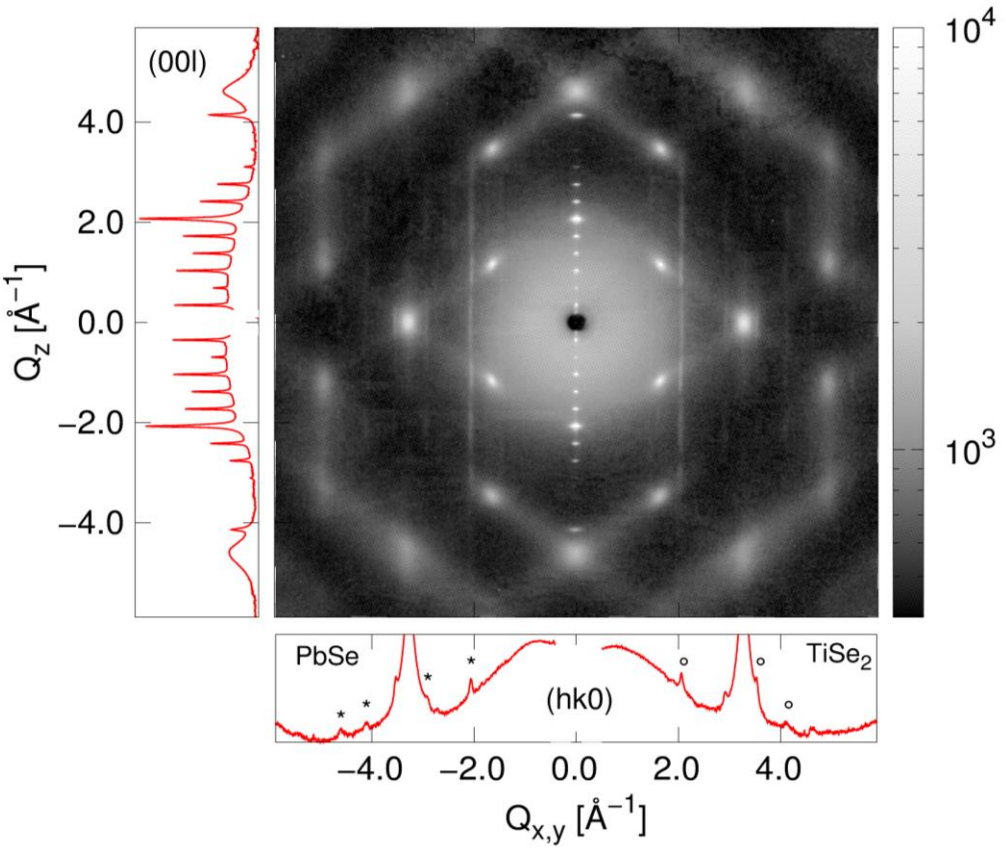

Figure VI.2. High energy synchrotron X-ray diffraction data from the $(PbSe)_{1.18}(TiSe_2)_2$ ferecrystal. Intensity projections of the (*00l*) reflection series ($Q_{x,y} = 0$) and the (*hk*0) reflection series ($Q_z = 0$) are shown on the left and bottom, respectively. The higher symmetry pattern of broad reflections originates in thermal diffuse scattering of the silicon substrate and is inconsequential in the analysis of the ferecrystal structure.

corresponding to the individual layer thickness. This indicates that there is long range order in the stacking of the PbSe and $TiSe_2$ layers, whereas there is no or low atomic correlation between the individual layers. These data reveal that the PbSe and $TiSe_2$ layers are precisely stacked, yet stack with little to no in-plane registry from layer to layer.

The incommensurate nature of conventional misfit layered compounds has historically presented significant challenges to their structural characterization, resulting in the application of superspace crystallographic approaches to structure refinement.[1] Elucidation of the structure of our $(PbSe)_{1.18}(TiSe_2)_2$ ferecrystal is further complicated by the lack of long range order in this material (cf. Figure VI.2). To gain further insight into the structure, we collected synchrotron X-ray diffraction scans in the (00*l)* and (*hk*0) directions. Analysis of the (*hk*0) reflection series by Le Bail refinement yields the in plane lattice parameters of the binary constituents, PbSe with a square in-plane lattice (a_{PbSe} = 0.6122(4) nm), and $TiSe_2$ with a hexagonal in-plane lattice (a_{TiSe2} = 0.3568(2) nm). These lattice parameters correspond well to those reported for bulk PbSe (0.6121 nm)[14] and $TiSe_2$ (0.3533 nm)[15] and the misfit layered compound.[2] The lattice parameter obtained for PbSe is also consistent with that previously reported for PbSe containing misfit layered compounds.[3] From the determined in-plane cell parameters, the misfit parameter for the ferecrystal is calculated to be δ = 0.177(1). This value lies well within the range of literature reports for MLCs which range from 0.07 to 0.28, but the largest value reported to date for ferecrystalline compounds, which range between -0.01 to 0.16.[4,16–18]

Analysis of the synchrotron X-ray diffraction scans in (00*l)* direction yields a ferecrystal lattice parameter of c_{FC} = 1.8257(2) nm, which is in good agreement with the corresponding c parameter for the misfit layered compound.[2] Rietveld structure refinement using this reflection series yields the atomic structure profile perpendicular to the substrate, *i.e.* projected atomic layer distances instead of atomic positions (Figure

VI.3). Our results reported in Table VI.1 indicate deviations of the atomic planes from the bulk structure of both the PbSe and $TiSe_2$ binary compounds. As commonly observed in conventional misfit layered compounds, we find that the PbSe layers in the ferecrystal exhibit a displacement of the Pb and Se atoms in opposite directions, with the Pb atoms approaching the neighbouring dichalcogenide layers. The refined distance between the Pb and Se layers is determined to be 0.062(5) nm, which is in the upper range of distortion distances previously observed for misfit layered compounds.[19–22] In the dichalcogenide constituent, different Ti-Se interlayer distances are observed, with the shorter (0.143(2) nm) Ti-Se interlayer distance neighbouring to the PbSe layer and the longer (0.156(2) nm) Ti-Se interlayer distance neighbouring the $TiSe_2$ layer. When averaged, the distance corresponds well to the Ti-Se interlayer distance observed in bulk $TiSe_2$. The relative displacement of Ti in this ferecrystal, where the two $TiSe_2$ trilayers are bordered by PbSe double layers, may be the result of energetic compensation for the finite size of the layer thickness, as is the distortion in the rock salt layers. The Pb ions also interact with the Se of the $TiSe_2$, producing an asymmetric arrangement of Se layers in the dichalcogenide as observed by the different Se-Ti interlayer distances. In contrast to the rock salt layer distortion, the asymmetric arrangement of the dichalcogenide layers has not been observed this significantly by single crystal structure determination of $(MX)(TX_2)_2$ misfit layered compounds (i.e. $(PbS)_{1.18}(TiS_2)_2$,[23] $(PbS)_{1.14}(NbS_2)_2$,[24,25] $(PbSe)_{1.12}(NbSe_2)_2$,[26] and $(LaSe)_{1.14}(NbSe_2)_2$[27]). It may thus likely be enhanced by the turbostratic disorder of the ferecrystal compound. The van der Waals gap between the $TiSe_2$ layers in the ferecrystal is determined as 0.318(1) nm, significantly larger than

observed in the bulk compound (0.30 nm). Both the van der Waals gap and the variation of the Ti-Se distances have been verified from HRTEM measurements (*vide infra*).

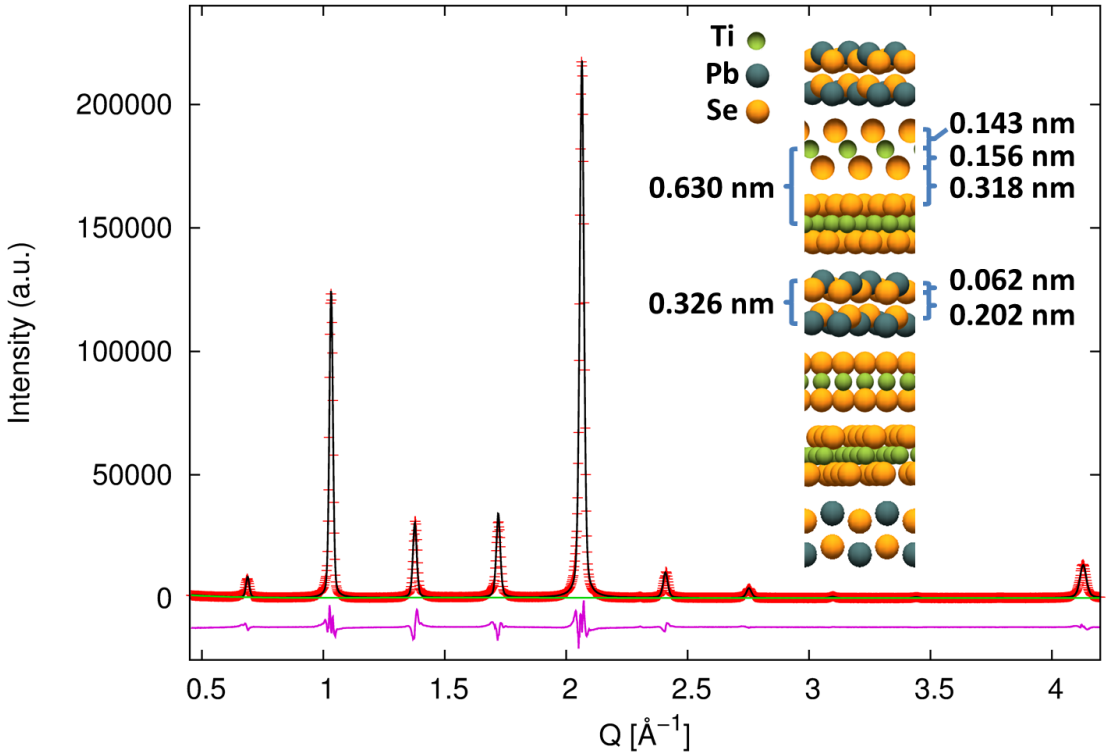

Figure VI.3. Rietveld refinement of the (00*l*) synchrotron X-ray diffraction data of $(PbSe)_{1.18}(TiSe_2)_2$. Observed, calculated, and difference intensities are shown in red, black, and purple, respectively. Inset: Representation of the turbostratically disordered structure, with the refined arrangement of the atomic planes along the *c* direction. Characteristic atomic distances determined from the refinement are indicated.

HRTEM studies confirm the XRD results that the structure of the ferecrystal $(PbSe)_{1.18}(TiSe_2)_2$ consists of alternating double PbSe layers and two $TiSe_2$ layers as given for a conventional misfit layer compound (Figure VI.4). Figure VI.4 clearly shows that, in contrast to conventional misfit layer compounds, the orientation of the PbSe and $TiSe_2$ layers varies not only from layer to layer along the intergrowth direction but also within the PbSe and $TiSe_2$ layers. Some of the areas of PbSe and $TiSe_2$ layers are well oriented

Table VI.1 Results from Rietveld and le Bail refinements of the $(PbSe)_{1.18}(TiSe_2)_2$ ferecrystal. Included are lattice parameters, *c*-axis positions (*z*) for each atom, site occupancies, important interplanar distances and refinement residuals.

Quantity	**Refined value**
c-lattice parameter [nm]	1.8257(2)
Se	
z	0.0555(3)
occ.	0.588
Pb	
z	0.0894(1)
occ.	0.588
Se	
z	0.2493(2)
occ.	1
Ti	
z	0.3274(2)
occ.	1
Se	
z	0.4128(1)
occ.	1
δ (00*l*)	0.176
Rp (00*l*) (12.9 keV)	0.106
d(Pb-Se)	0.062(1)
d(Ti-Se) (towards Pb)	0.143(1)
d(Ti-Se) (towards Ti)	0.156(1)
a-lattice parameter (PbSe) [nm]	0.6122(3)
a-lattice parameter ($TiSe_2$) [nm]	0.3568(2)
δ (*hk*0)	0.177(1)
Rp (*hk*0) (12.9 keV)	0.045
d, interplanar distances; occ., site occupancies; z, z-axis positions for each atom.	

so that the structure of the double rocksalt layers and the paired trilayers of $TiSe_2$ are imaged very well. It is obvious that larger parts of $TiSe_2$ are well oriented whereas the PbSe double layers are more misoriented. The computer analysis of the SAED pattern

(Figure VI.5) provided the best matching between the experimental pattern and the simulated templates for the following orientations of $TiSe_2$ [01.0], [11.0].

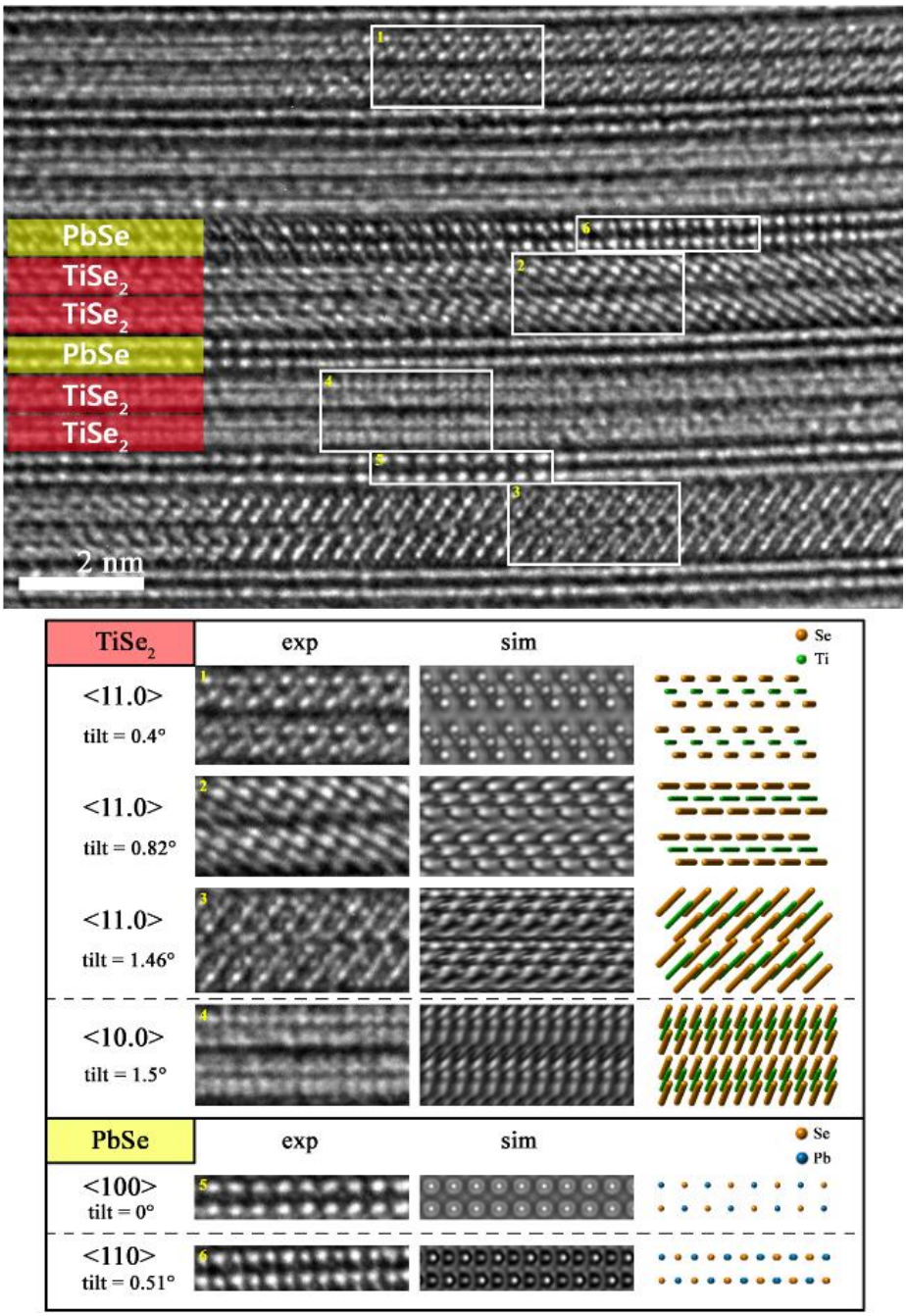

Figure VI.4. Cross-sectional HRTEM micrograph of ferecrystal $(PbSe)_{1.18}(TiSe_2)_2$ grown on Si (100) substrate.

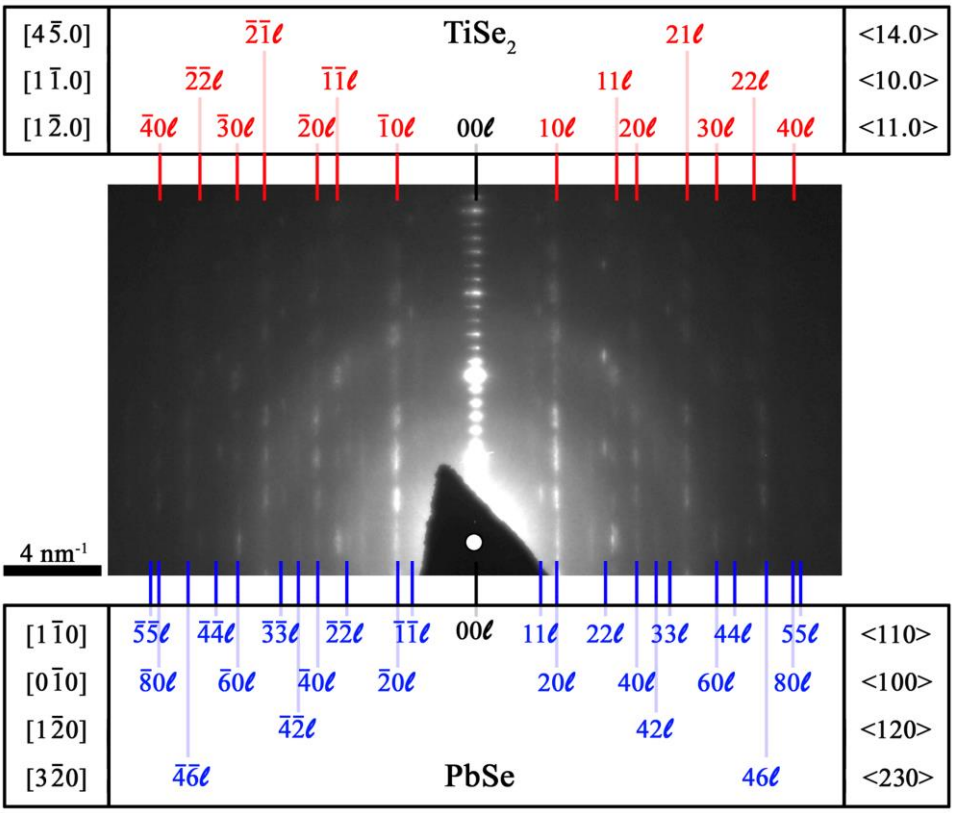

Figure VI.5. Selected-area electron diffraction pattern of the ferecrystal $(PbSe)_{1.18}(TiSe_2)_2$.

In order to determine the various orientations of the different grains in the layers and to see if they are correlated at all we have analysed the selected area diffraction pattern in Figure VI.5 using the approach of Rauch.[28,29] This essentially provides a map of average orientation of the crystallites similar to what is obtained by electron backscatter diffraction analysis. Figure VI.6 shows the cross correlation index map for $TiSe_2$. It displays the degree of matching of the experimental TED to the whole stack of related $TiSe_2$ templates. High degrees of correlation are dark in such maps. The map itself represents the symmetry invariant part of the stereographic projection. In the case of the $TiSe_2$ phase, the dark areas are well defined and located on the outer circle of the correlation map which is synonymous with the primitive circle in the crystallographic

stereographic projection. Indexing of the dark areas in Figure VI.6 reveals for the $TiSe_2$ layers two strongly preferred orientations: <01.0> and <11.0>. These two preferred orientations correspond to rotations about the c-axis of the unit cell. Due to the tiny thickness of the PbSe layer, there are only weak reflections, which are spread out in reciprocal space which makes identifying preferred orientations more challenging.

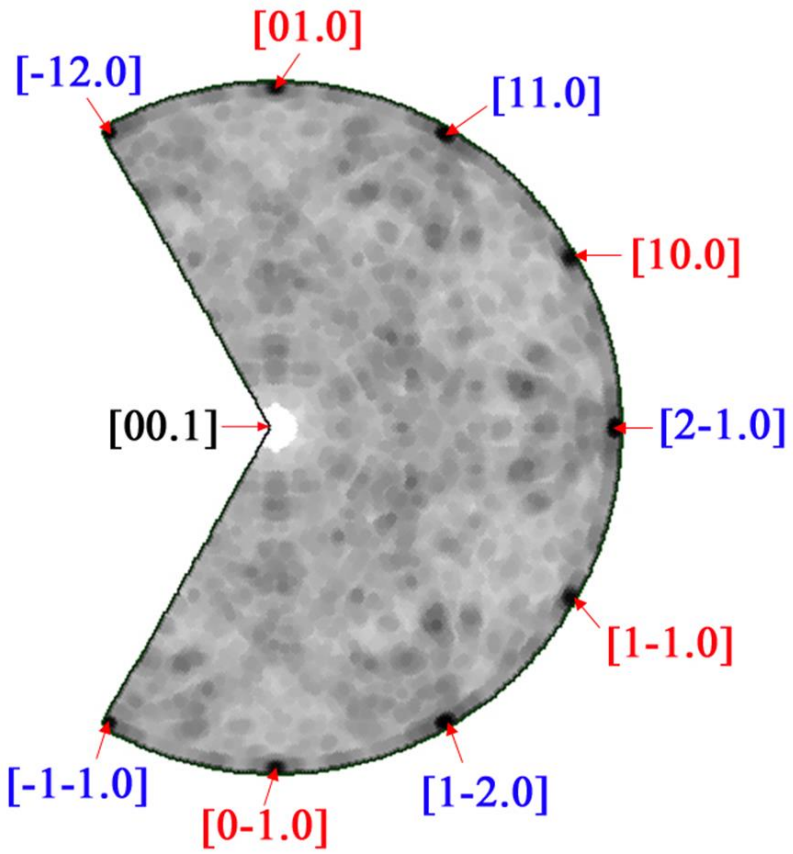

Figure VI.6. Cross correlation index map for $TiSe_2$. Note that this map is rather flat, indicating a very high degree of correlation.

The influence of the structural disorder on the electrical properties of the $(PbSe)_{1.18}(TiSe_2)_2$ ferecrystal was probed by measurements of the in-plane resistivity (ρ) and Seebeck coefficient (*S*) of the $(PbSe)_{1.18}(TiSe_2)_2$ ferecrystal film and compared to reported values for the corresponding crystalline misfit layered compound. The room

temperature electrical resistivity (Figure VI.7) of the ferecrystal was found to be a factor of 9 lower than that measured for a single crystal of the $(PbSe)_{1.16}(TiSe_2)_2$ misfit layered compound,[2] which is somewhat surprising given that the high density of interfaces in the in-plane direction due to turbostratic disorder in the ferecrystal might be expected to increase interface scattering thus reducing mobility. The resistivity of the ferecrystal weakly decreases with increasing temperature below 100 K and weakly increases with increasing temperature above 150 K. with ρ_{300}/ρ_{20} of 0.8. In contrast, Giang et al. reported a monotonically increasing resistivity as temperature is increased, with a residual resistivity ratio of nearly 19 for their single crystal, indicating the composition is a good metal. The reported residual resistivity (near 1 mOhm-cm) and room temperature resistivity (near 20 mOhm-cm) for the single crystal misfit layered compound are at the same time larger than commonly observed for metallic compounds. The $(PbSe)_{1.16}(TiSe_2)_2$ misfit layered compound was reported to undergo a superconducting transition at 2.3 K[2]. We were unable to extend our resistivity measurements to temperatures below 20 K, hence it remains an open question whether or not the superconducting transition still occurs in the ferecrystal.

The room temperature value of *S* for the $(PbSe)_{1.18}(TiSe_2)_2$ ferecrystal was found to be – 91 μV/K, suggesting electrons are the majority charge carriers for this composition. This is in agreement with the sign of the Seebeck coefficient observed for the misfit layered compound, $S = -50$ μV/K near 300 K[2] Giang et al.[2] qualitatively explained the negative Seebeck coefficient using a rigid band model for $(PbSe)_{1.16}(TiSe_2)_2$. By analogy with Cu_xTiSe_2, they suggested that PbSe acts as an intercalant in $TiSe_2$, donating charge

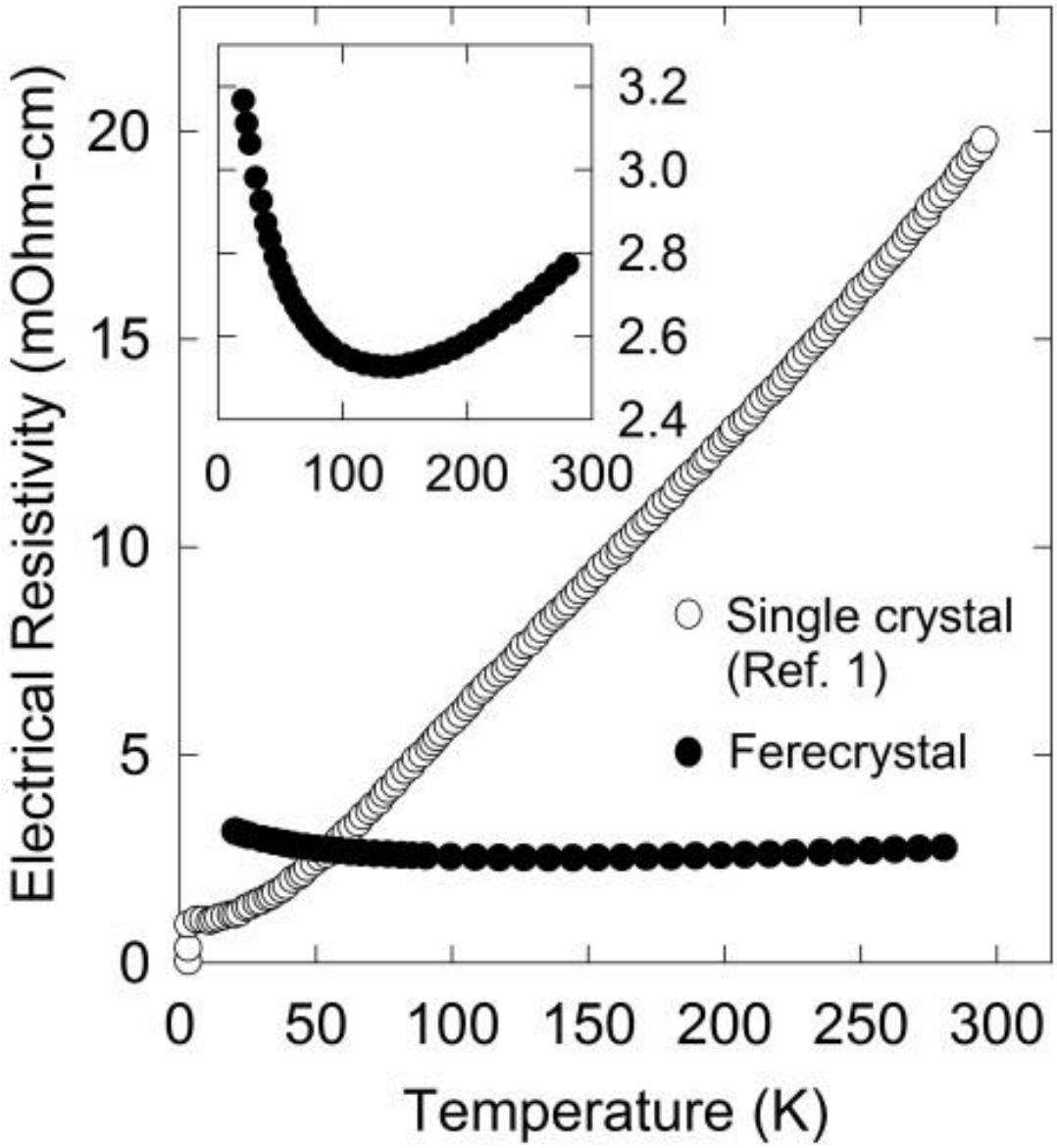

Figure VI.7. Temperature dependence of the electrical resistivity of the $(PbSe)_{1.18}(TiSe_2)_2$ ferecrystal and single crystal $(PbSe)_{1.16}(TiSe_2)_2$.[1] Inset (same units as main figure): Expanded plot of the resistivity of the ferecrystal.

to the $TiSe_2$ layers. This model predicts partial occupation of bands derived from Ti 3*d* states and *n*-type conduction. While the Seebeck coefficients for both materials are negative, the absolute value of *S* measured in our ferecrystal film is significantly larger than that observed for the polycrystalline specimen of the misfit layered compound

$(PbSe)_{1.16}(TiSe_2)_2$, which is somewhat surprizing given the significantly lower room temperature electrical resistivity of the ferecrystal. The lower resistivity yet higher Seebeck coefficient observed for the ferecrystal relative to the corresponding misfit layered compound is unusual and indicates the potential of such structures for thermoelectric enhancement. The power factor of a thermoelectric material is given by the ratio S^2/ρ. The power factor of the ferecrystal film is larger than the corresponding misfit compound by a factor of nearly 30. This could suggest that the mobility of the carriers in the ferecrystal is significantly higher than in the misfit compound, again surprising given the rotational disorder at the interfaces and the small in plane grain sizes of the constituents. A more complete understanding of the physical reasons for the increase in power factor may shed light on novel mechanisms for thermoelectric enhancement.

VI.4. Conclusion

The compound $(PbSe)_{1.18}(TiSe_2)_2$ was synthesized using modulated elemental reactants and structurally characterized as a disordered variant of a misfit layered compound. The structure contains interleaved layers of a distorted rock salt structured PbSe bilayer alternating with pairs of transition metal structured Se-Ti-Se trilayers, similar to that reported for the $(PbSe)_{1.16}(TiSe_2)_2$ misfit layered compound but with little to no correlation between the layers. The electrical properties of the misfit layered compound and the disordered ferecrystal are surprisingly different, with the ferecrystal having a significantly higher room temperature conductivity and Seebeck coefficient. The ferecrystal also has a much smaller temperature dependence of the conductivity.

VI.5. Bridge

Designed synthesis has been used to successfully create the first two members of the $[(PbSe)_{1+\delta}]_m(TiSe_2)_n$ family of compounds. The electrical properties of these compounds vary significantly from the misfit layer compound containing the same elements. In order to investigate both the designed synthesis and unique electrical properties of these compounds, many more members of this family were synthesized. The first nine members of the $[(PbSe)_{1+\delta}]_m(TiSe_2)_n$ family of compounds with m and n values 1 – 3 are reported in the following chapter.

CHAPTER VII

INVESTIGATING THE ELECTRICAL PROPERTIES WITHIN THE $[(PbSe)_{1+\delta}]_m(TiSe_2)_n$ FAMILY OF FERECRYSTALS (m, n = 1-3)

Several people contributed to work presented in this chapter. Matt Stolt made several samples of Set B as an undergraduate in the lab. Kat Hansen was responsible for the electrical measurements taken on Set B during her Summer REU. Ann Greenaway (Rotation student) and Daniel Berg (Undergraduate) collected the electrical data for Set C. Jeff Ditto prepared samples for STEM and collected the images.

VII.1. Introduction

Chemists routinely use synthesis techniques that take advantage of controlling reaction pathways to obtain kinetic products. Solution based chemistry relies heavily on multistep reactions and low temperature synthesis to prepare complex, kinetically stable compounds. Solid state synthesis, however, has typically been limited to thermodynamically stable products because high temperatures are typically used to overcome slow solid state diffusion rates. Even when using solution routes to produce precursors, a final high-temperature heating step is typically needed to form the desired crystalline product. Ternary compounds present further challenges as it is necessary to find conditions where the desired three-element phase is more stable than a mixture of the binary compounds and/or elements. A quaternary phase must be more stable than a mixture of elements, binary and ternary products.

The modulated elemental reactant synthesis method was developed to overcome thermodynamic limitations by dramatically reducing required diffusion lengths, trapping kinetic products that are otherwise not obtainable. This approach uses thin elemental layers in a repeating sequence to create a precursor that has diffusion lengths on the order of Angstroms as opposed to the many microns in typical solid state synthesis. The thickness of the elemental layers are adjusted to obtain the desired composition. With short diffusion lengths, the correct composition and the correct sequence of elemental layers, precursors can be annealed at low temperatures to self-assemble into the targeted, kinetically stable compound. By designing precursors with regions with distinct composition differences, it is possible to prepare compounds containing two intergrown structures. These $([MSe]_{1+\delta})_m(TSe_2)_n$ compounds, referred to as ferecrystals because of the extensive rotational disorder between the constituent layers, have interesting electrical properties that are quite different from their crystalline misfit layer compound analogs.[1]

With the modulated elemental reactant synthesis method, we have the opportunity to synthesize and investigate a wide assortment of different compounds within the $([PbSe]_{1+y})_m(TiSe_2)_n$ family of ferecrystals. We have previously reported[2] how different the electrical properties are between the turbostratically disordered ferecrystal $([PbSe]_{1.18})_1(TiSe_2)_2$ and the misfit layer compound analogue.[3] Here we report the synthesis, structure and how the electrical properties systematically change as m and n are varied. There are practically an infinite number of compounds that are possible within the $([PbSe]_{1+y})_m(TiSe_2)_n$ family. By investigating the first nine compounds

of this family, trends in the electrical properties can be evaluated to understand how the constituents interact electronically to affect the resulting properties of the film. With this data, predictions of other compounds in the family can be made and synthesis can be directed toward specific areas of interest.

VII.2. Results and Discussion

Through the iterative calibration process described in detail in Chapter II, we found the experimental conditions such that sequentially deposited elemental Ti -Se layers and Pb-Se layers have both the composition and absolute thickness to self-assemble into individual layers of $TiSe_2$ and PbSe respectively. By depositing the Ti-Se layers n times and the Pb-Se layers m times the compounds $([PbSe]_{1+\delta})_m(TiSe_2)_n$ can in principle be prepared. In this study we prepared the precursors for the first nine compounds in the $([PbSe]_{1+\delta})_m(TiSe_2)_n$ ferecrystal family, with m and n = 1 - 3. Cartoon representations of these nine compounds are shown in Figure VII.1. This set of compounds was prepared two different times and five compounds were synthesized a third time for this study (23 total samples). These sets will be referred to as sets A, B, and C in the following discussion.

An annealing study was carried out on the precursor of $([PbSe]_{1.16})_3(TiSe_2)_3$ to determine the best conditions to self-assemble the targeted compounds. Figure VII.2 shows the out-of-plane XRD of the $([PbSe]_{1.16})_3(TiSe_2)_3$ precursor annealed at the indicated temperature. A previously unannealed piece of a film from a single deposition was used for each temperature. Samples were placed on a hotplate at the desired temperature

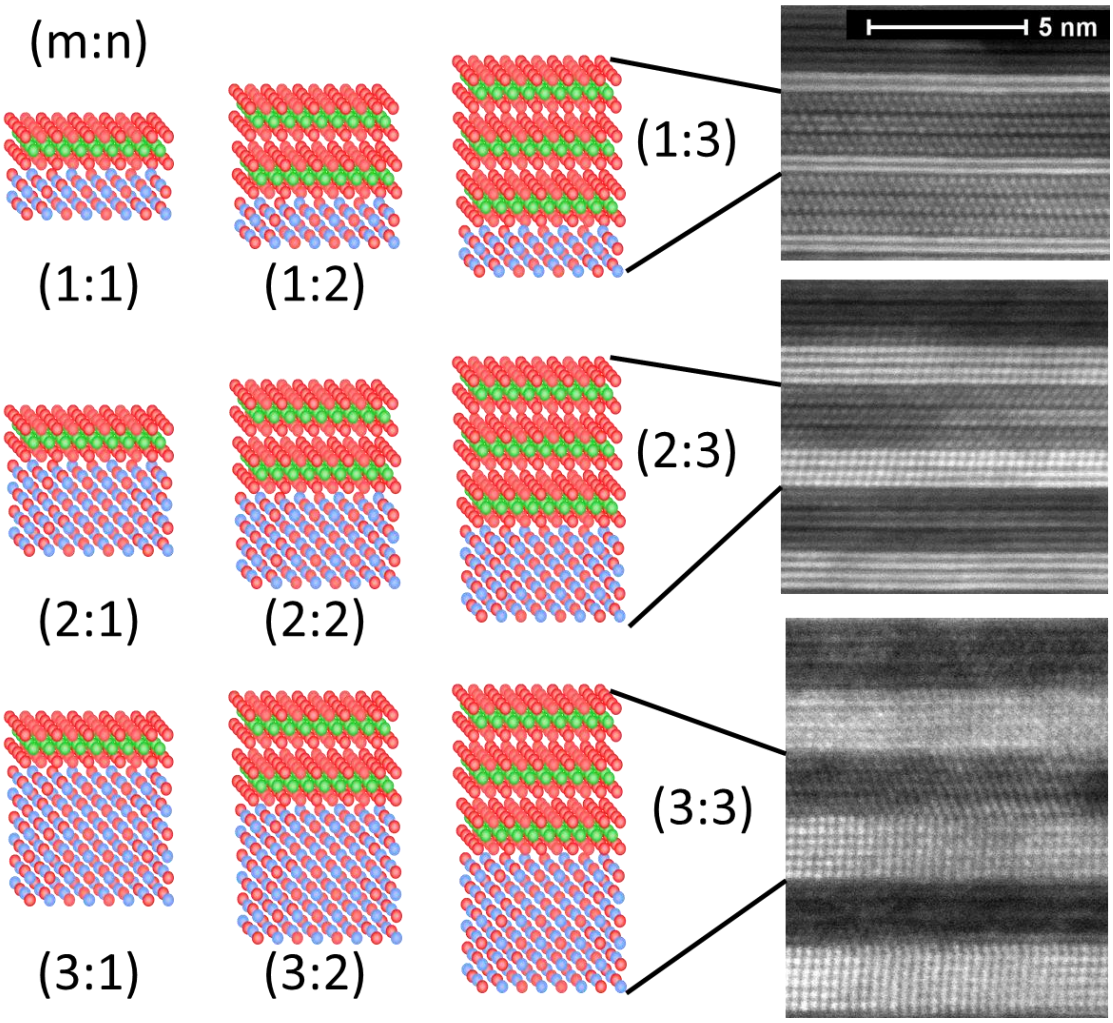

Figure VII.1. Cartoon representations of each $[(PbSe)_{1+\delta}]_m(TiSe_2)_n$ sample described are shown to the left, with the m and n values given in parenthesis, (m : n). On the right are STEM images of the indicated compounds where the lines connect the carton representation of a unit cell to the corresponding region in the image. Each image shows 3 unit cells of the compound.

inside a glove box with a nitrogen atmosphere (H_2O and O_2 0.6 ≤ ppm) for 30 minutes.

The as-deposited sample already shows some peaks for the superlattice, indicating significant order in the sample before annealing. From 50-150°C, the peaks begin to sharpen slightly and shift to higher angles, indicating the lattice parameter is decreasing, but the changes are small. This is typical of MER precursors containing an excess of

selenium, which is driven out of the film at elevated temperatures.[4] At 250°C, additional peaks of the superlattice are apparent, indicating the order in the precursor is increasing. Peaks continue to sharpen to 350°C, at which point they are the narrowest and most intense. At 400°C the peak intensity begins to slightly decrease as the compound begins to decompose. This decomposition continues as temperature is raised and by 500°C only peaks belonging to the parent compounds ($TiSe_2$ and PbSe)

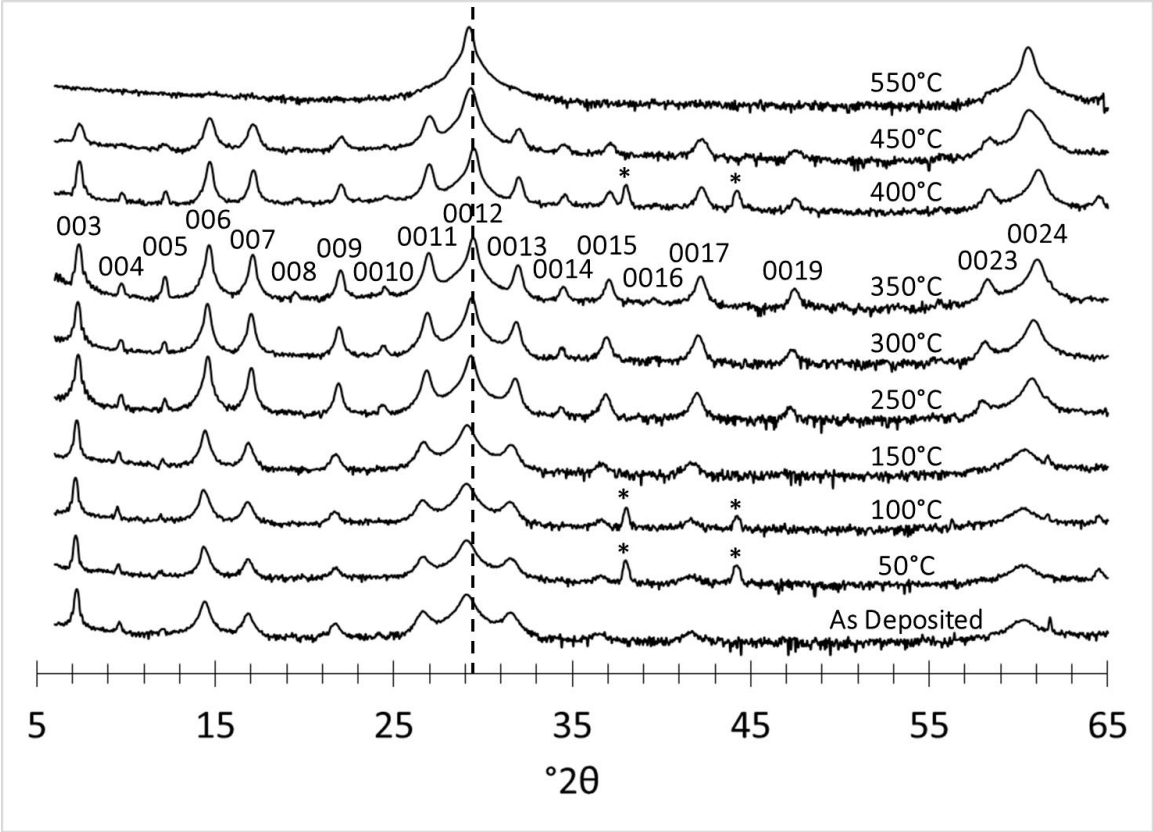

Figure VII.2. Stacked out-of-plane X-ray diffraction scans for the precursor that formed $([PbSe]_{1.16})_3(TiSe_2)_3$. Data are plotted on a log scale. Data were collected after a piece of the precursor was annealed for 30 minutes at the indicated temperature. The vertical dashed line is centered on the 0012 peak for the formed ferecrystal and shows the subtle changes in *c*-axis lattice parameter with annealing. * indicates diffraction from the stage of the diffractometer.

remain. From this study, and in agreement with previous results reported for ([PbSe]$_{1.16}$)$_1$($TiSe_2$)$_1$[5] and ([PbSe]$_{1.18}$)$_1$($TiSe_2$)$_2$,[2] 350°C is ideal to form the ([PbSe]$_{1.16}$)$_3$($TiSe_2$)$_3$ compound and was used to anneal the remainder of the samples.

STEM images of three representative samples from sample set B annealed at 350 °C are shown in Figure VII.1. It is clear from these images that the compounds are layered, containing regions of PbSe and $TiSe_2$. Turbostratic disorder between layers is also evident by the random sequence of different crystal faces visible. In some layers the (100) PbSe is clearly seen while in layers above or below, separated by $TiSe_2$, the layer is rotated and the crystal face is no longer apparent. For compounds with more than one $TiSe_2$ layer, each $TiSe_2$ layer seems to form a finite piece of a 1T polytype that also have different orientations in each layer, consistent with the results seen for the binary compound synthesized from modulated elemental reactants.[6]

The out-of-plane XRD for the nine samples of set B is shown in Figure VII.3. All the peaks for each sample can be indexed as (00*l*) reflections, indicating that the products are crystallographically aligned with their *c*-axis perpendicular to the substrate. Using the indices shown in Figure VII.3, the *c*-axis lattice parameters for the compounds in all 3 sets were calculated and are tabulated in Table VII.1. The lattice parameters systematically increase as the number of $TiSe_2$ or PbSe repeats is increased. The change per $TiSe_2$ unit (0.59) nm is in close agreement to the reported value of (0.6002) nm for the binary compound $TiSe_2$.[7] The change per PbSe unit (0.62) is also close to the value reported for the binary PbSe, (0.6128) nm.[8]

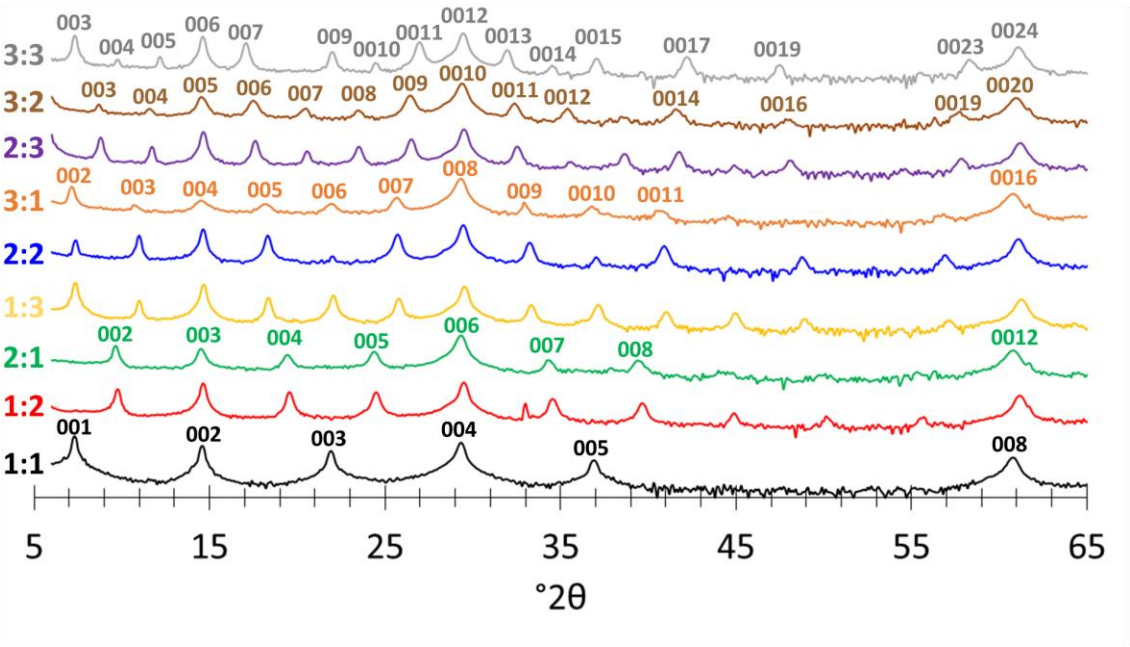

Figure VII.3. Stacked out-of-plane X-ray diffraction scans for Set B.

Table VII.1. *c*-axis lattice parameters, in Angstroms, for each sample in this study.

		Sample Set		
m	n	A	B	C
3	2	30.91(7)	30.4(1)	-
2	3	30.33(4)	30.25(6)	-
3	3	36.37(9)	36.37(6)	36.36(7)
2	2	24.32(3)	24.21(5)	24.30(2)
3	1	24.55(8)	24.50(2)	-
2	1	18.32(4)	18.29(5)	-
1	3	24.29(5)	24.19(1)	24.18(1)
1	2	18.22(5)	18.17(1)	18.17(4)
1	1	12.183(5)	12.18(1)	12.18(1)

In-plane XRD experiments were conducted at the Advanced Photon Source, Argonne National Labs. Figure VII.4 shows grazing incidence scans for five samples of set A. The diffraction peaks seen in-plane can all be indexed to the constituents of the ferecrystal, PbSe and $TiSe_2$, with the relative intensity changing as expected based on

the layering scheme. The lattice parameters obtained from these scans are given in Table VII.2. The PbSe and $TiSe_2$ *a*-axis lattice parameters are very close to the reported values for these compounds (PbSe = 6.128,[8] TiSe2 = 3.536[7]). From the in-plane lattice parameters, the misfit can be determined and is included in Table VII.2. The misfit is consistent with previous misfits reported for compounds from this family of ferecrystals.[2,5] The in-plane diffraction scan is powder-like, meaning it shows a low degree of texture in the *hk*0 direction, this is further evidence of the turbostratic disorder. A single crystal specimen, without this rotational disorder between layers, would not show reflections in the grazing incidence geometry used.

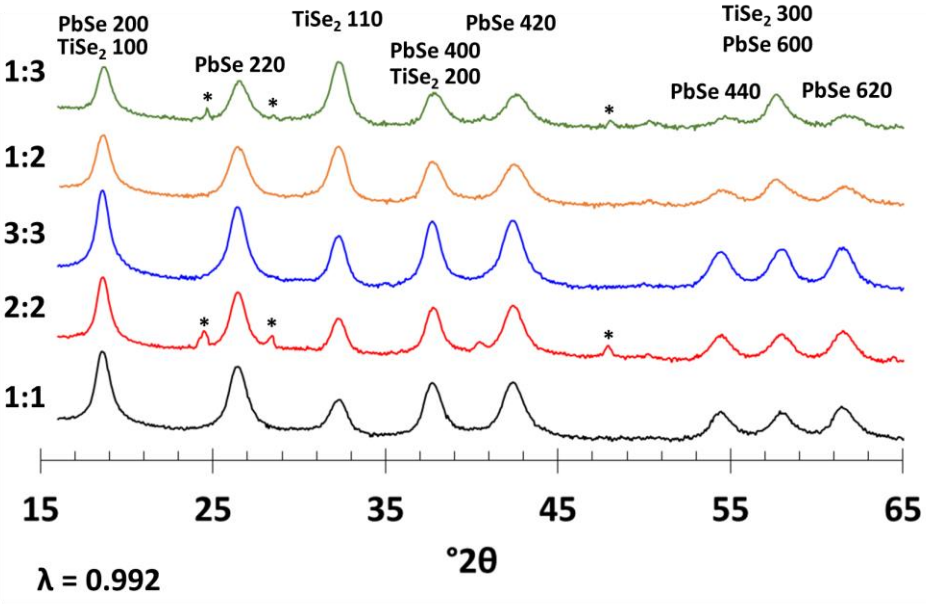

Figure VII.4. In-plane X-ray diffraction data. * marks peaks from the aluminum stage.

Table VII.2. Lattice parameters and misfit determined from in-plane XRD.

m:n	*a* (PbSe)	*a* ($TiSe_2$)	1+δ
1:1	6.137(1)	3.57(1)	1.17
1:2	6.118(3)	3.562(5)	1.17
1:3	6.109(4)	3.561(6)	1.18
2:2	6.134(3)	3.57(1)	1.17
3:3	6.140(1)	3.57(1)	1.17

The temperature dependent resistivity data for the 1 : n series of samples from Set A are shown in Figure VII.5. The resistivity of all three samples are close in magnitude and are representative in having a very small temperature dependence relative to the one known crystalline PbSe-$TiSe_2$ misfit layer compound. The resistivity slowly decreases as temperature is lowered from room temperature, likely due to a decrease in carrier scattering due to atomic vibration and in-plane phonons. At the lowest temperatures measured there is a slight upturn in the resistivity that has been attributed to electron-electron correlations.[9] The room temperature resistivity values for the remaining 6 samples are tabulated in Table VII.3. From the room temperature resistivity values, there is no apparent correlation between the resistivity and number of $TiSe_2$ or PbSe repeats per unit cell. Room temperature resistivity values were also measured for most of Set B and are included in Table VII.3. Temperature dependent resistivity data was also collected for the 1-n series for Set C. These results are plotted with Set A in Figure VII.5. Set C behavior is very similar to Set A, however each sample has a slightly smaller resistivity than it's counterpart in set A and the slight upturn at low temperatures is diminished.

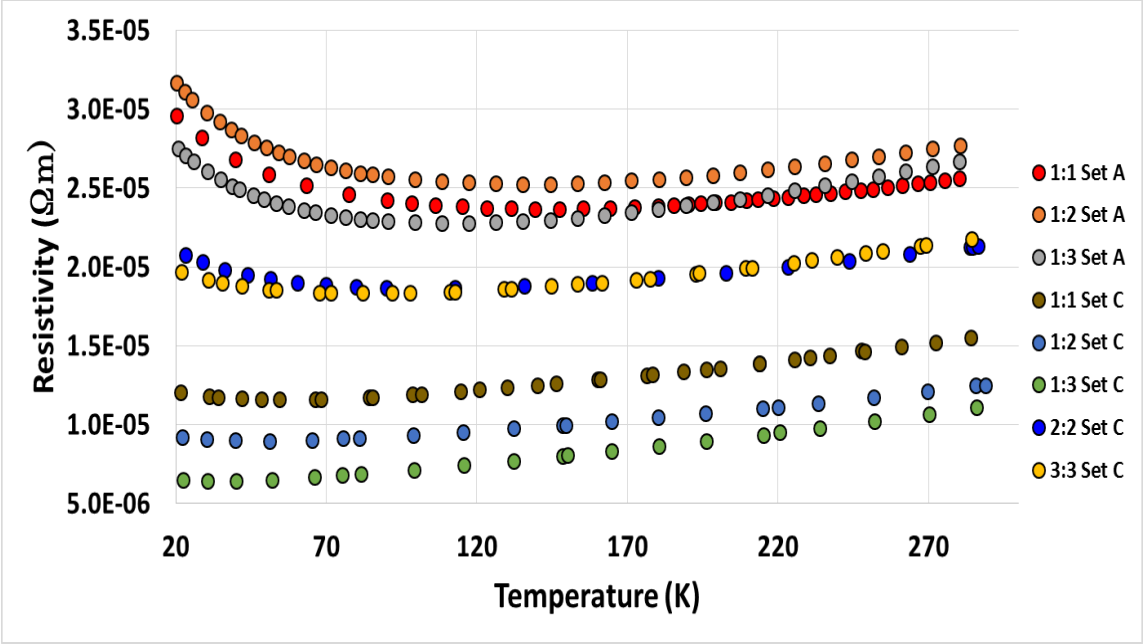

Figure VII.5. Temperature dependence of the resistivity.

The Seebeck coefficient was measured for all 9 samples of set A. The Seebeck coefficient increases as the number of $TiSe_2$ layers is increased as shown in Fig VII.6.a. Plotting the same data vs. the PbSe repeats (Fig VII.6.b) shows that the Seebeck is independent of the number of PbSe repeats in a unit cell. Seebeck coefficients for Set B samples are plotted versus the number of $TiSe_2$ and PbSe layers, along with the data from samples in Set A, in figures VII.6.c and d. The absolute value of the Seebeck coefficient for each sample changes between sets, however the trends within a sample set is consistent. This is consistent with the findings of Chapter V, which shows that variation between deposition cycles is larger than the variation within a deposition cycle. This study shows that in order to investigate trending as a function of changing structure, samples from the same sample set should be used.

Table VII.3. Room temperature resistivity

Sample Set	m	n	Resistivity (Ωm)
A	1	1	2.7E-05
	1	2	3.7E-05
	1	3	4.3E-04
	2	1	5.2E-05
	2	2	3.9E-05
	2	3	2.9E-05
	3	1	1.5E-04
	3	2	4.5E-05
	3	3	4.3E-05
B	1	1	1.5E-05
	1	2	1.7E-05
	2	1	1.6E-04
	2	2	3.3E-05
	3	1	8.6E-05
	3	2	3.0E-05
	3	3	2.4E-05
C	1	1	1.6E-05
	1	2	1.3E-05
	1	3	1.1E-05
	3	3	2.2E-05
	2	2	2.1E-05

With no apparent correlation between Seebeck coefficient and resistivity, sample set C was synthesized to determine Hall coefficients, which were used to calculate carrier concentration and mobility assuming a single band model. These results are in Table VII.4 and the mobility is plotted against the number of $TiSe_2$ layers in Figure VII.7.

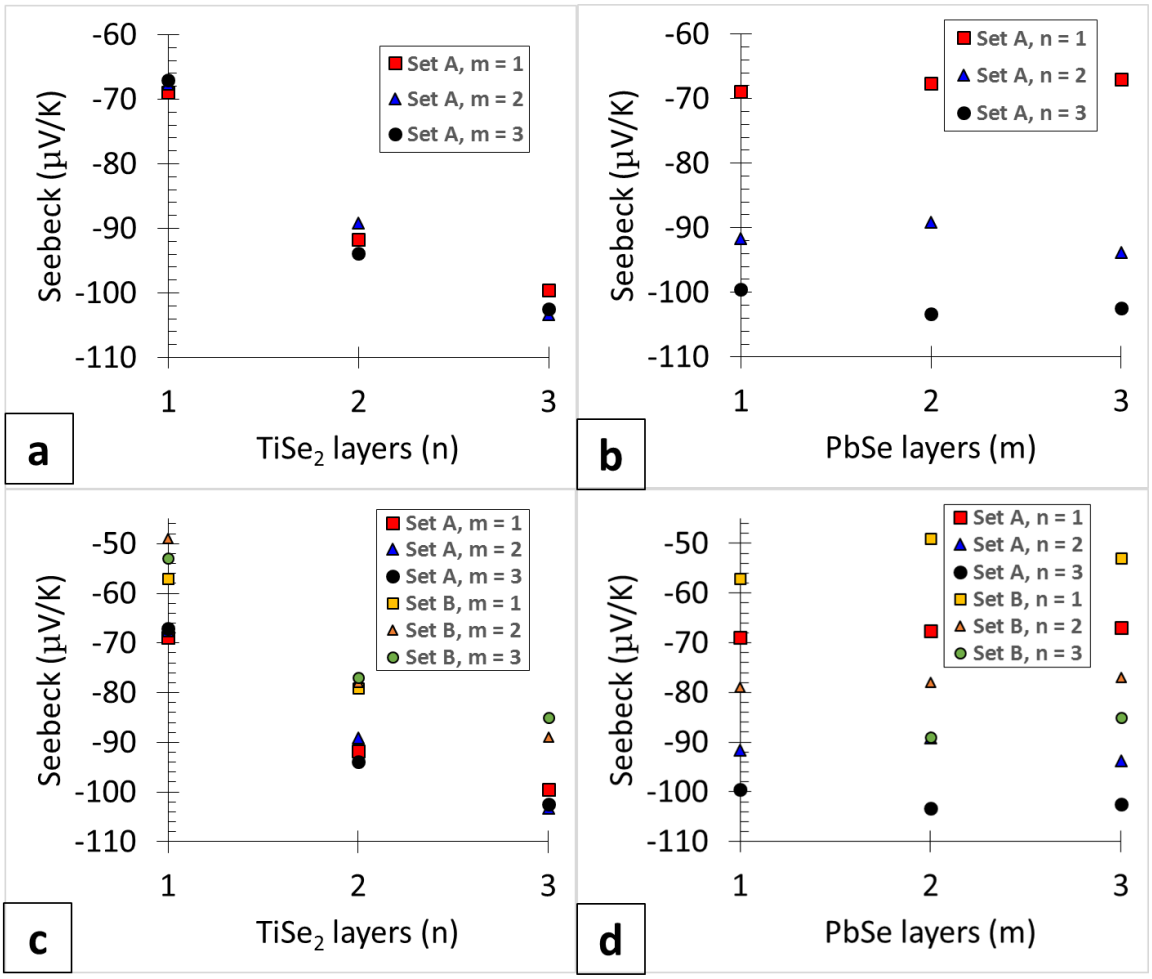

Figure VII.6. Room temperature Seebeck coefficients.

Table VII.4. Calculated carrier concentrations and mobility values for Set C

		Carrier	Mobility
m	n	Concentration	µ (cm^2/Vs)
1	1	2.3E+21	1.7
1	2	1.9E+21	2.6
1	3	1.6E+21	3.5
2	2	1.9E+21	1.5
3	3	1.5E+21	2.0

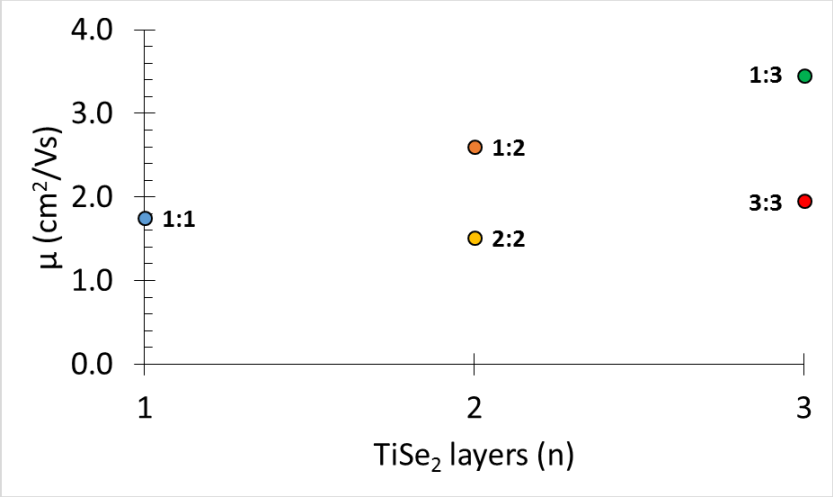

Figure VII.7. Mobility plotted against the number of $TiSe_2$ layers/unit cell for Set C.

Compounds with m = n have similar mobility values, while increasing the number of $TiSe_2$ layers relative to PbSe layers seems yields higher mobility values. This behavior supports charge transfer between the layers, as previously reported for ferecrystals.[10] As the mobility improves with increased $TiSe_2$, the carrier concentration decreases, leading to the increased Seebeck coefficients as a function of n.

VII.3. Conclusion

The first nine compounds in the $[(PbSe)_{1+\delta}]_m(TiSe_2)_n$ series of compounds were successfully synthesized from elemental precursors. The optimal annealing conditions do not depend on the layering scheme. The constituent structures appear to vary little from the bulk structures in the in-plane direction. While the variation between sample sets makes the identification of trends difficult, it is clear that increasing the ratio of n : m results in increases in the Seebeck coefficient, suggesting that compounds with high n values may be interesting for thermoelectric applications.

CHAPTER VIII

INVESTIGATING ELECTRICAL PROPERTIES OF THE $([PbSe]_{1+\delta})_1(TiSe_2)_n$ FAMILY OF FERECRYSTALS (n = 1 - 18)

VIII.1. Introduction

Thermoelectric materials, while being an appealing avenue to address today's energy crisis, have yet to become efficient and cheap enough to find their way into most applications.[1] The challenge in designing better thermoelectrics lies in the seemingly contradictory properties the material needs to possess.[2] The material must be a good electronic conductor and have a high Seebeck coefficient, but be a very poor thermal conductor, all of which have different carrier concentration dependencies. Currently, bulk alloys of Bi_2Te_3 and Sb_2Te_3 are the materials used most in real world applications,[3] however research has intensified around designing nanostructured materials because this approach has been shown to decrease lattice thermal conductivity while maintaining high electrical conductivity and high Seebeck coefficients.

Turbostratically disordered $[(PbSe)_m(MoSe_2)_n]$ misfit layer compounds have remarkably low lattice thermal conductivity, ~0.07 $Wm^{-1}K^{-1}$,[4] over 10 times lower than $Bi_{0.5}Sb_{1.5}Te_3$ (1 $Wm^{-1}K^{-1}$),[5] but their electrical conductivity is too low to be useful as a thermoelectric material. Other turbostratically disordered misfit layered compounds (or ferecrystals) have been reported to have much higher electrical conductivity, for example $([PbSe]_{1+y})_m(TiSe_2)_n$, but should have similarly small lattice thermal conductivities. Optimizing the power factor, the electrical conductivity times the square of the Seebeck coefficient could potentially lead to useful thermoelectric materials.

The synthesis route known as the modulated elemental reactants (MER) method, allows for a practically unlimited number of compounds that can be synthesized in the $([PbSe]_{1+y})_m(TiSe_2)_n$ family of ferecrystals. In the previous chapter, nine of these compounds in the $([PbSe]_{1+y})_m(TiSe_2)_n$ family were described, with m and n values 1-3. These compounds were metallic, with very similar resistivity values. However the Seebeck coefficient increased with the number of $TiSe_2$ layers per unit cell (n) while the number of carries decreased as the charge transferred from PbSe was diluted over more layers. To investigate if this trend in the Seebeck coefficient continues to higher n values, yielding compounds with high enough power factors to be interesting as thermoelectric materials, compounds in this family with a single PbSe bilayer and n values up to 18 were synthesized. While we find the power factor does indeed trend to a higher value as we increase n, further optimizing of the carrier concentration and an increase in the carrier mobility will be required to obtain a ZT greater than one.

VIII.2. Results and Discussion

Sample synthesis is described in detail in Chapter II. There were five sets of samples made for this study, made at different times but otherwise similar experimental parameters. Variation in samples is expected as shown in Chapter V. The five sets of samples will be referred to as Sets A-E in the discussion.

Representative out-of-plane diffraction patterns for a variety of samples used in this study are shown in Figure VIII.1. Each peak can be indexed as an (00*l*) reflection of the superlattice for the $([PbSe]_{1+y})_1(TiSe_2)_n$ compound. The n value and several (00*l*)

indices for each scan are shown above the diffraction patterns and the *c*-axis lattice parameter is contained in Table VIII.1. Plotting the *c*-axis lattice parameter versus the number of $TiSe_2$ trilayers (Figure VIII.2) yields a slope of 0.6034 nm, which corresponds to the thickness of each additional $TiSe_2$ trilayer. This is in good agreement with the bulk value of 0.6002 nm.[6] The intercept of this plot, 0.613nm, corresponds to the thickness of the single PbSe bilayer in each compound. This also is in good agreement with the bulk PbSe value reported at 0.6128nm.[7]

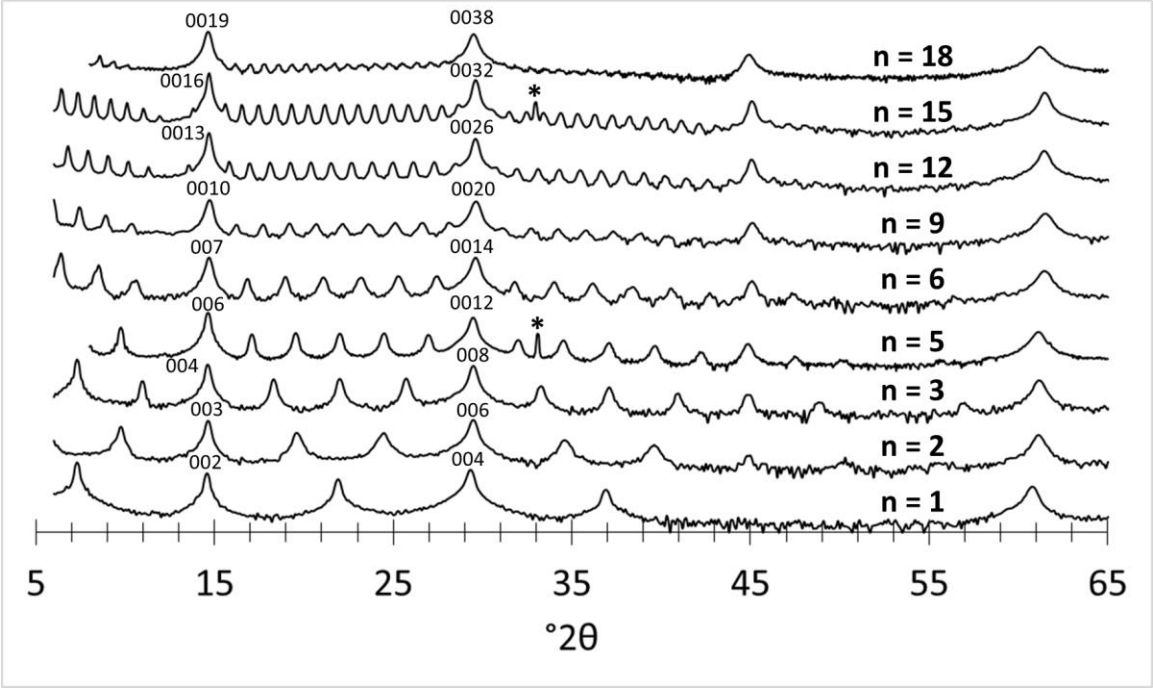

Figure VIII.1. Stacked diffraction patterns of a variety of the $([PbSe]_{1+y})_m(TiSe_2)_n$ samples used in this study, the n value is giving above each pattern. * denotes diffraction peaks originating from the Si substrate.

Table VIII.1. *c*-lattice parameters for all samples in this study.

Sample Set	$TiSe_2$ layers (n)	*c*-lattice parameter (Angstroms)
Set A	1	12.183(5)
	2	18.22(5)
	3	24.29(5)
Set B	1	12.18(1)
	2	18.17(1)
	9	60.26(1)
	12	78.21(1)
	15	96.55(3)
Set C	1	12.18(1)
	2	18.17(4)
	3	24.18(1)
	4	30.2(2)
	6	42.21(5)
Set D	5	36.38(3)
	6	42.43(7)
	9	60.67(7)
Set E	15	96.7(3)
	18	114.9(2)

STEM images were acquired for one of the samples, $([PbSe]_{1+y})_1(TiSe_2)_{12}$, to further investigate the structure of this family of compounds. A representative image is shown in Figure VIII.3. Turbostratic disorder is evident between the separated layers of $TiSe_2$ and PbSe. This rotation disorder is indicated by the different zone axes (or crystal faces) seen in different layers and the lack of any pattern between them. The 12 $TiSe_2$ layers within one unit cell of the superlattice structure adopt the 1-T polytype structure,

as has been reported for $TiSe_2$ itself prepared using MER approach.[8] This is different than the rotationally disordered arrangement of layers observed in ferecrystals containing the group V and VI dichalcogenides, which have stacking sequences such as the 2-H polytype observed for $TaSe_2$.[8]

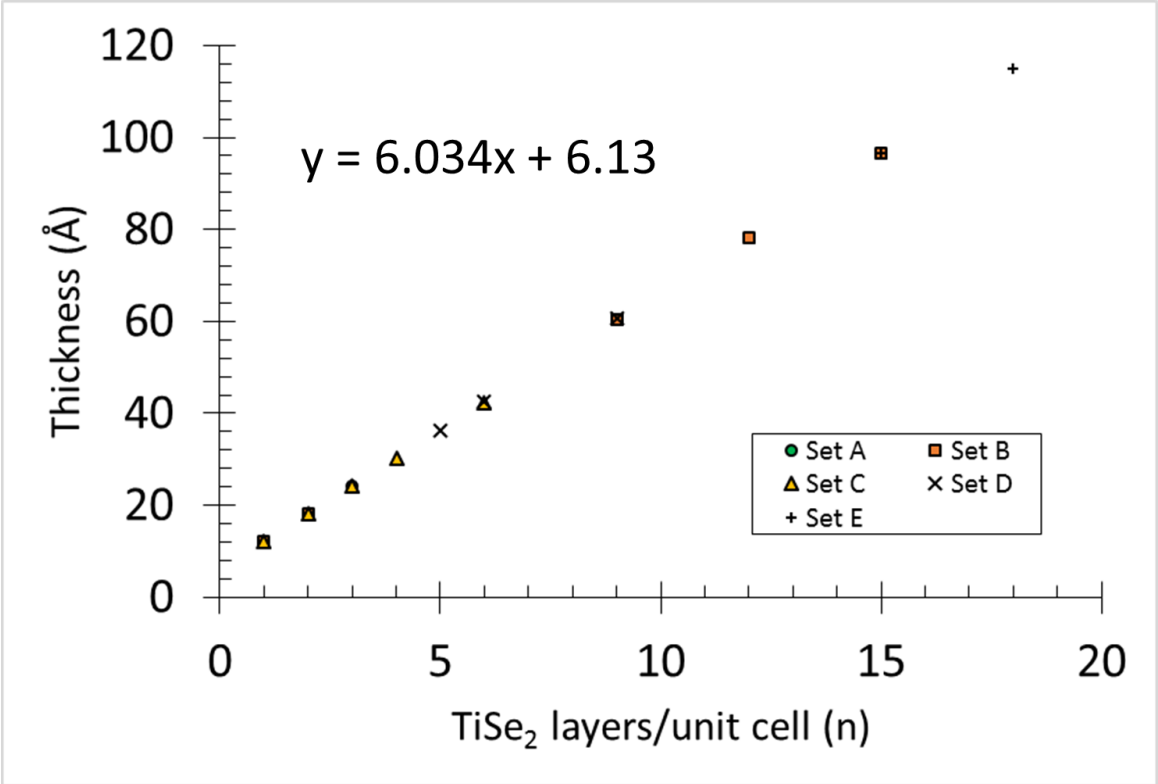

Figure VIII.2. Plotting unit cell thickness vs. the number of $TiSe_2$ layers per unit cell gives a slope equal to the thickness of 1 layer of $TiSe_2$ while the intercept is equal to the thickness of the PbSe layer.

The room temperature electrical resistivity was measured for a majority of the samples in this study and the data is shown in Figure VIII.4. The magnitude of the resistivity is in the lower end of the metallic regime, on the order of 10^{-5} Ωm, and the spread of resistivity values for all samples is about a factor of four. Samples of the same compound made in different deposition cycles vary by as much as a factor of three. This

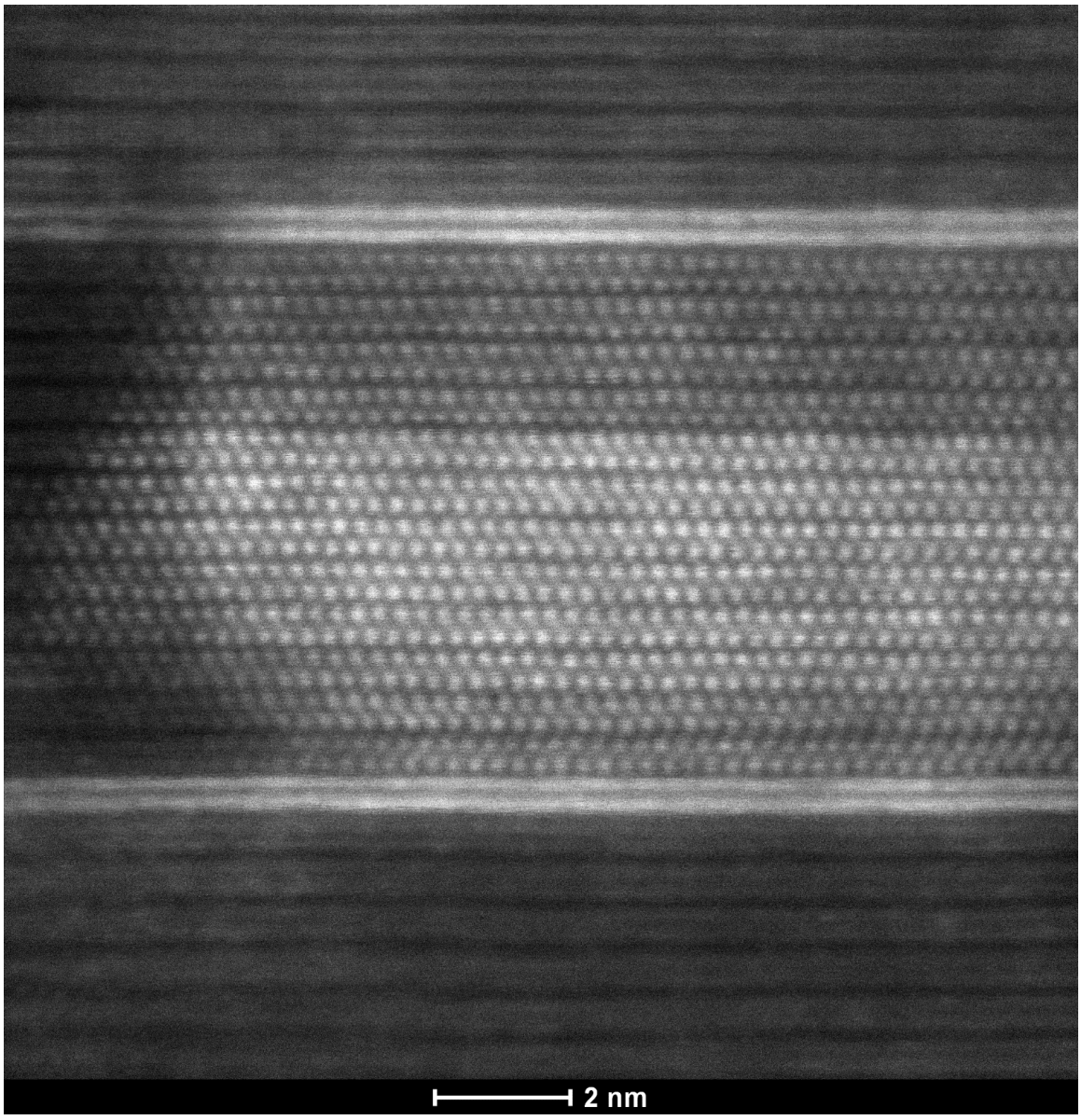

Figure VIII.3. STEM image of the $([PbSe]_{1+y})_1(TiSe_2)_{12}$ compound.

variation prevents making a clear connection between the number of $TiSe_2$ layers and the resistivity. MER synthesized $TiSe_2$[9] , the n = ∞ member of this series, has a resistance of 3.58 x 10^{-5} Ωm at room temperature.

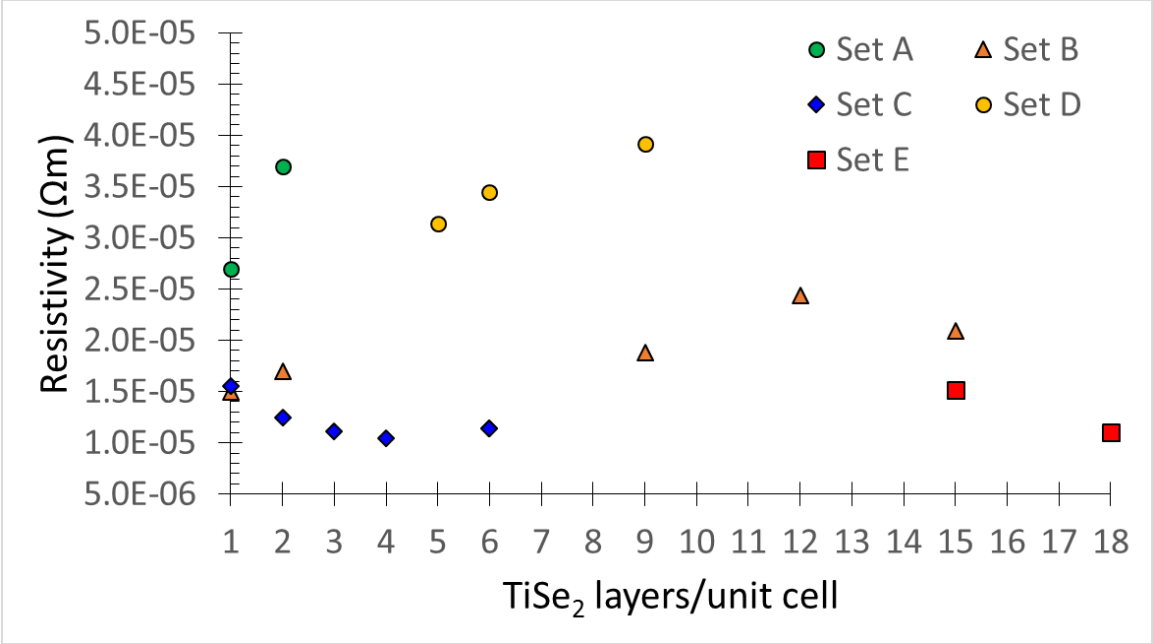

Figure VIII.4. Room temperature resistivity data for most of the samples included in this study.

Temperature dependent resistivity data was also collected for several samples and is shown in Figure VIII.5. All samples measured showed very little temperature dependence, with the largest change being a factor of 1.25 over the temperature range measured. In comparison, the change in resistivity over the same range is 12 times greater for the $([PbSe]_{1.16})_1(TiSe_2)_2$ misfit layer compound reported by Giang et al.[10] The small resistivity ratios (ρRT/ ρ20K) are, interestingly, not due to an increase in the low temperature resistivity, but rather a lack of increase in resistivity as a function of temperature normally observed for three dimensional crystals. This has been attributed to the turbostratic disorder present in the films, which disrupts phonons with any *c*-direction component. This decreases the number of electron-phonon scattering events as the temperature increases. There is an increased resistivity at very low temperatures

in most of the samples studied and the temperature where this upturn begins and the magnitude of the upturn both increase as the resistivity of the sample increases. It has been speculated that electron localization from electron-electron correlations could be responsible for this behavior, which has been reported for other layered intergrowths containing rotationally disordered $TiSe_2$.[11]

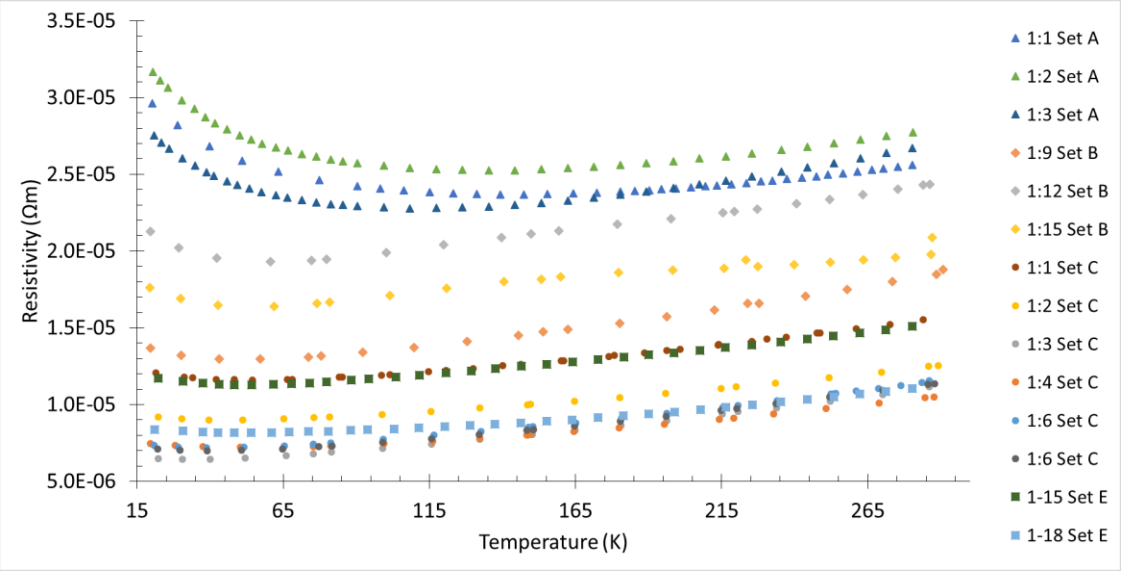

Figure VIII.5. Temperature dependent resistivity data.

The room temperature Seebeck coefficient for the samples in this study are shown in Figure VIII.6 plotted against the number of $TiSe_2$ layers. In general there is an increase in the magnitude of the Seebeck coefficient trend continues with increasing n, but different sample sets have significantly different Seebeck coefficients for the same compound. For n values greater than 9, the Seebeck coefficient remained constant at about -110 μVK^{-1}. The MER synthesized TiSe2 ($n = \infty$) has a Seebeck coefficient of -134 $\mu V/K$,[9] slightly higher than measured for the compounds in this study with large n.

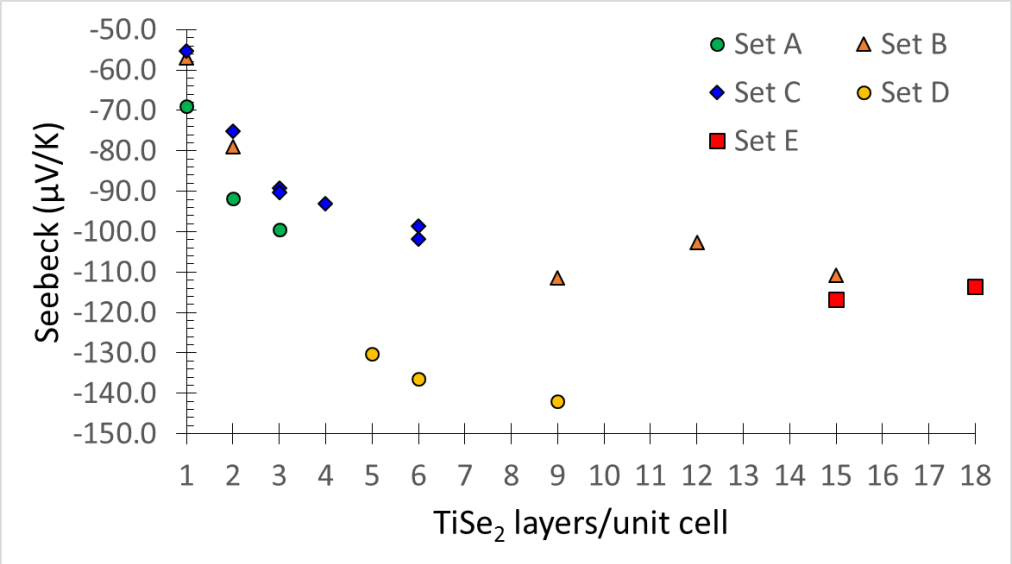

Figure VIII.6. Room temperature Seebeck coefficients.

The thermoelectric power factor (σS^2) is shown plotted as a function of the $TiSe_2$ (n) layers in Figure VIII.7. Since the resistivity remains fairly constant within the family of compounds, the general trend in increased Seebeck as a function of n carries over to an increase power factor. The thermoelectric industry standard material, Bi_2Te_3, has an optimized room temperature power factor of around 45 $mWcm^{-1}k^{-2}$.[12] The highest measured ferecrystal in this study is the n = 18 compound with a power factor of around 11 $mWcm^{-1}k^{-2}$., in a very reasonable range for a material that could be optimized as a useful thermoelectric material. To begin to understand how to optimize this family of compounds electrical behavior and drive up the thermoelectric power factor, more information is needed about the carrier behavior.

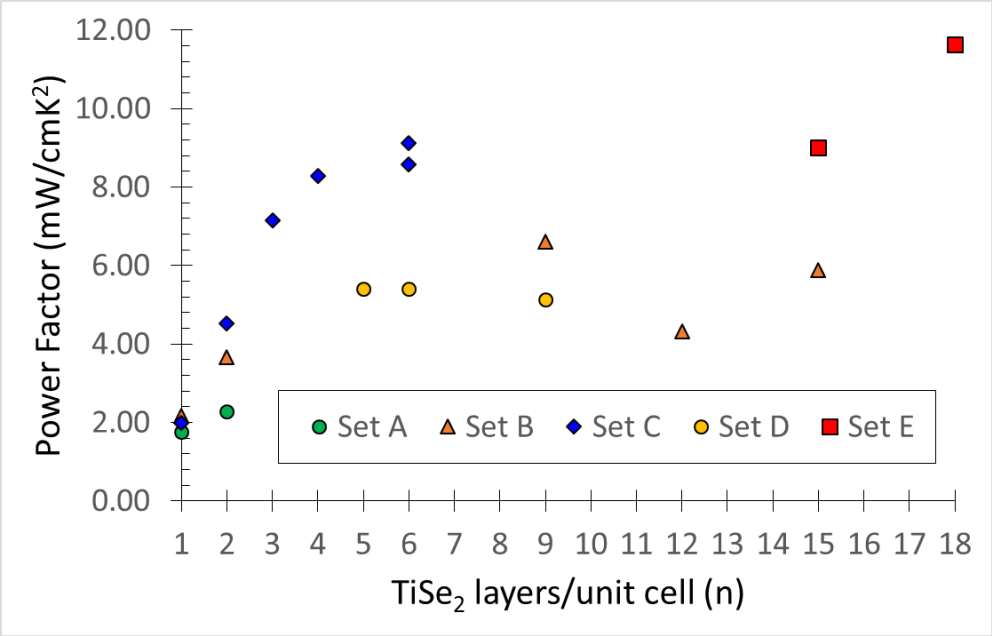

Figure VIII.7. Calculated power factors

In order to gain more insight on the transport properties of this system, Hall measurements were performed on various samples and the room temperature carrier concentrations calculated from the Hall coefficients assuming a single band model are plotted in Figure VIII.8. In general, the carrier concentration decreases as n increases, consistent with the current hypothesis in the TiX_2 misfit layer compound literature suggesting that the rocksalt layer donates electrons to nominally unoccupied Ti 3d stated in the TiX_2 layers. In such a case, PbSe should act as an electron donor, and $TiSe_2$ as an electron acceptor. As n increases, the number of total carriers donated should increase until the chemical potential or Fermi level in the two constituents is equal. Saturation behavior would be expected as the ratio of electrons available for donation in the PbSe layer to the number of available Ti 3d states is decrease. The data supports this trend generally, though the sample-to-sample variation prevents the clear

observation of any saturation behavior. It should also be noted that in the case of n > 1, excess atoms (especially Ti) could be house in the van der Waal's gaps between $TiSe_2$ layers, further complicating any charge transfer behavior.[9]

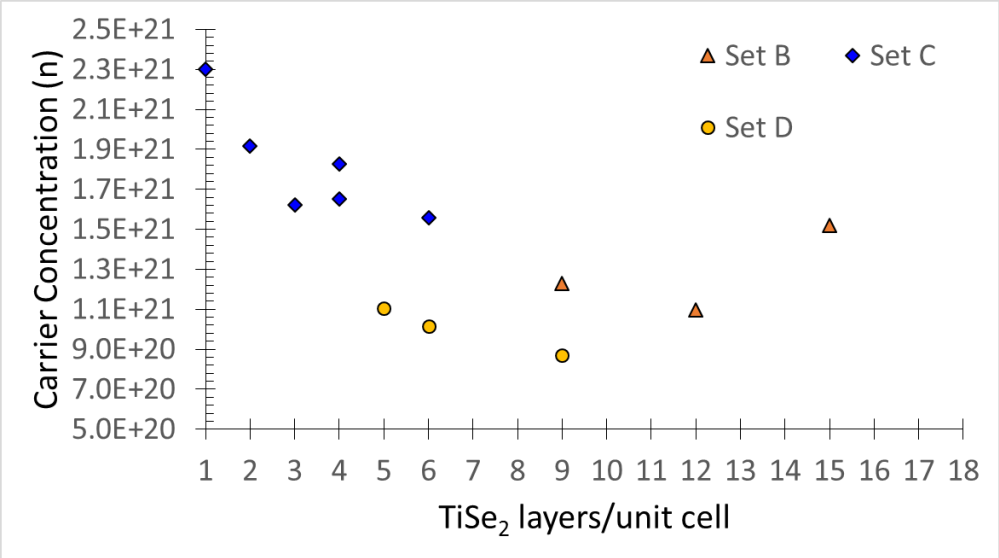

Figure VIII.8. Carrier concentrations.

The mobility of samples from Sets B, C, and D were calculated and these are shown in Figure VIII.9 as a function of $TiSe_2$ (n) layers. Variation in mobility as a function of n is small as variation between the same compound made multiple times is on the same order. Set C taken by itself has a general trend of increasing mobility as n is increased, however this trend disappears when the data is combined with Set B and D. Set B and D, rather, have fairly constant mobilities between 1.75 and 2.75 $cm^2V^{-1}s^{-1}$.

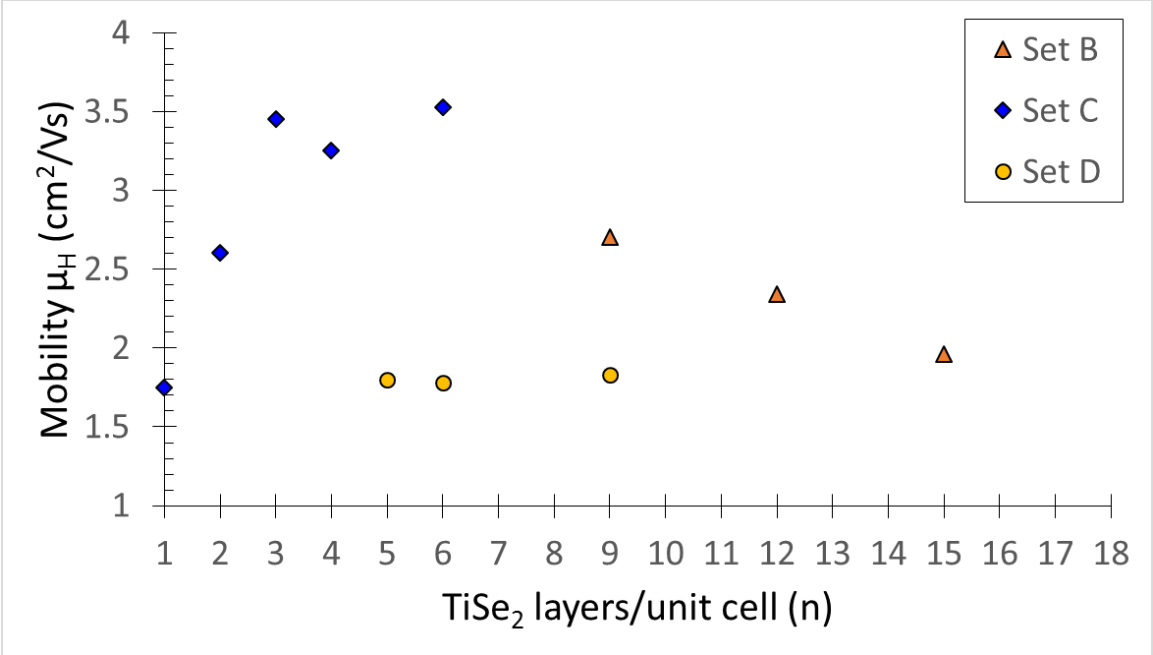

Figure VIII.9. Calculated mobility.

Though the variation of samples makes it difficult to draw clear conclusions on the behavior of the $[(PbSe)_{1+\delta}]_m(TiSe_2)_n$ as a function of n, further insight into the materials' behavior can be gained by plotting the Seebeck coefficient as a function of carrier concentration (Figure VIII.10). In general, the Seebeck coefficient is expected to depend on the carrier concentration based on the relationship given below, where α is the Seebeck coefficient, n is the carrier concentration, e is the elementary charge, h is Planck's constant, k_B is Boltzmann's constant, m^* is the effective mass, and T is temperature[13]

$$\alpha = \frac{8\pi^2 {k_B}^2}{3eh^2} m^* T \left(\frac{\pi}{3n}\right)^{2/3}$$

While the data shows a clear increase in magnitude of α with a decrease in carrier concentration as expected from the given relationship, the trend does not follow a clear $n^{-2/3}$ dependence. The variation between samples and the expected changes to the local environments and subsequent subtle changes to band structure as the number of $TiSe_2$ layers per unit cell increases would suggest that the effective mass of electrons in the material should not be constant. In this context, the convoluted dependence of the Seebeck coefficient on carrier concentration is not surprising. The data clearly suggests that controlling carrier concentration by means beyond just varying n is crucial to the optimization of the materials for thermoelectric applications.

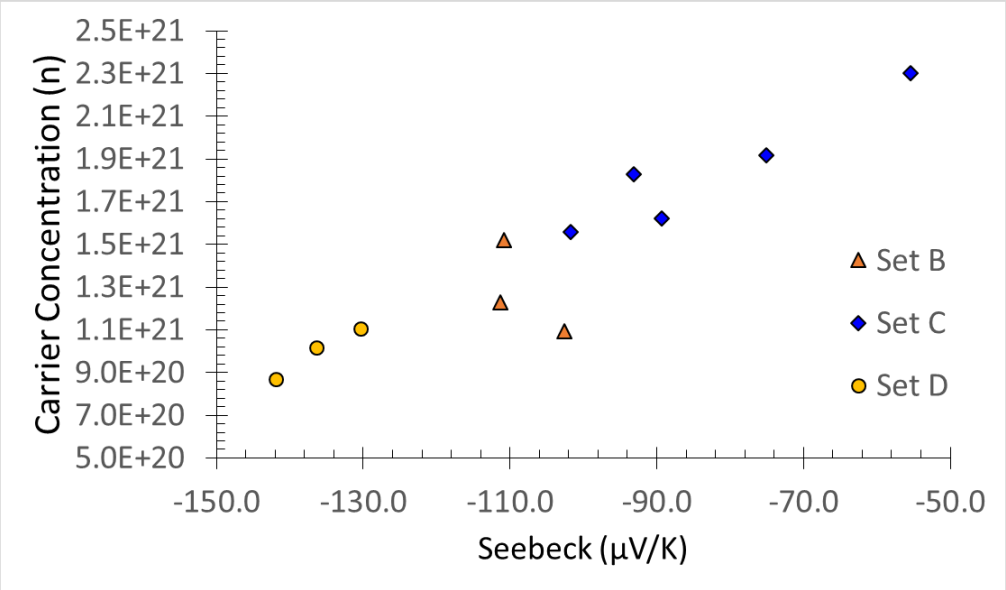

Figure VIII.10. Room temperature carrier concentrations plotted against Seebeck coefficient.

VIII.3. Conclusion

Compounds in the $[(PbSe)_{1+\delta}]_1(TiSe_2)_n$ series are reported, up to n = 18. The variation of n is expected to result in a decrease in carrier concentration according to the current hypothesis found in literature. While acknowledging that sample-to-sample

variation convolutes the conclusions that can be drawn from the data, the hypothesis seems to be supported by the data. Not surprisingly, increasing n generally leads to a decrease in the number of electrons per unit volume as the ration of donors to acceptors is decreased. Plotting the Seebeck coefficient versus carrier concentration further confirms the need to realize a consistent manner of decreasing the number of carriers in the material to make them viable thermoelectric materials.

VIII.4. Bridge

Designed synthesis of the $[(PbSe)_{1+\delta}]_m(TiSe_2)_n$ family of compounds has been realized over the last several chapters. In order to examine how robust the MER synthesis method is, a new family of compounds was chosen, $[(PbTe)_{1+\delta}]_m(TiTe_2)_n$. Telluride misfit layer compounds have never been reported before, which makes these compounds an excellent candidate to further evaluate the MER synthesis method.

CHAPTER IX

TELLURIDE MISFIT LAYER COMPOUNDS: $[(PbTe)_{1.17}]_m(TiTe_2)_n$

This work was published in volume 53 of Angewandte Chemie International Edition in 2014 with co-authors Matt Beekman, Sabrina Disch, and David C. Johnson. Matt Beekman provided assistance with electrical data analysis, Sabrina Disch provided the Rietveld and le Bail analysis, David C. Johnson is my advisor and research group leader, and I am the primary author.

IX.1. Introduction and Discussion

1990, DiSalvo highlighted how the concepts and basic principles that are the core of synthetic molecular chemistry had yet to be developed and applied towards the synthesis of new extended solids.[1] These principles include the ability to predict composition (stoichiometry) and structure (the geometric arrangement of atoms), and reaction mechanism (an understanding of how reactants evolve into products). The relative lack of predictive power and detailed control of reaction mechanisms in synthetic solid state chemistry has historically limited the number of ternary and higher order compounds that have been prepared. Stein[2] and co-authors attributed this to the diffusion limited, high temperature reactions traditionally used to prepare new solid state compounds, which yield the most thermodynamically stable products under the reaction conditions. To overcome slow solid-state diffusion rates, several synthesis approaches start with amorphous precursors and use composition as the experimental tool to direct nucleation, however nucleating desired products is not controlled.[3–6]

Stein and co-authors also suggested that a key factor enabling the rational prediction of composition and structure of products would be the retention of structural elements of starting materials in the products, which would require significantly reduced reaction temperatures.

Recently we have shown that it is possible to prepare entire families of structurally related metastable compounds with designed compositions and structures, based on an existing, thermodynamically stable prototype intergrowth of two different structural motifs[7]. Vacuum deposition techniques are used to produce a layered precursor of alternating elemental constituents. By tuning the relative thickness of these individual elemental layers, local composition can be systematically controlled. The local composition(s) in the precursor controls the identity of the structure(s) that nucleate. The presumably random nucleation events result in an unusual rotational disorder between layers known as turbostratic disorder[8]. The nanoarchitecture of the precursor remains intact during the low temperature self-assembly of products and the essential structural framework of the products can be predicted based on the bonding motifs found in the binary compounds. To explore how general this approach might be, we attempted to use this synthesis approach to prepare a previously unknown family of compounds, $[(PbTe)_{1+\delta}]_m(TiTe_2)_n$, where δ represents the difference of in-plane packing density of the two constituents, structurally related to the so called misfit layer compounds as described by the general formula $[(MX)_{1+\delta}]_m(TX_2)_n$. To our knowledge, there are no known tellurides with this structure type, although the constituent binary compounds PbTe and $TiTe_2$ exist with structures similar to those found in misfit layer compounds.

Briefly, an initial series of 5 precursors was made with m:n values targeted at m:n = 1:1, 1:3, 1:5, 5:1, and 3:1 by depositing a Pb-Te bilayer m times and a Ti-Te bilayer n times assuming that δ was the same as for the known selenide compound.[9]. Based on composition and thickness of these initial samples, the deposition parameters were iteratively adjusted to obtain the desired composition of each layer and to scale the individual layers to the correct thickness. The diffraction patterns of the optimized as-deposited samples suggested that some self-assembly occurs during the deposition process and time spent at room temperature. An annealing study via X-ray diffraction is shown in Figure IX.1. The precursor used in this study was designed to form the $[(PbTe)_{1.17}]_3(TiTe_2)_1$ compound upon annealing. After annealing for 30 seconds at 200°C, all expected 00*l* diffraction peaks in this scan range are visible and more intense. One minute of annealing at 200°C slightly increased the diffraction intensities, but increasing the annealing temperature to 300°C decomposed the desired product. This low decomposition temperature explains why this compound has not been previously observed.

Additional optimized precursors targeting m:n = 1:1, 1:2, 3:1, and 5:1 were annealed for one minute at 200°C and the diffraction patterns of successfully synthesized $[(PbTe)_{1.17}]_m(TiTe_2)_n$ compounds are shown in Figure IX.2. The diffraction patterns all contain only the 00*l* diffraction peaks for the targeted compounds, indicating that the samples are highly textured. The *c*-axis lattice parameters change by 6.47Å for each additional PbTe structural unit added to the structure and by 6.73Å between the 1:1 and

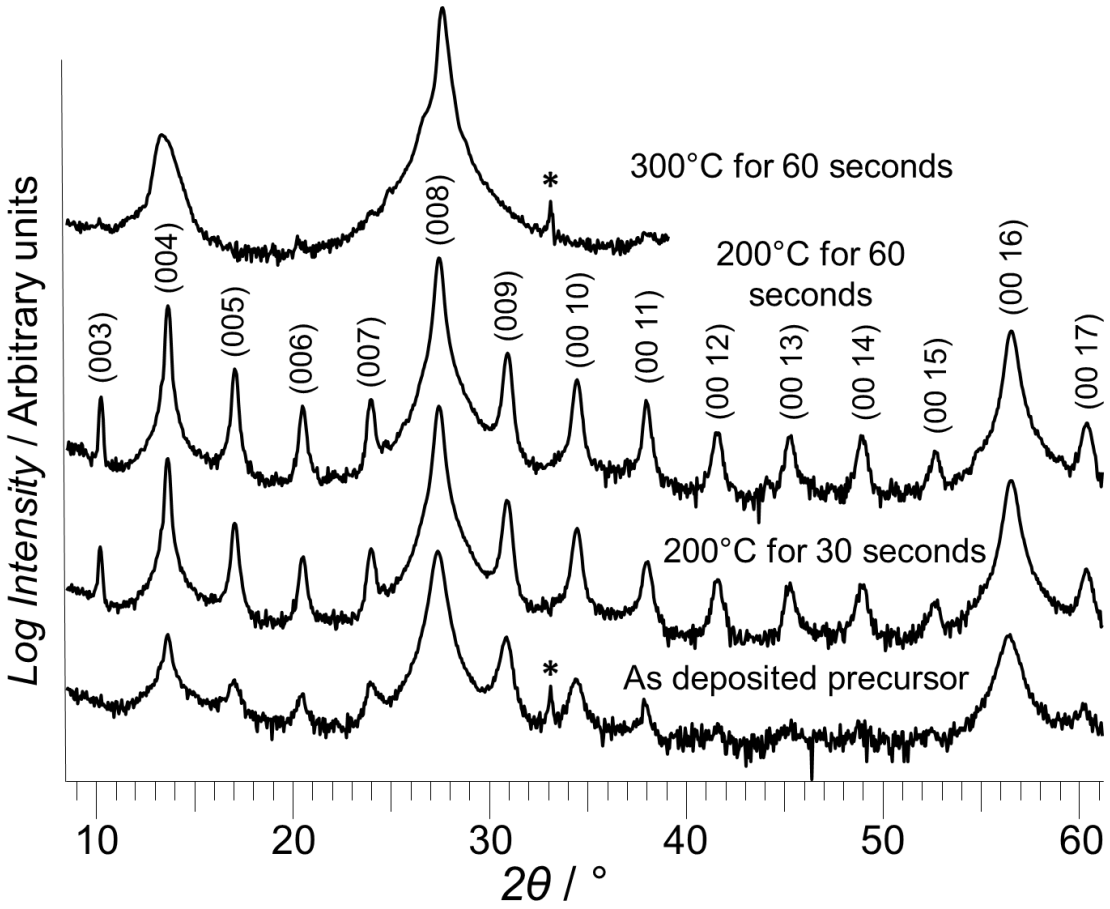

Figure IX.1. Specular X-ray diffraction patterns collected post annealing of the precursor designed to form the compound $[(PbTe)_{1+\delta}]_3(TiTe_2)_1$. Indicated above each diffraction scan is the time the sample was annealed and the annealing temperature. The 00*l* indices are given above the pattern of 200°C for 60 seconds. The sharp reflection at around 33° marked with an * is from the Si substrate.

the 1:2 compounds, suggesting that this is the thickness of a $TiTe_2$ structural unit in the unit cell. The thickness of the corresponding structural units of the binary compounds of 6.454Å[10] for PbTe and 6.491Å[11] for $TiTe_2$ support this interpretation. The retention of the nanoarchitecture of the precursor as the products self-assemble enables the rational design of precursors for a specific product.

More detailed structural information was obtained through high resolution X-ray diffraction scans in the *hk*0 direction. Analysis of the *hk*0 reflection series according to the Le Bail approach for the $[(PbTe)_{1+\delta}]_3(TiTe_2)_1$ compound yields the in-plane lattice parameters of the binary constituents, PbTe with the tetragonal lattice constant a = 6.526(2) Å, and $TiTe_2$ with the hexagonal lattice constant a = 3.799(4) Å. The reflection positions corresponding to both PbTe and $TiTe_2$ do not change significantly as m and n are varied, whereas the relative scattering intensities change as expected as the m:n ratio is varied. These lattice parameters are close to those reported for the bulk PbTe (6.454 Å[10]) and $TiTe_2$ (3.777 Å[11]). From the determined in plane cell parameters, the misfit of the compound is derived as 0.174. This is close to the assumed value of 0.16 taken from the selenide compound that was used as the target for synthesis.

Analysis of the 00*l* reflection series of the $[(PbTe)_{1+\delta}]_3(TiTe_2)_1$ compound yields a lattice parameter of c = 26.044(1) Å and Rietveld refinement yields the position of atomic planes along this axis (Figure IX.3). The Ti-Te atomic plane distance of 1.66(1) Å is in good agreement with the bulk material (1.7 Å[11]). In contrast, the atomic plane distances in the PbTe layers deviate strongly from the bulk compound. Instead of a constant distance between (001) PbTe planes along the c axis, the 6 PbTe layers segregate into 3 PbTe double layers with a significantly larger distance between the double layers, as reported previously for $[(PbSe)_{1+\delta}]_m(TSe_2)_n$ where T is Mo and W.[12] The individual PbTe atomic layers furthermore distort with the Pb and Te moving in alternate directions, with the outermost Pb atoms approaching the neighbouring dichalcogenide layers. The distances between the Pb and Te atomic planes of 0.27(3) to 0.43(2) Å are in the range of puckering

distances previously observed for misfit layered compounds[13–16]. This effect is more pronounced close to the $TiTe_2$ layer and decreases toward the center of the PbTe stack, likely due to the finite thickness of the PbTe layers.

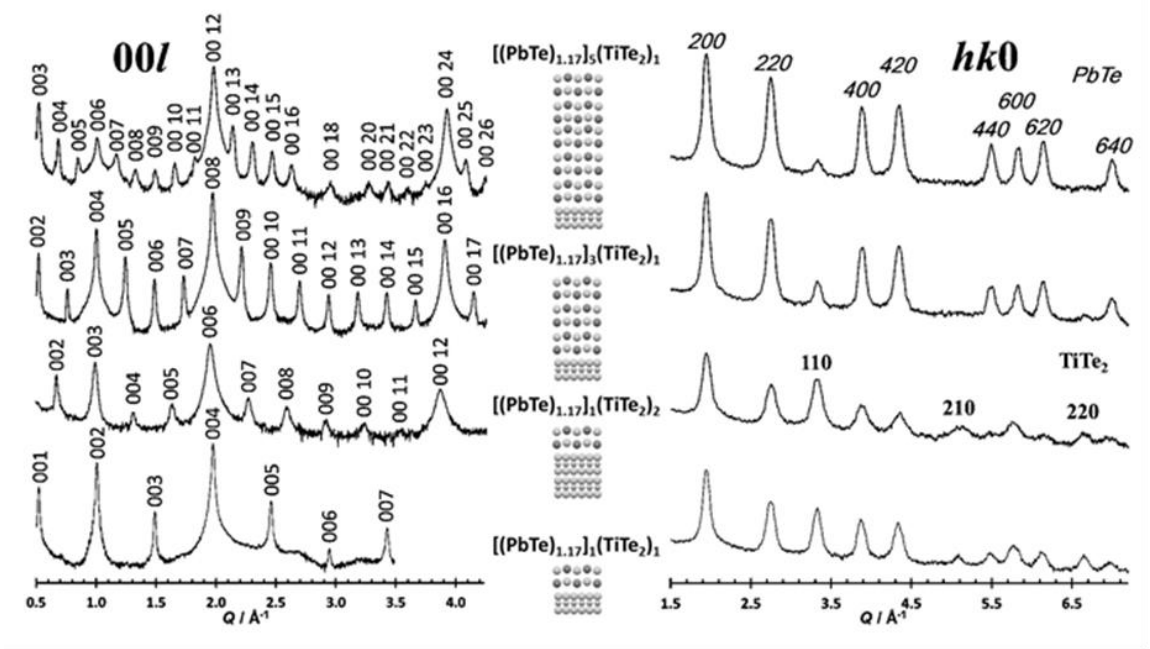

Figure IX.2. The out of plane diffraction patterns (left) and in plane diffraction patterns (right) containing the 00*l* and *hk*0 reflections respectively of some of the samples made in this study. Both sets of diffraction patterns are plotted in log scale and offset to separate the patterns. The numbers above the Bragg peaks are the Miller indices of the reflections. Schematic unit cells for each compound are in the center. For simplicity, these schematics do not show turbostratic disorder and are therefore only accurate for the c direction.

The TEM images in Figure IX.4 confirm the layered nature of the structure. There are six PbTe planes between the single Te-Ti-Te trilayers of $TiTe_2$. Each PbTe layer appears to have a single crystallographic orientation between $TiTe_2$ trilayers, and the crystallographic orientation of the PbTe and $TiTe_2$ layers change from layer to layer, confirming the turbostratic disorder indicated by our diffraction results.

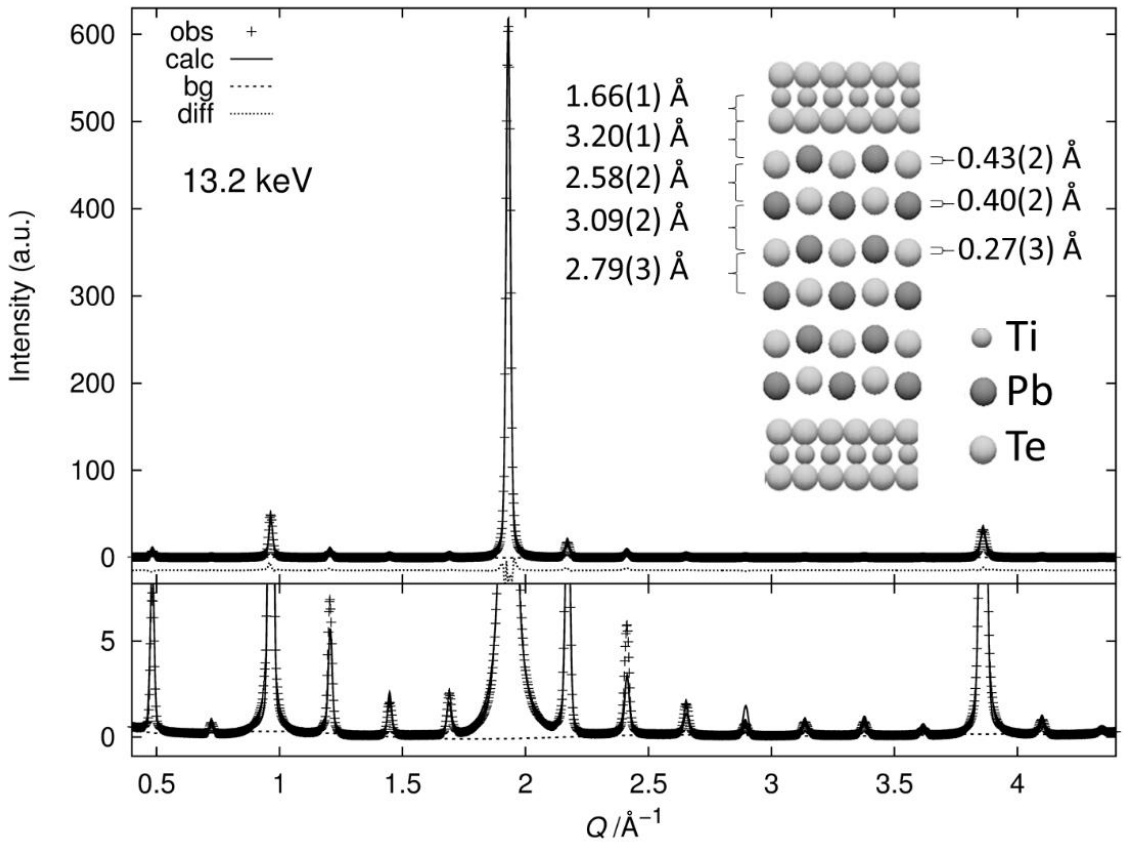

Figure IX.3. Results of the Rietveld refinement for the (00*l*) reflection series of $[(PbTe)_3]_{1.17}(TiTe_2)_1$ with observed, calculated, and difference intensities. The arrangement of the atomic planes in the *c* direction with atomic distances are shown in the inset.

The diffraction and TEM data support our ability to prepare targeted metastable compounds where the structure of the designed precursor is preserved in the final products. The structure of the PbTe layers is observed to distort, presumably as a consequence of competition between surface/interface and volume free energy contributions to the total free energy of the system. The low decomposition temperature explains why these compounds have not been previously observed. There are many other metastable compounds that probably cannot be accessed via high

temperature synthesis routes, and accessing them and their potential properties requires further development of the approach presented here and other low temperature synthesis approaches to extended solids.

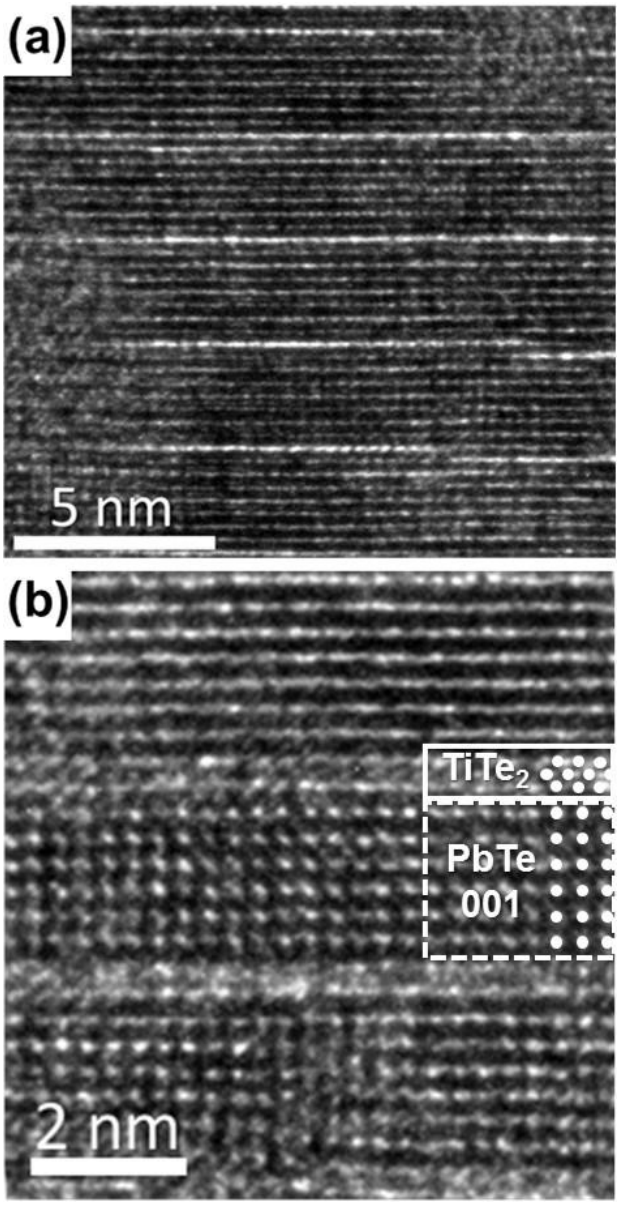

Figure IX.4. A representative TEM image of the $[(PbTe)_{1.17}]_3(TiTe_2)_1$ compound is shown (a) and a higher magnification image (b) contains a region with a [100] zone axis of PbTe.

IX.2. Experimental Details

Samples were synthesized using a custom built physical vapor deposition system.[9] High resolution X-ray diffraction using a point detector was measured at the 33-BM-C beamline of the APS. For the *hk*0 reflection series, an incident X-ray energy of 13.1 keV was selected, whereas for the 00*l* reflection series, X-ray energies of 12.5 keV and 13.2 keV (i.e. above and below the Pb L3 edge) were chosen. Refinements according to the Le Bail[17] and Rietveld[18] approaches have been carried out using the GSAS program package[19,20].

Cross-sections for the high-resolution transmission electron microscopy (HRTEM) investigations were prepared with an FEI Helios Nanolab D600. The in situ lift-out was done using an Omniprobe 200. HRTEM and electron diffraction studies were performed on an FEI aberration-corrected Titan 80-300 equipped with an objective lens C_s corrector.

CHAPTER X

CONCLUSIONS AND SUMMARY

$TiSe_2$ was synthesized using the modulated elemental reactant method. The thin film binary compound, in contrast to bulk, showed electrical behavior as a heavily doped semiconductor. This behavior is thought to be due to the MER compound containing excess Ti atoms incorporated into the van der Waal's gap by donating electrons to the conduction band of the material. A relatively large Seebeck coefficient for the measured carrier concentration was also observed for this compound. The first $TiSe_2$ turbostratically disordered misfit layer compound was synthesized by layering Pb and Se between the $TiSe_2$ units. The $[(PbSe)_{1.16}]_1(TiSe_2)_1$ compound was achieved after performing a careful calibration of the deposition system. The structural properties of this compound are investigated in detail and the electrical transport properties begin to be examined. The reproducibility in structure and electrical transport properties for the $([PbSe]_{1+y})_1(TiSe_2)_1$ compound was then investigated. Looking at the compound made several times, it is observed that variation can be large, but variation of samples synthesized in the same deposition cycle is much less. This information is critical in later studies to understand the variations measured.

Several other metastable compounds in the $[(PbSe)_{1+\delta}]_m(TiSe_2)_n$ family were synthesized, beginning with an in depth study of $(PbSe)_{1.18}(TiSe_2)_2$. This compound provided an excellent comparison to the only misfit layer compound in this elemental family synthesized using bulk techniques, and therefore not containing the rotational disorder seen in ferecrystalline compounds. When compared, the ferecrystal has

electrical properties that are significantly different than the misfit layer compound, including lower resistivity at room temperature and a two times higher Seebeck coefficient. The concept of designed synthesis was tested in more detail with the synthesis of nine members of the $[(PbSe)_{1+\delta}]_m(TiSe_2)_n$ family of ferecrystals (m,n = 1-3). The synthesis method developed earlier is used to successfully and repeatedly produce the nine compounds. The electrical transport properties indicate a strong correlation between increasing $TiSe_2$ layers and increasing magnitude of the Seebeck coefficient, while the resistivity remains relatively constant for all samples examined. This work also corroborates what is seen while investigating the sample variation of the $([PbSe]_{1+y})_1(TiSe_2)_1$ compound; that trending within a deposition cycle is evident but variation between cycles can be relatively large. The changes in electrical properties as n, or the number of $TiSe_2$ units, increases is further evaluated by synthesizing many more members of the $([PbSe]_{1+\delta})_1(TiSe_2)_n$ family of ferecrystals with m = 1 and n = 1-18. The electrical transport properties of these compounds reveal that increasing n generally leads to a decrease in the number of electrons per unit volume as the ratio of donors to acceptors is decreased. Examining the relationship between the Seebeck coefficient and the carrier concentration confirms the need to realize a consistent manner of decreasing the number of carriers in the material to make them viable thermoelectric materials.

Using the MER synthesis method as a tool for designing compounds is more rigorously tested by synthesizing the first telluride misfit layer compounds, $[(PbTe)_{1.17}]_m(TiTe_2)_n$. The robustness of the MER method is revealed by the synthesis of

these layered intergrowths which would not be possible using other synthesis methods available.

REFERENCES CITED

Chapter I

(1) Disalvo, F. J. *Science.* **1990**, *247*, 649–655.

(2) Stein, A.; Keller, S.; Mallouk, T. *Science.* **1993**, *259*, 1558–1564.

(3) Wiegers, G. A. *Prog. Solid State Chem.* **1996**, *24*, 1 – 139.

(4) Lin, Q.; Heideman, C. L.; Nguyen, N.; Zschack, P.; Chiritescu, C.; Cahill, D. G.; Johnson, D. C. *Eur. J. Inorg. Chem.* **2008**, 2382–2385.

(5) Heideman, C.; Nyugen, N.; Hanni, J.; Lin, Q.; Duncombe, S.; Johnson, D. C.; Zschack, P. *J. Solid State Chem.* **2008**, *181*, 1701–1706.

(6) Biscoe, J.; Warren, B. *J. Appl. Phys.* **1942**, *13*, 364.

(7) Chiritescu, C.; Cahill, D. G.; Heideman, C.; Lin, Q.; Mortensen, C.; Nguyen, N. T.; Johnson, D.; Rostek, R.; Böttner, H. *J. Appl. Phys.* **2008**, *104*, 033533.

(8) Lin, Q.; Smeller, M.; Heideman, C. L.; Zschack, P.; Koyano, M.; Anderson, M. D.; Kykyneshi, R.; Keszler, D. A.; Anderson, I. M.; Johnson, D. C. *Chem. Mater.* **2010**, *22*, 1002–1009.

(9) Snyder, G.; Toberer, E. *Nat. Mater.* **2008**, *7*, 105–114.

(10) Rowe, D. M. *CRC Handbook of Thermoelectrics: Macro to Nano*; Nature Publishing Group, 2005.

(11) Gurdal, Z. *Design and optimization of laminated composite materials*; Wiley, 1999; p. 337.

(12) Alemayehu, M. B.; Mitchson, G.; Hanken, B. E.; Asta, M.; Johnson, D. C. *Chem. Mater.* **2014**, *26*, 1859–1866.

(13) Atkins, R.; Dolgos, M.; Fiedler, A.; Grosse, C.; Fischer, S. F.; Rudin, S. P.; Johnson, D. C. *Chem. Mater.* **2014**, *26*, 2862–2872.

(14) Atkins, R.; Wilson, J.; Zschack, P.; Grosse, C.; Neumann, W.; Johnson, D. C. *Chem. Mater.* **2012**, *24*, 4594–4599.

(15) Boer, D. De; Bruggen, C. Van; Bus, G. *Phys. Rev. B* **1984**, *29*, 6797-6809

(16) Klipstein, P.; Bagnall, A. *J. Phys. C: Solid State Phys.* **1981**, 14 4067-4081.

(17) Salvo, F. Di; Moncton, D.; Waszczak, J. *Phys. Rev. B* **1976**, 14, 4321-4328.

(18) Greenaway, D.; Nitsche, R. *J. Phys. Chem. Solids* **1965**, *26*, 1445–1458.

(19) Rasch, J.; Stemmler, T.; Müller, B.; Dudy, L.; Manzke, R. *Phys. Rev. Lett.* **2008**, *101*, 237602.

(20) R. D. Barnard. *Thermoelectricity in Metals and Alloys*; Wiley: New York, 1972.

(21) Guilmeau, E.; Bréard, Y.; Maignan, A. *Appl. Phys. Lett.* **2011**, *99*, 052107.

(22) Bhatt, R.; Bhattacharya, S.; Patel, M.; Basu, R.; Singh, a.; Sürger, C.; Navaneethan, M.; Hayakawa, Y.; Aswal, D. K.; Gupta, S. K. *J. Appl. Phys.* **2013**, *114*, 114509.

(23) Bhatt, R.; Basu, R.; Bhattacharya, S.; Singh, a.; Aswal, D. K.; Gupta, S. K.; Okram, G. S.; Ganesan, V.; Venkateshwarlu, D.; Surgers, C.; Navaneethan, M.; Hayakawa, Y. *Appl. Phys. A* **2013**, *111*, 465–470.

(24) Wiegers, G.; Haange, R. *Eur. J. solid state Inorg. Chem.* **1991**, *28*, 1071-1078.

(25) Wan, C.; Wang, Y.; Wang, N.; Koumoto, K. *Materials.* **2010**, *3*, 2606–2617.

(26) Giang, N.; Xu, Q.; Hor, Y. S.; Williams, A. J.; Dutton, S. E.; Zandbergen, H. W.; Cava, R. *Phys. Rev. B: Condens. Matter* **2010**, *82*, 024503.

Chapter II

(1) Harris, F. R. PhD. Dissertation, University of Oregon, 2004.

(2) Noda, Y.; Masumoto, K.; Ohba, S.; Saito, Y.; Toriumi, K.; Iwata, Y.; Shibuya, I. *Acta Cryst.* **1987**, *C43*, 1443–1445.

(3) Harris, F. R.; Standridge, S.; Johnson, D. C. *J. Am. Chem. Soc.* **2005**, *127*, 7843–7848.

(4) Giang, N.; Xu, Q.; Hor, Y.; Williams, A.; Dutton, S.; Zandbergen, H.; Cava, R. *Phys. Rev. B Condens. Matter* **2010**, *82*, 024503.

Chapter III

1. J.A. Wilson and A.D. Yoffe, Adv. Phys. 18, 193 (1969).

2. M. Noh, C.D. Johnson, M.D. Hornbostel, J. Thiel, and D.C. Johnson, Chem. Mater. 8, 1625 (1996).

3. C. Heideman, N. Nguyen, J. Hanni, Q. Lin, S. Duncombe, D.C. Johnson, and P. Zschack, J. Solid State Chem. 181, 1701 (2008).

4. Q. Lin, M. Smeller, C.L. Heideman, P. Zschack, M. Koyano, M.D. Anderson, R. Kykyneshi, D.A. Keszler, I.M. Anderson, and D.C. Johnson, Chem. Mater. 22, 1002 (2010).

5. M. Beekman, G. Cogburn, C. Heideman, S. Rouvimov, P. Zschack, W. Neumann, and D.C. Johnson, J. Electron. Mater. 41, 1476 (2012).

6. C. Chiritescu,D.G. Cahill, N.Nguyen,D. Johnson, A. Bodapati, P. Keblinski, and P. Zschack, Science 315, 351 (2007).

7. N.T. Nguyen, P.A. Berseth, Q. Lin, C. Chiritescu, D.G. Cahill, A. Mavrokefalos, L. Shi, P. Zschack, M.D. Anderson, I.M. Anderson, and D.C. Johnson, Chem. Mater. 22, 2750 (2010).

8. M.M. Traum, G. Margaritondo, N.V. Smith, J.E. Rowe, and F.J. Di Salvo, Phys. Rev. B 17, 1836 (1978).

9. J.C.E. Rasch, T. Stemmler, B. Mu¨ ller, L. Dudy, and R. Manzke, Phys. Rev. Lett. 101, 237602 (2008).

10. F.J. Di Salvo, D.E. Moncton, and J.V. Waszczak, Phys. Rev. B 14, 4321 (1976).

11. Y. Hirota, K. Ichiyama, N. Hosoi, Y. Oikawa, Y. Miyahara, V. A. Kulbachinskii, and H. Oszki, Proceedings of the 21st International Conference on Thermoelectrics (Piscataway: IEEE, 2002), p. 159.

12. F. Gascoin, N. Raghavendra, E. Guilmeau, and Y. Bre´ard, J. Alloys Compd. 121, 521 (2012).

13. C. Riekel, J. Solid State Chem. 17, 389 (1976).

14. T. Hirota, Y. Ueda, and K. Kosuge, Mater. Res. Bull. 23, 1641 (1988).

15. F. Grønvold and F.J. Langmyhr, Acta Chem. Scan. 15, 1949 (1961).

16. G. Li, W.Z. Hu, D. Qian, D. Hsieh, M.Z. Hasan, E. Morosan, R.J. Cava, and N.L. Wang, Phys. Rev. Lett. 99, 027404 (2007).

17. Q. Lin, S. Tepfer, C. Heideman, C. Mortensen, N. Nguyen, P. Zschack, M. Beekman, and D.C. Johnson, J. Mater. Res. 26, 1866 (2011).

18. T.C. Ozawa and S.J. Kang, J. Appl. Cryst. 37, 679 (2004).

Chapter IV

1. Rowe, D. M. (ed.) *Thermoelectrics and its Energy Harvesting*, Vol. 1 and 2, Boca Raton: CRC Press (2012), and references therein.

2. Wan, C.; Wang, Y.; Wang, N.; Koumoto, K. Low-Thermal-Conductivity $(MS)_{1+x}(TiS_2)_2$ (M = Pb, Bi, Sn) Misfit Layer Compounds for Bulk Thermoelectric Materials, *Materials* **2010**, *3*, 2606-2617.

3. Wiegers, G. A. Misfit Layered Compounds: Structures and Physical Properties, *Prog. Solid. St. Chem.* **1996**, *24*, 1-139.

4. Heideman, C.; Nguyen, N.; Hanni, J.; Lin, Q.; Duncombe, S.; Johnson, D. C.; Zschack, P. The synthesis and characterization of new $[(BiSe)_{1.10}]_m[NbSe_2]_n$, $[(PbSe)_{1.10}]_m[NbSe_2]_n$, $[(CeSe)_{1.14}]_m[NbSe_2]_n$ and $[(PbSe)_{1.12}]_m[TaSe_2]_n$ misfit layered compounds, *J. Solid State Chem.* **2008**, *181*, 1701-1706.

5. Lin, Q.; Heideman, C. L.; Nguyen, N.; Zschack, P.; Chiritescu, C.; Cahill, D. G.; Johnson, D. C. Designed Synthesis of Families of Misfit-Layered Compounds, *Eur. J. Inorg. Chem.* **2008**, 2382-2385.

6. Lin, Q.; Smeller, M.; Heideman, C. L.; Zschack, P.; Koyano, M.; Anderson, M. D.; Kykyneshi, R.; Keszler, D. A.; Anderson, I. M.; Johnson, D. C. Rational Synthesis and Characterization of a New Family of Low Thermal Conductivity Misfit Layer Compounds $[(PbSe)_{0.99}]_m(WSe_2)_n$, *Chem. Mater.* **2010**, *22*, 1002-1009.

7. Noh, M.; Johnson, C. D.; Hornbostel, M. D.; Thiel, J.; Johnson, D. C. Control of Reaction Pathway and the Nanostructure of Final Products through the Design of Modulated Elemental Reactants, *Chem. Mater.* **1996**, *8*, 1625-1635.

8. Chiritescu, C.; Cahill, D. G.; Heideman, C.; Lin, Q.; Mortensen, C.; Nguyen, N. T. ; Johnson, D. C.; Rostek, R.; Böttner, H. Low thermal conductivity in nanoscale layered materials synthesized by the method of modulated elemental reactants, *J. Appl. Phys.***2008**, *104*, 033533-1–5 .

9. Giang, N.; Xu, Q.; Hor, Y. S.; Williams, A. J.; Dutton, S. E.; Zandbergen, H. W.; Cava, R. J. Superconductivity at 2.3 K in the misfit compound $(PbSe)_{1.16}(TiSe_2)_2$, *Phys. Rev. B* **2010**, *82*, 024503-1–5.

10. Le Bail, A.; Duroy, H. ; Fourquet, J. Ab-initio structure determination of $LiSbWO_6$ by X-ray powder diffraction *Mat. Res. Bull.* **1988** *23,* 447-452.

11. Rietveld, H.; Refinement of Debye-Scherrer synchrotron X-ray data from Al_2O_3, *J. Appl. Cryst.* **1987** *20*, 79-83.

12. Larson, A. C.; Von Dreele, R. B.; General Structure Analysis System (GSAS), Los Alamos National Laboratory Report LAUR 86-748, **2000**.

13. Toby, B. H. EXPGUI, a graphical user interface for GSAS, *J. App. Cryst.* **2001,** *34*, 210-213.

14. J. L. C. Daams, P. Villars, J. H. N. van Vucht, *Atlas of Crystal Structure Types for Intermetallic Phases*. ASM International: Materials Park, OH, 1991.

15. Riekel, C. Structure Refinement of $TiSe_2$ by Neutron Diffraction, J. Sol. State Chem. **1976**, 17, 389-392.

16. Wiegers, G. A.; Zhou, W. Y. The misfit layer compound $(SnSe)_{1.16}NbSe_2$, *Mater. Res. Bull.* **1991,** 26, 879-885.

17. De Boer, J. L.; Meetsma, A.; Zeinstra, T. J.; Haange, R. J.; Wiegers, G. A. Structures of the misfit layer compounds $(LaS)_{1.13}TaS_2$, `$LaTaS_3$' and $(CeS)_{1.5}TaS_2$, `$CeTaS_3$' *Acta Cryst. C* **1991,** 47, 924-930.

18. Gotoh, Y.; Onoda, M.; Akimoto, J.; Goto, M.; Oosawa, Y. The Layered Composite Crystal Structure of the Ternary Sulfide, $(BiS)_{1.07}TaS_2$ "$BiTaS_3$" *Japan. J. Appl. Phys.* **1992,** 31, 3946-3950.

19. van Smaalen, S.; Meetsma, A.; Wiegers, G. A.; De Boer, J. L. Determination of the modulated structure of the inorganic misfit layer compound $(PbS)_{1.18}TiS_2$, *Acta Cryst.* **1991,** 47, 314-325.

20. Wiegers, G. A.; Meetsma, A.; de Boer, J. L.; van Smaalen, S.; Haange, R. J. X-ray crystal structure determination of the triclinic misfit layer compound $(SnS)_{1.20}TiS_2$ *J Phys.: Cond. Mat.* **1991,** 3, 2603-2612.

21. Wiegers, G. A.; Meetsma, A.; Haange, R. J.; van Smaalen, S.; De Boer, J. L.; Meerschaut, A.; Rabu, P.; Rouxel, J. The incommensurate misfit layer structure of $(PbS)_{1.14}NbS_2$, `$PbNbS_3$' and $(LaS)_{1.14}NbS_2$, `$LaNbS_3$': an X-ray diffraction study, *Acta Cryst. B* **1990,** 46, 324-332.

22. Wiegers, G. A.; Meetsma, A.; van Smaalen, S.; Haange, R. J.; De Boer, J. L. Structural relationship between the orthorhombic, monoclinic and triclinic misfit layer compounds $(MS)_nTS_2$ (M = Sn, Pb, rare earth metals, T = Ti, V, Cr, Nb, Ta; 1.13 < n < 1.21) *Solid State Commun.* **1990,** 75, 689-692.

23. Meerschaut, A.; Guemas, L. Auriel, C.; Rouxel, J. Preparation, structure determination and transport properties of a new misfit layer compound:$(PbS)_{1.14}(NbS_2)_2$, *Eur. J. Solid State Inorg. Chem.* **1990**, 27, 557-570.

24. Lin, Q.; Tepfer, S.; Heideman, C.; Mortensen, C.; Nguyen, N.; Zschack, P.; Beekman, M.; Johnson, D. C. Influence of selenium vapor postannealing on the electrical transport properties of PbSe–WSe_2 nanolaminates, *J. Mater. Res.* **2011**, *26*, 1866-1871.

Chapter V

(1) Stein, A.; Keller, S.; Mallouk, T. *Science.* **1993**, *259*, 1558–1564.

(2) S.M.Sze. *Semiconductor Devices Physics and Technology*; Zobrist, W., Ed.; John Wiley and Sons, 2002.

(3) Wiegers, G.; Haange, R. *Eur. J. Solid State Inorg. Chem.* **1991**. *28*, 1071-1078.

(4) Harris, F. R.; Standridge, S.; Johnson, D. C. *J. Am. Chem. Soc.* **2005**, *127*, 7843–7848.

(5) Lin, Q.; Smeller, M.; Heideman, C. L.; Zschack, P.; Koyano, M.; Anderson, M. D.; Kykyneshi, R.; Keszler, D. A.; Anderson, I. M.; Johnson, D. C. *Chem. Mater.* **2010**, *22*, 1002–1009.

(6) Moore, D.; Stolt, M.; Atkins, R.; Sitts, L.; Jones, Z.; Disch, S.; Beekman, M.; Johnson, D. *Emerg. Mater. Res.* **2012**, *1*, 292–298.

(7) Phung, T.; Jensen, J.; Johnson, D. C.; Donovan, J. J.; McBurnett, B. G. *X-Ray Spectrom.* **2008**, *37*, 608–614.

(8) Van der Pauw, L. J. *Philips Tech. Rev.* **1958**, *20*, 220–224.

(9) Moore, D. B.; Sitts, L.; Stolt, M. J.; Beekman, M.; Johnson, D. C. *J. Electron. Mater.* **2012**, *42*, 1647–1651.

(10) Snyder, G.; Toberer, E. *Nat. Mater.* **2008**, *7*, 105–114.

Chapter VI

(1) Wiegers, G. A. *Prog. Solid State Chem.* **1996**, *24*, 1 – 139.

(2) Giang, N.; Xu, Q.; Hor, Y.; Williams, A.; Dutton, S.; Zandbergen, H.; Cava, R. *Phys. Rev. B: Condens. Matter* **2010**, *82*, 024503.

(3) Heideman, C.; Nyugen, N.; Hanni, J.; Lin, Q.; Duncombe, S.; Johnson, D. C.; Zschack, P. *J. Solid State Chem.* **2008**, *181*, 1701–1706.

(4) Lin, Q.; Smeller, M.; Heideman, C. L.; Zschack, P.; Koyano, M.; Anderson, M. D.; Kykyneshi, R.; Keszler, D. A.; Anderson, I. M.; Johnson, D. C. *Chem. Mater.* **2010**, *22*, 1002–1009.

(5) Chiritescu, C.; Cahill, D. G.; Heideman, C.; Lin, Q.; Mortensen, C.; Nguyen, N. T.; Johnson, D.; Rostek, R.; Böttner, H. *J. Appl. Phys.* **2008**, *104*, 033533.

(6) Harris, F. R.; Standridge, S.; Johnson, D. C. *J. Am. Chem. Soc.* **2005**, *127*, 7843–7848.

(7) Moore, D.; Stolt, M.; Atkins, R.; Sitts, L.; Jones, Z.; Disch, S.; Beekman, M.; Johnson, D. *Emerg. Mater. Res.* **2012**, *1*, 292–298.

8) Phung, T.; Jensen, J.; Johnson, D. C.; Donovan, J. J.; McBurnett, B. G. *X-Ray Spectrom.* **2008**, *37*, 608–614.

(9) Van der Pauw, L. J. *Philips Tech. Rev.* **1958**, *20*, 220–224.

(10) Bail, A. Le; Duroy, H.; Fourquet, J. L. *Mater. Res. Bull.* **1988**, *23*, 447–452.

(11) Rietveld, H. *J. Appl. Cryst.* **1969**, *20*, 65–71.

(12) Larson, A.; Dreele, R. Von *Los Alamos Nat. Lab.(unpublished)* **2004**.

(13) Toby, B. H. *J. Appl. Cryst.* **2001**, *34*, 210–213.

(14) Noda, Y.; Masumoto, K.; Ohba, S.; Saito, Y.; Toriumi, K.; Iwata, Y.; Shibuya, I. *Acta Cryst.* **1987**, *C43*, 1443–1445.

(15) Oftedal, I. *Z. physik. Chem.* **1928**, *134*, 301–310.

(16) Gotoh, Y.; Onoda, M.; Akimoto, J.; Goto, M.; Oosawa, Y. *Jpn. J. Appl. Phys., Part 1* **1992**, *31*, 3946–3950.

(17) Lafond, A.; Deudon, C.; Meerschaut, A.; Sulpice, A. *European Journal of Solid State and Inorganic Chemistry* **1994**, *31*, 967–978.

(18) Beekman, M.; Moore, D. B.; Atkins, R.; Heideman, C.; Lin, Q.; Hill, K.; Anderson, M.; Johnson, D. C. *Mater. Res. Bull. Online Proceedings Library* **2011**, *1329*.

(19) Wiegers, G. A.; Meetsma, A.; Haange, R. J.; Van Smaalen, S.; De Boer, J. L.; Meerschaut, A.; Rabu, P.; Rouxel, J. *Acta Crystallogr., Sect. B: Struct. Sci* **1990**, *46*, 324–332.

(20) Wiegers, G.; Meetsma, A.; De Boer, J. L.; Van Smaalen, S.; Haange, R. J. *J. Phys.: Condens. Matter.* **1991**, *3*, 2603–2612.

(21) De Boer, J. L.; Meetsma, A.; Zeinstra, T. J.; Haange, R. J.; Wiegers, G. a. *Acta Crystallogr., Sect. C: Cryst. Struct. Commun.* **1991**, *47*, 924–930.

(22) Van Smaalen, S.; Meetsma, A.; Wiegers, G. a.; De Boer, J. L. *Acta Crystallogr., Sect. B: Struct. Sci* **1991**, *47*, 314–325.

(23) Meerschaut, A.; Auriel, C.; Rouxel, J. *J. Alloys Compd.* **1992**, *183*, 129–137.

(24) Auriel, C.; Meerschaut, A.; Rouxel, J. *Mater. Res. Bull.* **1993**, *28*, 675–684.

(25) Meerschaut, A.; Guemas, L.; Auriel, C.; Rouxel, J. *Eur. J. Solid State Inorg. Chem.* **1990**, *27*, 557.

(26) Auriel, C.; Meerschaut, A.; Roesky, R.; Rouxel, J. *Eur. J. Solid State Inorg. Chem.* **1992**, *29*, 1079–1091.

(27) Roesky, R.; Meerschaut, A.; Rouxel, J. *Z. Anorg. Allg. Chem.* **1993**, 117–122.

(28) Rauch, E. R.; Duft, A. *Mater. Sci. Forum* **2005**, *495-497*, 197–202.

(29) Moeck, P.; Rouvimov, S.; Rauch, E. F.; Véron, M.; Kirmse, H.; Häusler, I.; Neumann, W.; Bultreys, D.; Maniette, Y.; Nicolopoulos, S. *Cryst. Res. Technol.* **2011**, *46*, 589–606.

Chapter VII

(1) Wiegers, G. A. *Prog. Solid State Chem.* **1996**, *24*, 1 – 139.

(2) Moore, D. B.; Beekman, M.; Disch, S.; Zschack, P.; Hausler, I.; Neumann, W.; Johnson, D. C. *Chem. Mater.* **2013**, *25*, 2404–2409.

(3) Giang, N.; Xu, Q.; Hor, Y. S.; Williams, A. J.; Dutton, S. E.; Zandbergen, H. W.; Cava, R. J. *Phys. Rev. B - Condens. Matter.* **2010**, *82*, 024503.

(4) Lin, Q.; Smeller, M.; Heideman, C. L.; Zschack, P.; Koyano, M.; Anderson, M. D.; Kykyneshi, R.; Keszler, D. a.; Anderson, I. M.; Johnson, D. C. *Chem. Mater.* **2010**, *22*, 1002–1009.

(5) Moore, D.; Stolt, M.; Atkins, R.; Sitts, L.; Jones, Z.; Disch, S.; Beekman, M.; Johnson, D. *Emerg. Mater. Res.* **2012**, *1*, 292–298.

(6) Atkins, R.; Moore, D.; Johnson, D. *Chem. Mater.* **2013**, *25*, 1744–1750.

(7) Oftedal, I. *Z. Phys. Chem.* **1928**, *134*, 301–310.

(8) Noda, Y.; Masumoto, K.; Ohba, S.; Saito, Y.; Toriumi, K.; Iwata, Y.; Shibuya, I. *Acta Cryst.* **1987**, *C43*, 1443–1445.

(9) Altshuler, B.; Khmel'Nitzkii, D.; Larkin, A.; Lee, P. *Phys. Rev. B* **1980**, *22*, 5142–5153.

(10) Alemayehu, M. B.; Mitchson, G.; Hanken, B. E.; Asta, M.; Johnson, D. C. *Chem. Mater.* **2014**, *26*, 1859–1866.

Chapter VIII

(1) Rowe, D. M. *CRC Handbook of Thermoelectrics: Macro to Nano*; Nature Publishing Group, 2005.

(2) Kanatzidis, M. G.; et al., *Prog. Solid State Chem.* **2007**, *36*, 1–133.

(3) Snyder, G.; Toberer, E. *Nat. Mater.* **2008**, *7*, 105–114.

(4) Chiritescu, C.; Cahill, D. G.; Heideman, C.; Lin, Q.; Mortensen, C.; Nguyen, N. T.; Johnson, D.; Rostek, R.; Böttner, H. *J. Appl. Phys.* **2008**, *104*, 033533.

(5) Mahanti, S. D.; Hogan, T. P. *Chemistry, physics, and materials science of thermoelectric materials*; Springer, 2003.

(6) Oftedal, I. *Z. Phys. Chem.* **1928**, *134*, 301–310.

(7) Noda, Y.; Masumoto, K.; Ohba, S.; Saito, Y.; Toriumi, K.; Iwata, Y.; Shibuya, I. *Acta Cryst.* **1987**, *C43*, 1443–1445.

(8) Atkins, R.; Moore, D.; Johnson, D. *Chem. Mater.* **2013**, *25*, 1744–1750.

(9) Moore, D. B.; Sitts, L.; Stolt, M. J.; Beekman, M.; Johnson, D. C. *J. Electron. Mater.* **2012**, *42*, 1647–1651.

(10) Giang, N.; Xu, Q.; Hor, Y. S.; Williams, A. J.; Dutton, S. E.; Zandbergen, H. W.; Cava, R. J. *Phys. Rev. B - Condens. Matter Mater. Phys.* **2010**, *82*, 024503.

(11) Merrill, D. R.; Moore, D. B.; Ditto, J.; Sutherland, D. R.; Falmbigl, M.; Winkler, M.; Hans-Fridtjof, P.; Johnson, D. C. *Eur. J. Inorg. Chem.* **2014**.

(12) Nolas, G. S.; Sharp, J.; Goldsmid, H. J. *Thermoelectrics: basic principles and new materials developments*; Zunger, A.; Osgood Jr., R. M.; Hull, R.; Sakaki, H., Eds.; Springer-Verlag Berlin Heidelberg, 2010; p. 229.

(13) Blatt, F. J. *Physics of electronic conduction in solids*; McGraw-Hill: New York, 1968; p. 210.

Chapter IX

[1] F. J. Disalvo, *Science* **1990**, *247*, 649–655.

[2] A. Stein, S. Keller, T. Mallouk, *Science* **1993**, *259*, 1558–1564.

[3] J. Schön, M. Jansen, *Angew. Chem. Int. Ed..* **1996**, *35*, 1286–1304.

[4] Y. Liebold-Ribeiro, D. Fischer, M. Jansen, *Angew. Chem. Int. Ed.* **2008**, *47*, 4428–31.

[5] D. C. Johnson, *Nature* **2008**, *454*, 174–175.

[6] M. D. Anderson, J. O. Thompson, D. C. Johnson, *Chem. Mater.* **2013**, *25*, 3996–4002.

[7] C. Heideman, N. Nyugen, J. Hanni, Q. Lin, S. Duncombe, D. C. Johnson, P. Zschack, *J. Solid State Chem.* **2008**, *181*, 1701–1706.

[8] J. Biscoe, *J. Appl. Phys.* **1942**, *13*, 364.

[9] D. Moore, M. Stolt, R. Atkins, L. Sitts, Z. Jones, S. Disch, M. Beekman, D. Johnson, *Emerg. Mater. Res.* **2012**, *1*, 292–298.

[10] Y. Noda, K. Masumoto, S. Ohba, Y. Saito, K. Toriumi, Y. Iwata, I. Shibuya, *Acta Cryst.* **1987**, *C43*, 1443–1445.

[11] D. De Boer, C. Van Bruggen, G. Bus, *Phys. Rev. B* **1984**, *29*, 6797.

[12] M. D. Anderson, C. L. Heideman, Q. Lin, M. Smeller, R. Kokenyesi, A. a Herzing, I. M. Anderson, D. a Keszler, P. Zschack, D. C. Johnson, *Angew. Chem. Int. Ed.* **2013**, *52*, 1982–5.

[13] G. A. Wiegers, A. Meetsma, R. J. Haange, S. van Smaalen, J. L. de Boer, A. Meerschaut, P. Rabu, J. Rouxel, *Acta Crystallogr., Sect. B Struct. Sci* **1990**, *46*, 324–332.

[14] G. Wiegers, A. Meetsma, J. L. de Boer, S. van Smaalen, R. J. Haange, *J. Phys. Condens. Matter.* **1991**, *3*, 2603–2612.

[15] J. L. de Boer, A. Meetsma, T. J. Zeinstra, R. J. Haange, G. a. Wiegers, *Acta Crystallogr., Sect. C Cryst. Struct. Commun.* **1991**, *47*, 924–930.

[16] S. van Smaalen, A. Meetsma, G. a. Wiegers, J. L. de Boer, *Acta Crystallogr., Sect. B Struct. Sci* **1991**, *47*, 314–325.

[17] A. Le Bail, H. Duroy, J. L. Fourquet, *Mater. Res. Bull.* **1988**, *23*, 447–452.

[18] H. Rietveld, *J. Appl. Cryst.* **1969**, *20*, 65–71.

[19] A. Larson, R. Von Dreele, *Los Alamos Nat. Lab.(unpublished)* **2004**.

[20] B. H. Toby, *J. Appl. Cryst.* **2001**, *34*, 210–213.